



Flame propagation in narrow channels

Fernando Veiga López

Tesis Doctoral

Flame propagation in narrow channels

Autor:

FERNANDO VEIGA LÓPEZ

Tesis depositada en cumplimiento parcial de los requisitos para el grado de
Doctor en Mecánica de Fluidos

Universidad Carlos III de Madrid

Director:

MARIO SÁNCHEZ SANZ

Codirector:

DANIEL MARTÍNEZ RUIZ

Leganés, junio de 2020

Esta tesis se distribuye bajo licencia "Creative Commons **Reconocimiento - No Comercial - Sin Obra Derivada**"



A meu pai.

Agradecimientos

No sé ni por dónde empezar, incluso resulta más complicado después de semanas sin veros. Cierro los ojos y sonrío. Es imposible no sentirme afortunado al, simplemente, echar la vista atrás. Han sido tres años repletos de dulces (y no tanto...) momentos y experiencias que, sinceramente, me han terminado por marcar. Lo más importante, siempre, sois vosotras y vosotros, las personas con las que uno tiene la fortuna de coincidir y disfrutar de pequeños fragmentos de su particular aventura. A veces, con suerte, incluso a largo plazo.

Me enfrento ahora a la difícil tarea de plasmar lo verdaderamente agradecido que os estoy. Solo espero no dejar nada ni a nadie en el tintero, lo de las expectativas lo dejamos para otro día. Allá vamos.

Empezaremos, como es lógico, por el final. Gracias Mario, sencillamente por todo. Por aquello que me has enseñado, que me ha hecho crecer tanto profesional como personalmente. Por tu apoyo, confianza y paciencia. También a ti Dani, por tu inestimable ayuda desde mis primeros pasos en esto de la ciencia, por tenderme siempre la mano y por mostrarme sin reparos tus siempre interesantes ideas y puntos de vista. Con toda la sinceridad y seguridad del mundo, me atrevo a decir que formamos un gran equipo.

Gracias Isra, Manolo y David, sin vosotros la consecución de este trabajo no habría sido posible. Porque me encanta gritar en estas líneas que es un placer trabajar con vosotros. Por ofrecerme, sin pedir nada a cambio, vuestra destreza, experiencia y maestría en el laboratorio. Recordarte también a ti, Eduardo, por tus importantísimas aportaciones a lo largo de estos años. Al igual que Mike y Jorge, por invitarme a colaborar con vosotros y acogerme con los brazos abiertos en vuestro grupo.

Gracias *Pat*, por lo bonito que ha sido encontrarte. Porque me hace feliz pensar que me llevo a una segunda hermana (con el permiso de Bena). Por haber sido y ser uno de mis principales

sopores, tanto dentro como fuera de estas horribles paredes de ladrillo. Y a tí, María. Sin más. A veces, la simplicidad encierra un significado mucho más complejo e interesante que todas las palabras vacías.

No podría olvidarme de mis Alejandros favoritos. Te agradezco, Álex, tu disponibilidad y compañía, las conversaciones de despacho y los siempre necesarios desahogos. A ti, Millán, el enfundarte conmigo el traje de viajero, recorriendo y comiéndonos el mundo. Se nos unió Alberto y fue, aún cuando se aventuraba imposible, mejor todavía. Gracias chicos por esos momentos irrepetibles.

Gracias Javi, por hacerme llorar de la risa prácticamente a diario e incitarme, con la sutileza de un paquidermo, a la ludopatía. A Mariano, por sus sabios consejos en este difícil esprint final y no dejarme caer en la espiral de locura que a veces acompaña al mundo de la investigación. Gracias Vanesa, Rafa, Marta, Jesús, Javi, Yusri, Kike y Dani por todo lo compartido y vivido estos años. Sin vosotras y vosotros todo esto habría sido infinitamente más complicado. Quiero agradecerlos también al resto del departamento de Térmica y Fluidos vuestra cercanía y cariño. También a la gente de *Cardio & Hit*, en particular a Marisa, Olaya y Raúl, por hacerme muy llevadero el día a día y ofrecerme una, a veces necesaria, vía de escape. Además mencionar a mis compañeros y compañeras de los equipos de fútbol sala, fútbol 7 y voleibol. Ha sido un placer competir a vuestro lado. Por último, que no menos importante, agradecer de corazón el apoyo y ayuda de mis alumnos y alumna de Trabajo Fin de Grado, con quienes he aprendido mucho a la vez que disfrutábamos de la hipnótica danza del fuego.

En definitiva, quiero recordar y dar las gracias a todas esas personas que, durante esta etapa de mi vida, han tallado una muesca, por pequeña que sea, en la figura definitiva de la persona en la que me he convertido. A todos y a todas, ¡gracias!.

Es ahora el momento de dar marcha atrás, de acordarme de toda esa gente que ya estaba y siguió ahí, a sabiendas de la alta probabilidad de secuelas que puede acarrear escribir una tesis. Gracias a Sof, Marina, Fer, Jorge, Carmen, Victor, Javo, Reynard y a todas y a todos los *aeros* que han estado ahí desde el momento en que me decidí a salir de casa. Al pesado de Antonio en especial, que no me lo despegó. Te agradezco infinito tu inagotable paciencia y bondad.

Grazas á miña xente galega! Es increíble todo lo que una frase puede englobar. A mis chicos y mis chicas de toda la vida que, pase lo que pase, están ahí desde el siglo pasado. A

Carlos, Jes, Brais, Pablo, Mei, Martin, Sergio, Jaco y Jochi, el mejor grupo de amigos jamás formado. A Sara y Tere, mis consejeras, confidentes y amigas. A Raquel, porque nadie me puede entender y ayudar como ella lo hace. Y también a Alba, por convertirse mil y una veces en mi refugio. Alguien con quien estar y sentirme a salvo, donde poder desprenderme temporalmente de mí, todavía, gruesa coraza.

Siguiendo mi lógica, terminaremos por el principio. Quiero dar las gracias a mi pequeña gran familia: Mamá, Bena, Beto, Midri y Pepe. Y bueno, ¡*Link* también! Por vuestro apoyo incondicional. No voy a añadir mucho más. Sé que siempre estáis y estaréis ahí. Lo mismo podréis esperar de mí.

Por último, a Papá, por haberme animado a todo, por imbuirme tu energía y valentía (¡y créeme cuando te digo que todavía me queda!). Porque he llegado hasta aquí gracias a tí. Con este peculiar homenaje, este pequeño grano de arena que creo aportar al mundo, quiero tratar de paliar, de alguna manera, el perenne dolor, esas lágrimas invisibles, que todavía marcan tu ausencia. Por eso, todo esto es por y para tí. Simplemente, ¡gracias!

Published and submitted content

The results of this PhD thesis were published or submitted for publication as:

- F. Veiga-López, D. Martínez-Ruiz, E. Fernández-Tarrazo, M. Sánchez-Sanz, *Experimental analysis of oscillatory premixed flames in a Hele-Shaw cell propagating towards a closed end.* Combustion and Flame 201 1-11 (2019).

This publication is included in **chapter 2 and 4** of this PhD thesis, but may not be indicated as a reference in the main text.

- D. Martínez-Ruiz, F. Veiga-López, D. Fernández-Galisteo, V.N. Kurdyumov, M. Sánchez-Sanz, *The role of conductive heat losses on the formation of isolated flame cells in Hele-Shaw chambers.* Combustion and Flame 209 187-199 (2019).

This publication is included in **chapter 5 and 7** of this PhD thesis, but may not be indicated as a reference in the main text.

- D. Martínez-Ruiz, F. Veiga-López, M. Sánchez-Sanz, *Premixed-flame oscillations in narrow channels.* Physical Review Fluids 4 (10) 100503 (2019).

This publication is included in **chapter 2** of this PhD thesis, but may not be indicated as a reference in the main text.

- F. Veiga-López, M. Kuznetsov, D. Martínez-Ruiz, E. Fernández-Tarrazo, J. Grune, M. Sánchez-Sanz, *Unexpected propagation of ultra-lean hydrogen flames in narrow gaps.* Accepted for publication in Physical Review Letters (2020) and chosen as editor's suggestion.

This publication is included in **chapter 5, 6 and 7** of this PhD thesis, but may not be indicated as a reference in the main text.

- **F. Veiga-López**, M. Kuznetsov, D. Martínez-Ruiz, M. Sánchez-Sanz, *Thermoacoustic analysis of lean premixed hydrogen flames in narrow vertical channels*. Preprint submitted to Fuel (2020).

This publication is included in **chapter 2, 3 and 4** of this PhD thesis, but may not be indicated as a reference in the main text.

and presented in the following conferences:

- **F. Veiga-López**, D. Martínez-Ruiz, E. Fernández-Tarrazo, M. Sánchez-Sanz, *Experimental analysis of premixed-flame propagation in a Hele-Shaw cell*. Fourteenth International Conference on Flow Dynamics, ICFD, Sendai, Japan (2017).

Some parts of this publication could appear in **chapter 2 and 4** of this PhD thesis, but may not be indicated as a reference in the main text.

- **F. Veiga-López**, D. Martínez-Ruiz, E. Fernández-Tarrazo, M. Sánchez-Sanz, *Experimental analysis of the oscillatory motion of premixed flames propagating in a Hele-Shaw cell*. Central States Section of the Combustion Institute's Spring Technical Meeting, Minneapolis, USA (2018).

Some parts of this publication could appear in **chapter 2 and 4** of this PhD thesis, but may not be indicated as a reference in the main text.

- D. Martínez-Ruiz, **F. Veiga-López**, M. Sánchez-Sanz, *Vessel confinement contributions to thermo-acoustic instabilities of premixed flames*. 71st Annual Meeting of the APS Division of Fluid Dynamics, Atlanta, USA (2018).

Some parts of this publication could appear in **chapter 2 and 4** of this PhD thesis, but may not be indicated as a reference in the main text.

- **F. Veiga-López**, D. Martínez-Ruiz, M. Kuznetsov, M. Sánchez-Sanz, *Thermoacoustic study of lean air-hydrogen premixed flames in narrow channels*. 11th Mediterranean Combustion Symposium, Tenerife, España (2019).

Some parts of this publication could appear in **chapter 3 and 4** of this PhD thesis, but may not be indicated as a reference in the main text.

- **F. Veiga-López**, D. Martínez-Ruiz, M. Kuznetsov, M. Sánchez-Sanz, *Experimental analysis of lean hydrogen premixed flames propagation in a confined vertical channel*. 9th European Combustion Meeting, Lisboa, Portugal (2019).

Some parts of this publication could appear in **chapter 3 and 4** of this PhD thesis, but may not be indicated as a reference in the main text.

- **F. Veiga-López**, M. Kuznetsov, J. Yanez, J. Grune, M. Sánchez-Sanz, *Near-limit flame propagation in a thin layer geometry*. 2nd Near Limit Flame Workshop, Beijing, China (2019).

Some parts of this publication could appear in **chapter 6 and 7** of this PhD thesis, but may not be indicated as a reference in the main text.

- **F. Veiga-López**, D. Martínez-Ruiz, M. Kuznetsov, E. Fernández-Tarrazo , M. Sánchez-Sanz, *Thermoacoustic analysis of lean H₂-air premixed flames in thin layers*. 27th ICDERS, Beijing, China (2019).

Some parts of this publication could appear in **chapter 3 and 4** of this PhD thesis, but may not be indicated as a reference in the main text.

- **F. Veiga-López**, M. Kuznetsov, J. Yanez, J. Grune, M. Sánchez-Sanz, *Flame propagation near the limiting conditions in a thin layer geometry*. ICHS, Adelaide, Australia (2019).

Some parts of this publication could appear in **chapter 3, 4, 6 and 7** of this PhD thesis, but may not be indicated as a reference in the main text.

Other research merits

During this research period the following merits were obtained:

- **F. Veiga-López**, Outstanding Student Presentation Award for the presentation titled: *Experimental Analysis of the Oscillatory Motion of Premixed Flames Propagating in a Hele-Shaw Cell*. Central States Section of the Combustion Institute's Spring Technical Meeting, 2018, Minneapolis, USA.
- D. Martínez-Ruiz, **F. Veiga-López**, M. Sánchez-Sanz, Milton Van Dyke APS/DFD Award 2018. [Premixed-flame oscillations in narrow channels](#).*

*One of the awarded frames was chosen as the front cover of this dissertation. The photograph shows the beautiful finger-like shape of an oscillatory rich propane flame under the effect of the secondary thermoacoustic instability.

Resumo

Coa chegada do cambio climático cómpre afondar nos temas que axuden a paliar os seus efectos máis adversos e inmediatos. Unha das principais liñas de investigación baséase no desenvolvemento de combustibles alternativos, como por exemplo o metano ou o hidróxeno, co fin de substituir aqueles derivados do petróleo e o carbón. Así mesmo, a investigación centrada na oxidación destes combustibles, con especial interese naqueles fenómenos que acontecen en xeometrías confinadas, é importante tanto para a seguridade dos futuros sistemas de xeración de enerxía e a mellora da súa eficiencia como para o deseño de xeradores portátiles. A combustión destes combustibles alternativos abre a porta á aparición de inestabilidades que poñan en risco a seguridade e o funcionamento de moitos sistemas. Un dos fenómenos más perigosos aparece cando as ondas acústicas presentes na cámara de combustión interactúan coas chamas, xerando unha forte vibración do fronte reativo e o campo fluido que pode ser transmitido á estrutura e derivar nunha rotura catastrófica.

Esta tese doutoral ten como obxectivo o estudo da estabilidade de chamas pre mesturadas de diferentes combustibles gaseosos que se propagan en xeometrías estreitas e semiconfinadas, como a celda *Hele-Shaw*. O principal interese reside na descripción das coñecidas como inestabilidades termoacústicas e o efecto de diferentes parámetros (combustible, mestura, perdidas de enerxía e gravidade) nelas. Ademais, preséntase e estúdase un novo réxime de propagación que emerxe para mesturas moi pobres dun combustible altamente difusivo, como é o hidróxeno, cando a canle na que se propaga é suficientemente estreita.

Comezaremos co estudo de chamas de propano, metano e dimetiléter (DME) que non se vexan afectadas pola gravidade. Éstas propáganse nunha cámara de combustión horizontal e fixa, modificando só a composición das mesturas queimadas. En relación ás inestabilidades a estudar, todas presentan dous rexímenes. Chamas suficientemente ricas (pobres) de propano ou DME (metano) interactúan coas ondas acústicas e comezan a vibrar violentamente, por mor

das altas presións acústicas que aparecen, á frecuencia propia marcada polas condicións da cámara (xeometría, temperatura media, posición do fronte). Alén diso, a forma da chama vese claramente modificada, mudando do característico fronte lixeiramente ondulado das inestabilidades *Darrieus-Landau* a outro moito máis estirado, xerando ondas con forma de dedos cunhas longas colas. Este réxime coñécese como o das inestabilidades termoacústicas secundarias. Cando se queiman chamas más pobres (ricas) dun valor crítico –que depende da mestura–, éstas oscilan suavemente. Aparece o réxime primario, no que as presións acústicas asociadas son moitos menores e a forma da chama non se ve modificada. De seguido, rotamos a cámara de combustión e permitimos así que as chamas se propaguen cara abaixo e influenciadas polo efecto estabilizador da gravidade. En comparación coa propagación horizontal, non se atopan diferencias de calado. Isto permítenos contrapoñer os resultados de hidrocarburos coas chamas de hidróxeno pobre que queimamos nunha canle de similares características e influenciada tamén pola flotabilidade. O hidróxeno compórtase como o metano: mesturas suficientemente ricas vibran de forma feble baixo o efecto do réxime primario e mesturas más pobres transicionan ao réxime secundario para vibrar con forza.

Ademais, o efecto das perdidas acústicas e de calor estúdase para chamas estequiométricas de DME e diferentes composicións de hidróxeno e aire, diminuíndo o tamaño da canle. Ata acadar estreiteces pequenas, estas perdidas non son importantes. Chega un punto crítico no que as ondas se comezan a atenuar, incluso a desaparecer, por mor da interacción dísticas coa capa límite acústica e o incremento das perdidas de calor coas paredes da cámara. Un fenómeno do hidróxeno en particular é que a rexión de inestabilidades secundarias vese reducida, aflorando tamén unha zona de transición adicional para chamas moi pobres preto do límite, na que o fronte se rompe en varias estruturas más pequenas. Esta discontinuidade da chama provoca unha interacción más feble co fronte, permanecendo éste baixo o efecto das inestabilidades primarias.

Alén diso, analizamos chamas propagándose cara arriba. A dinámica de chamas pobres e lentas vese gobernada pola inestabilidade de *Rayleigh-Taylor*, o que xera uns frontes moi más suaves e lisos que chamas idénticas que se moven en dirección oposta e que non se perturban pola presencia da acústica na cámara. Este comportamento pasa a ser crítico para casos pobres de hidróxeno e metano. Éstas vibran e xeran altas presións acústicas (arredor de 3/5 kPa) cando se propagan horizontalmente ou cara abaixo, no que a gravidade exerce

un efecto estabilizador. Sen embargo, non se ven afectadas polas oscilacións acústicas ao se propagar cara arriba. Con isto, mostramos neste traballo unha relación directa e clara entre as inestabilidades termoacústicas e a forma do fronte.

Polo que a curvatura e a elongación do fronte afectarían á conducción e á difusión e caracterizarían a resposta das chamas ás perturbacións de presión. Comunmente, o número de *Markstein* describe este efecto, polo que o sinalamos como posible parámetro de control destas inestabilidades. Ademais, o seu valor diminúe de forma monótona para as chamas estudadas, o que reforza a súa candidatura. Sen embargo, a propia definición deste parámetro e todo análise matemático derivado del só está contemplado para mesturas cun número de *Lewis* preto a un. Por tanto, o número de *Markstein* non pode describir de forma precisa a interacción coa acústica do hidróxeno, xa que ésta só se atopa en casos considerablemente pobres e cun $Le \sim 0.3$.

Para rematar, considerábase imposible que chamas ultra pobres de hidróxeno sobreviviran en cámaras de combustión confinadas e extremadamente estreitas. Nós predicimos, cunha simulación numérica simplificada (quasi 2D) na que tamén se consideran as perdas de calor, e verificamos experimentalmente cómo estas chamas non só se propagan senón que o fan dunha maneira sen precedentes en canles cunha estreitez inferior a 6 mm. Estas mesturas altamente difusivas combaten condicións tan adversas como as expostas ben partindo o fronte en pequenas celas que se moven a unha velocidade constante ou volvendo a romper dunha maneira cíclica, delineando unha circulación fractal que asemella ás estruturas que seguen habitualmente seres vivos, como as bacterias e os fungos, en situacións de carencia de alimento. A combinación da alta difusivididade máscia do hidróxeno e as altas perdas de calor cara as paredes sólidas das nosas estreitas canles habilita e explica estes dous novos métodos de propagación.

Resumen

El cambio climático ya está aquí. Con el fin de paliar sus peores efectos, se acelera la investigación científica relacionada con el aumento global de la temperatura de la Tierra. Por ejemplo, el estudio de combustibles alternativos, como el metano o el hidrógeno, busca sustituir, en un período de tiempo relativamente corto, aquellos derivados del petróleo y al carbón. Por otro lado, las investigaciones centradas en procesos de combustión en geometrías confinadas son interesantes en relación a la seguridad, desarrollo de pequeños combustores o incluso la mejora de la eficiencia de los motores de combustión interna. El uso de combustibles gaseosos no convencionales puede destapar inestabilidades previamente ausentes que afectan al rendimiento y la seguridad, en general, de todos los sistemas de generación de energía. En particular, las llamas pueden acoplarse con las ondas acústicas presentes en la cámara de combustión, generando una fuerte pulsación del frente reactivo. Esta vibración del campo fluido puede ser a su vez transmitida a la estructura que sostiene el sistema y, potencialmente, desencadenar roturas catastróficas.

Por las razones enumeradas anteriormente, entre otras, esta tesis doctoral tiene como objetivo estudiar la estabilidad de llamas gaseosas premezcladas que se propagan en geometrías estrechas y semiconfinadas, como la celda Hele-Shaw. Nos centraremos, por un lado, en las conocidas como inestabilidades termoacústicas y, por otro, en un régimen de propagación previamente desconocido que aparece en llamas extremadamente pobres de combustibles altamente difusivos, como el hidrógeno. La metodología aplicada consiste en la evaluación, mayormente experimental, del efecto de diferentes parámetros (combustible, composición de la mezcla, pérdidas de calor y gravedad) en la aparición de dichos fenómenos.

Primero, se estudia la propagación de llamas de metano, propano y dimetiléter (DME), minimizando efectos de flotabilidad y cambiando la composición de sus mezclas con aire. Todos estos combustibles muestran dos regímenes de acoplamiento termoacústico. En concreto,

mezclas pobres (ricas) de propano y DME (metano), oscilan suavemente en el régimen termoacústico primario, por lo que su contorno, ligeramente rizado por la estabilidad de *Darrieus-Landau*, no se ve modificado durante su propagación a lo largo del canal. Mezclas más ricas (pobres) que un valor crítico –dependiente de la mezcla– muestran una interacción mucho más marcada con la acústica y se mueven bajo el efecto de las inestabilidades termoacústicas secundarias. Éstas se caracterizan por un movimiento oscilatorio muy violento, generando picos acústicos de hasta 6 kPa, a la frecuencia propia dictada por las condiciones de la cámara (geometría, temperatura media, posición del frente reactivo, *etc.*). Su forma se modifica por completo, volviéndose altamente estirada y generando unos lóbulos con forma dactilar y largas colas. Después, rotamos la celda Hele-Shaw para añadir el efecto de la gravedad al problema. Aquellas llamas que se propagan hacia abajo se ven estabilizadas por esta aceleración y no muestran cambios significativos en comparación con las llamas horizontales. Esto nos permite comparar las llamas de los hidrocarburos nombrados previamente con las de hidrógeno pobre, las cuales se propagan en una geometría parecida y también hacia abajo. Se comportan, cualitativamente, de la misma manera que el metano. Llamas suficientemente ricas se ven afectadas por la suave oscilación del régimen primario, transicionando aquellas más pobres al secundario para vibrar con fuerza.

Por otro lado, redujimos el grosor del canal para una mezcla fija de DME con aire (estequiométrica) y diversas mezclas de hidrógeno, para contabilizar el efecto de las pérdidas de calor y acústicas del sistema. Se ve que son relativamente despreciables –de nuevo, dependientes de la mezcla– hasta alcanzar geometrías suficientemente estrechas. Es aquí donde la acústica comienza a ser atenuada, incluso totalmente eliminada, por la creciente interacción con la capa límite acústica y las crecientes pérdidas de calor hacia las paredes del contenedor. En relación al hidrógeno, la región de inestabilidades secundarias se ve progresivamente reducida al estrechar el canal, mostrando una nueva zona de transición a la región primaria para llamas muy pobres. En estos casos, el frente se rompe y divide en llamas más pequeñas que interactúan de forma más débil con las ondas acústicas.

Además, analizamos llamas que se propagan hacia arriba. La inestabilidad de *Rayleigh-Taylor* se vuelve dominante para valores suficientemente pequeños del número de Froude –que compara los efectos de flotabilidad e inercia–, que se obtienen para llamas pobres y lentas. Las llamas que se rigen por esta inestabilidad desarrollan frentes menos

arrugados que las que se propagan en dirección opuesta e ignoran cualquier presencia de ondas acústicas en el sistema. Este comportamiento se vuelve crítico para casos pobres de hidrógeno y metano. Estas llamas vibran generando altas presiones acústicas cuando se propagan hacia abajo u horizontalmente. Pero no se ven afectadas por estas oscilaciones cuando viajan hacia arriba. Con todos estos resultados, damos una relación directa y clara entre las inestabilidades termoacústica y la forma del frente.

Por tanto, la curvatura y elongación de las llamas afectarían a los procesos de conducción y difusión y, por ello, caracterizarían la respuesta del frente a perturbaciones de presión oscillatorias. Este efecto se caracteriza comúnmente con el número de Markstein, que podría controlar la transición entre los diferentes modos de inestabilidad termoacústica. Además, su tendencia monótona decreciente en las llamas estudiadas, lo refuerzan como el principal candidato para ello. Sin embargo, la definición de este parámetro, y por consiguiente toda teoría relacionada con él, solo es válida para mezclas con igual difusión térmica y másica ($Le \sim 1$). Esto conlleva que el número de Markstein no pueda describir de forma detallada y precisa mezclas de hidrógeno pobre ($Le \sim 0.3$), que es donde aparecen las inestabilidades termoacústicas.

Finalmente, se creía imposible la propagación de llamas de hidrógeno extremadamente pobre en geometrías muy estrechas y confinadas. Aquí, la predecimos con una simulación numérica quasi-2D que incluye los efectos de las pérdidas de calor, para luego demostrar empíricamente cómo llamas con una concentración de combustible muy baja experimentan una propagación sin precedentes en espacios muy estrechos, incluso alcanzando geometrías inferiores a 6 mm. Estas llamas, con una alta difusividad másica, son capaces de soportar condiciones tan adversas como las expuestas, rompiendo su frente de propagación en varias celdas aisladas que o bien se propagan a una velocidad constante y siguiendo trayectorias prácticamente rectilíneas, o se dividen cíclicamente para seguir caminos que delinean sorprendentes patrones fractales, similares a aquellos que generan diferentes mecanismos biológicos, como las bacterias o los hongos, cuando se encuentran ante una situación de escasez de alimento. La combinación de la alta difusividad másica del hidrógeno y unas muy severas pérdidas de calor hacia las paredes de nuestros canales, permite y explica los dos nuevos métodos de propagación.

Abstract

The sudden arrival of the climate change hurries fundamental research on a wide variety of topics trying to slow it down and counteract its effects. One of the examples is the study of alternative fuels (*e.g.*, methane and hydrogen) to replace oil and coal. Furthermore, scientific investigation focusing on combustion in confined geometries is also interesting in safety-related scenarios, as well as in the development of small burners, or even improving the efficiency of the existing and upcoming internal combustion engines. Combustion of premixed alternative gaseous fuels involves several instabilities that affect the overall performance and security of confined power generation systems. Particularly, the flames may couple with the acoustic waves produced in the combustion chamber, generating a strong pulsation of the reactive front which is also transmitted to the holding structure and can lead to a catastrophic failure.

This dissertation aims to study the stability of premixed gaseous flames propagating in semi-confined narrow geometries (*i.e.*, Hele-Shaw cell). The spotlight focuses on the so-called thermoacoustic instabilities and a previously unknown propagation regime, introduced here, for ultra-lean highly-diffusive flames. The methodology consists of the evaluation of experimental studies to assess the effect of different parameters (*e.g.*, fuel, mixture composition, energy losses, gravity) on their onset.

First, we study the combustion of methane, propane and dimethylether (DME) blends with air, minimizing buoyancy effects and changing the composition of the mixture. Regarding thermoacoustics, all the fuels undergo two regimes of acoustic coupling. Lean enough (rich) propane and DME (methane) flames oscillate smoothly, given the relatively low interaction with the acoustic waves, at the primary thermoacoustic regime, and keep their slightly wrinkled outline (due to the hydrodynamic instability) during their whole journey along the channel. Richer (leaner) flames than a critical value –mixture dependent– show a strong coupling with the acoustic waves and develop the secondary thermoacoustic instability, characterized by a

violent oscillatory motion of the front, related to high acoustic pressures, at the eigenfrequency determined by the conditions of the chamber (*i.e.*, geometry, average temperature, position of the front, *etc.*). The shape of the reactive front changes from the characteristic smoothly-wrinkled Darrieus-Landau front to become very stretched, generating lobes with the shape of fingers with long tails. Later, we rotate the combustion chamber to burn downward-propagating flames which are somehow influenced by the stabilizing effect of buoyancy. The differences found are not of major importance and, therefore, it is possible to compare the previous results to the ones obtained for lean hydrogen-air buoyant mixtures propagating in a similar geometry. They behave as methane flames: rich-enough downward-propagating flames begin to vibrate smoothly, under the primary acoustic regime described before. Mixtures leaner than a critical value are able to transit to the secondary oscillating regime.

Additionally, we reduce the channel thickness for a stoichiometric non-buoyant DME flame and different hydrogen-air mixtures, of variable composition and traveling downwards, to evaluate heat losses and acoustic damping *via* viscous effects. They result to be almost negligible –mixture dependent– until reaching sufficiently thin geometries, where acoustics begin to be attenuated, and eventually totally removed, due to the interaction with the acoustic boundary layer and the increasing heat losses to the surrounding walls. Regarding hydrogen, the region of equivalence ratio for the secondary thermoacoustic instability diminishes, showing an additional transition for very lean flames. There, the reactive front breaks into several smaller flames and their feedback with the acoustic waves becomes weaker.

Next, we test flames travelling upwards, finding that the Rayleigh-Taylor instability becomes dominant for sufficiently small values of the Froude number –that compares gravity to inertial effects–, obtained for lean and rich enough flames that propagate slowly. Flames governed by this instability develop less wrinkled fronts than those propagating to the opposite direction, and remain unresponsive to the interaction with acoustics. This behaviour becomes critical for lean hydrogen and methane flames, that do vibrate strongly and build up pressure peaks up to 3/5 kPa if gravity is negligible or stabilizing, but they show zero feedback with acoustic when propagating upwards. We give here a direct and clear connection between thermoacoustics and the shape of the front.

Therefore, curvature and strain effects on conduction and diffusion processes are found to be important in the response of the flames to dynamic pressure perturbations. This effect is commonly represented by the Markstein number, which might control the transition between the different aforementioned thermoacoustic instabilities. Furthermore, its monotonic decreasing trend with the composition of the mixture –for the analyzed flames– reinforces it as an important actor. Nevertheless, its definition and the related theoretical analyses found in the literature only apply for equidiffusional ($Le \sim 1$) mixtures, and are not accurate enough to describe the vibratory hydrogen flames, only found for considerably lean mixtures ($Le \sim 0.3$), considered in our experiments.

Finally, the propagation of ultra-lean hydrogen flames was thought to be impossible in very narrow and confined geometries. We first predict with a simplified quasi-2D non-adiabatic simulation and then demonstrate empirically how flames with very low fuel concentration undergo an unprecedented propagation in gaps narrower than 6 mm: the highly-diffusive flames can withstand such adverse conditions by parting the front into several isolated flame cells that move at a constant velocity with an almost straight trajectory or split cyclically to fulfill a fractal-like circulation that looks like the pathway formed by different living mechanisms, such as starving bacteria or fungi. The combination of a high mass diffusivity of hydrogen and severe heat losses to the enclosing solid walls of our thin channels enables and explains the two new propagation schemes.

Contents

Agradecimientos	i
Published and submitted content	v
Other research merits	ix
Resumo	xi
Resumen	xv
Abstract	xix
Nomenclature	xxvii
1 Introduction	1
1.1 Premixed flames	5
1.2 Objectives	10
1.3 Experimental set-up	11
1.4 Outline of the document	13
	xxiii

I Thermoacoustic instabilities	19
Opening remarks	23
2 Thermoacoustic instabilities in hydrocarbon and ether gaseous flames	25
2.1 Experimental setups and procedures	29
2.2 Effect of the mixture composition for non-buoyant flames	33
2.2.1 Propane flames	35
2.2.2 Methane flames	42
2.2.3 Dimethylether (DME) flames	44
2.3 Effect of the combustion chamber thickness h	45
2.3.1 Heat losses	47
2.3.2 Viscous layer	50
2.4 Effect of buoyancy	51
2.4.1 Downward-propagating flames	52
2.4.2 Upward-propagating flames	57
Appendix 2.A Image analysis and post-processing	71
3 Thermoacoustic instabilities in buoyant lean hydrogen flames	73
3.1 Experimental setup and procedure	74
3.2 Effect of the mixture composition for downward-propagating flames	76
3.3 Effect of the channel gap thickness h	80
3.4 Effect of buoyancy	82
4 Conclusions and future work	89

II Near-limit combustion of hydrogen	111
Opening remarks	115
5 Numerical analysis of the propagation of highly-diffusive flames in a quasi-2D non-adiabatic geometry	117
5.1 Quasi-2D considerations	118
5.2 Heat-loss effect in non-buoyant flames	120
5.2.1 Open-closed (OC) propagation	121
5.2.2 Closed-open (CO) propagation	123
5.2.3 Flame velocity and burning times	124
5.2.4 The role of the thermodiffusive instability	126
5.3 Effect of the heat losses in buoyant flames	127
5.3.1 Upward-propagating flames	128
5.3.2 Downward-propagating flames	131
5.4 One or two-headed cell flames	132
Appendix 5.A Mathematical formulation*	139
6 Experimental observations of ultra-lean H₂-air flames in narrow channels	151
6.1 Experimental setup and procedure	151
6.2 Splitting and steady flame cells	153
6.3 Effect of mass diffusivity	159
6.4 Effect of gravity	160
6.5 One or two-headed cells	161
7 Conclusions and future work	165

Nomenclature

Variables and physical constants

α	Angle between the cell and the horizontal	\mathcal{L}	Markstein length
β	Zel'dovich number	\mathcal{M}	Markstein number
δ_T	Flame thickness	\mathcal{R}	Ideal gas constant
δ_v	Acoustic boundary layer thickness	μ	Dynamic viscosity
\dot{m}	Mass flow	ν	Kinematic viscosity
\dot{x}	Observed circular flame velocity	ν_P	Poisson coefficient
ϵ	Box size used for the box counting method	Ω	Reaction rate
γ	Gas expansion parameter	ω	Angular frequency
γ_g	Heat capacity ratio	ϕ	Equivalence ratio
λ	Cell wavelength	ρ	Density
\mathcal{A}	Signal instantaneous amplitude	θ	Dimensionless temperature
\mathcal{K}	Curvature, strain and flame surface effect on the flame burning velocity	A	Arrhenius constant
		a	Dimensionless channel thickness
		b	Heat loss parameter
		c	Speed of sound

c_p	Specific heat at constant pressure	p	Acoustic pressure peak
D	Stiffness	Pe	Peclet number
d_f	Fractal dimension	Q	Heat released per unit of fuel mass
D_i	Mass diffusivity of component i	q_f	Thermal power released by the flame
D_T	Thermal diffusivity	q_k	Conductive thermal power losses
E	Activation energy	r	Radius
E_Y	Young modulus	r_f	Circular flame cell width
f	Frequency	Re	Reynolds number
f_p	Flame position frequency	S_f	Wrinkled flame burning velocity
f_s	Acoustic frequency	S_L	Planar flame burning velocity
Fr	Froude number	S_T	Overall flame propagation velocity
G	Gravity parameter	T	Temperature
g	Constant acceleration of gravity at Earth	t	Time
h	Thickness of the combustion chamber	T_l	Temperature at a distance l from the flame
k	Thermal conductivity	t_r	Residence time of the flame
L	Length of the combustion chamber	t_s	Residence time of a sound wave
l	Longitudinal distance from a burned region to the flame	t_{diff}	Diffusion time
Le	Lewis number	t_{fill}	Filling time
M	Mach number	$t_{k,w}$	Characteristic time of conduction
P	Power level	t_{rad}	Radiation characteristic time
		$t_{s,d}$	Acoustic dissipation time
		U_g	Buoyancy-induced velocity

U_L	Observed flame velocity	V	Volume
U_{strat}	Stratification velocity	W	Width of the combustion chamber
U_{vert}	Vertical velocity of a lobe due to the induced transverse Rayleigh-Taylor velocity	w	Acoustic-induced velocity
		Y	Mass fraction
		[X]	Concentration of the species X

Recurrent sub- and superscripts

0	Reference	<i>hot</i>	Hot premixture
-	Average	<i>max</i>	Maximum
<i>air</i>	Air	<i>O</i>	Oxidizer
<i>b</i>	Burned products	<i>plug</i>	Plug
<i>c</i>	Critical	<i>r</i>	Residence
<i>eff</i>	Effective	<i>tot</i>	Total
<i>F</i>	Fuel	<i>u</i>	Unburned reactants (room)
<i>g</i>	Gas	<i>w</i>	Solid walls

Abbreviations and chemical formulae

C_3H_8	Propane	fps	Frames per second
CH_4	Methane	H_2	Hydrogen
CO	Closed-Open	He	Helium
CO_2	Carbon dioxide	HS	Hele-Shaw
DL	Darrieus-Landau instabilities	N_2	Nitrogen
DME	Dimethylether	NO_x	Nitrous oxides

xxx

OC	Open-Close	RT	Rayleigh-Taylor instabilities
OH	Hydroxide	ST	Saffmann-Taylor instabilities
OO	Open-Open		
PMMA	Polymethyl methacrylate	TA	Thermoacoustic instabilities
PVC	Polyvinyl chloride	TD	Thermodiffusive instabilities

Introduction

Global warming is a reality [1–4]. Despite the huge concern of our society, only vague and insufficient political directives are being applied to fight against such a giant [5]. Most of these changes have proved to be a fiasco as CO₂ emissions keep rising globally, running away from the too-optimistic and ignored targets of the European Union (Fig. 1.1).

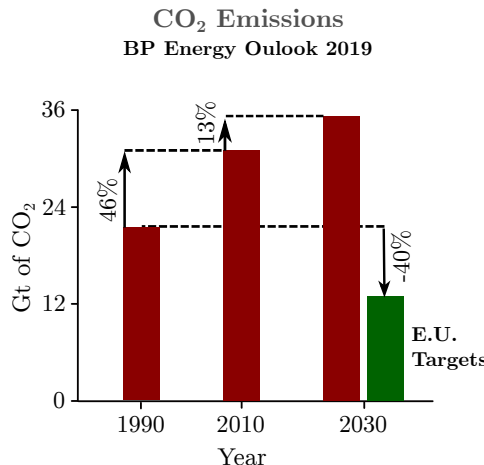


FIGURE 1.1 | Expected global CO₂ emissions for the close future. Data reproduced from [6].

During the last decades of the 20th century, different renewable and clean-energy alternatives were developed (*e.g.*, wind, solar) [7] trying to remove oil and coal as the main energy sources. The intention was to avoid the upcoming climate problem that, unfortunately, we are now

facing and that will be even more intense soon [2]. Recent studies claim that the average surface temperature of the Earth increases faster than previously thought (Fig. 1.2), as will also increase the population affected by the derived risks of global warming (Fig. 1.3). On light of the numbers, one can only affirm that the measures are –for now– not enough.

ACCELERATED WARMING

Climate simulations predict that global warming will rise exponentially if emissions go unchecked.

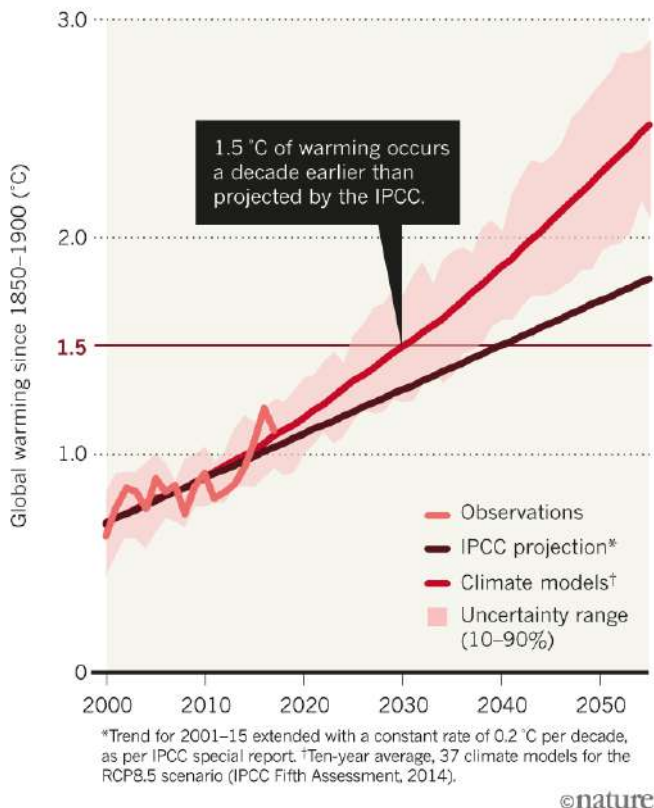


FIGURE 1.2 | Global temperature rise predictions by the IPCC linear extrapolation and different climate models [2]. Publication permission granted by the publisher under license number 1014952-1.

On top of this, the current economic system asks for a relentless growth and continuous production to ensure its own survival, and Earth population keeps growing. For these reasons, the derived rise in energy demand (Fig. 1.4) leads to an increment of the global energy

consumption. This drives us directly to an imminent energetic challenge as our main source (oil) is harmful for the environment and close to its end. The question now is how to keep a sustainable growth of our production to supply even more people with power, using the available resources on the planet.

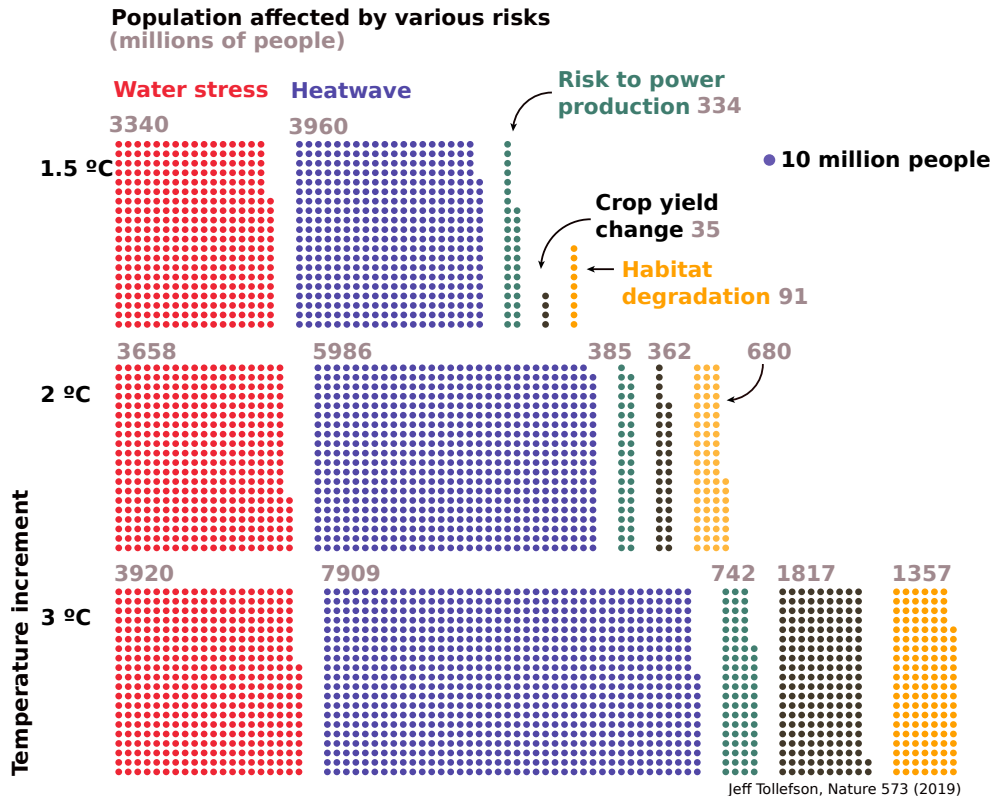


FIGURE 1.3 | Affected people by global warming derived risks as a function of the global temperature increment [8]. Publication permission granted by the publisher under license number 1014952-2.

We must reshape the way we produce energy. Figure 1.4 shows the predicted energy share for the next twenty years [6]. The strategy that we are now following is to strongly reduce the energy harvested from the combustion of oil-derived fuels and coal. However, drastic changes are neither advisable nor possible. A transition period must be held to reach the difficult emission-free goal, only obtained from fully renewable sources. For the next years, burning oil, gas and coal seems to keep holding the main primary energy share, up to 80% of the total. We still need combustion. The plan for the transition period is to bet on sustainable combustion,

mostly relying on gaseous light hydrocarbons (*e.g.*, CH₄) or alternative gaseous fuels (*e.g.*, dimethylether –DME–), as they emit much less CO₂ compared to heavy hydrocarbons or coal, for the same amount of energy obtained. In addition, hydrogen provides big amounts of energy as an alternative fuel when oxidizing, emitting no CO₂. For this reason, it is a strong candidate to endure not only during the transition plan but as a consolidated zero-emissions energy source [9, 10]. However, burning gaseous alternative fuels, such as methane or hydrogen, is only part of the envisioned solution. Additionally, the energy production from renewable technologies should become an important part of the energy share soon. However, it is still not sufficient to be the base of the global production as these technologies seem to be not mature yet [7].

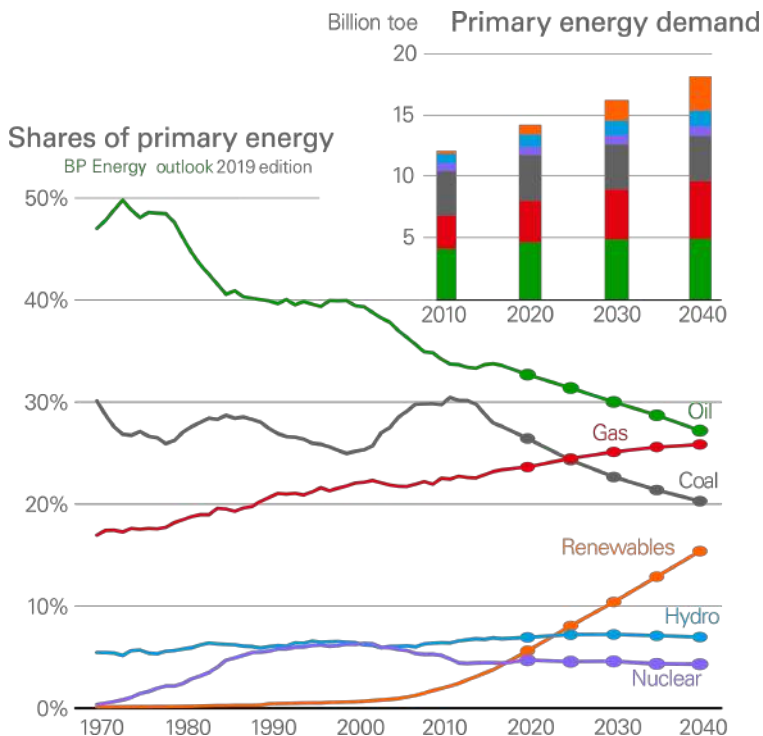


FIGURE 1.4 | Global energy demand and share prediction for the next years [6].

1.1 Premixed flames

Obtaining energy from fuel combustion can be seen as a settled technology. However, the arrival of new fuels opens new challenges to be faced. Focusing on gaseous fuels, it is interesting to burn premixed or partially-premixed fuel and oxidizer blends for efficiency and emission-related reasons. These type of processes allows to easily modify the mixture composition, which permits burning flames out of stoichiometric conditions (*i.e.*, lean flames). This leads to reduced burning temperatures, thus lowering NOx emissions, which are strongly influenced by the temperatures found in the combustion chambers [11], and avoiding wearing damage due to extreme temperatures. Additionally, the composition can be homogenized, which reduces the probability of finding hot spots during the reaction (directly related to an increment of NOx emissions) or leaving part of the available fuel unburned. Furthermore, strong heterogeneity of the fuel-oxidizer blends as in diffusion flames produces higher soot emissions, and not burning the whole available fuel leads to a waste of energy and consequent decrease of the efficiency of any process.

Premixed flame structure

Premixed flames are propagating waves that move at a determined velocity [12] consuming the available reactants and increasing the local temperature *via* the chemical energy release. Figure 1.5 represents the inner structure of an idealized one-dimensional premixed flame. The region of interest is divided into two differentiated parts: the reaction and preheat zones, which occupy a determined length, known as flame thickness, δ_T .

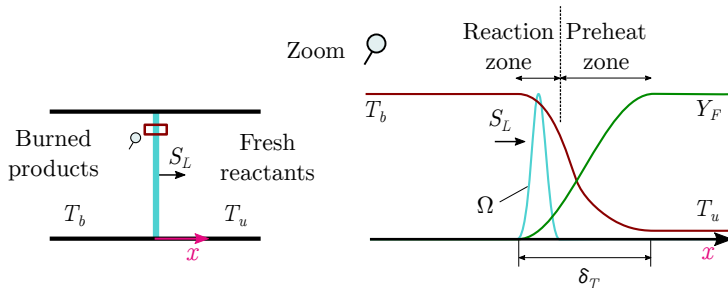


FIGURE 1.5 | Sketch of the structure of 1-D premixed flames.

The reaction zone is a very thin region where substantial chemical reactions take place. If one considers a simplified one-step Arrhenius model for chemistry, the reaction rate per unit mass per unit time can be written as

$$\Omega = AY_F Y_O e^{-E/\mathcal{R}T}, \quad (1.1)$$

being A the pre-exponential factor, E the activation energy that depends on the fuel, \mathcal{R} the ideal gas constant, and Y_F and Y_O the mass fraction of the fuel and oxidizer respectively. The rate of reaction is highly dependent on temperature and is rapidly reduced out of the reactive region. Introducing the dimensionless Zel'dovich number to measure the influence of the said temperature dependence

$$\beta = E(T_b - T_u)/(\mathcal{R}T^2), \quad (1.2)$$

the thickness of the reaction region is of the order δ_T/β . Since $\beta \sim \mathcal{O}(10)$ for most fuels, this zone can usually be considered, for simplicity, as an infinitely thin surface that produces discontinuities in the fluid variables. Particularly, consuming upstream unburned reactants at a temperature T_u and leaving hot combustion products behind at a maximum temperature that depends on the heat of combustion of the fuel Q . Namely, T_b is the adiabatic flame temperature of a given mixture (Fig. 1.6 (a)), obtained under no loss of energy in the system, thus all the extracted heat from the chemical reaction is used to heat up the products.

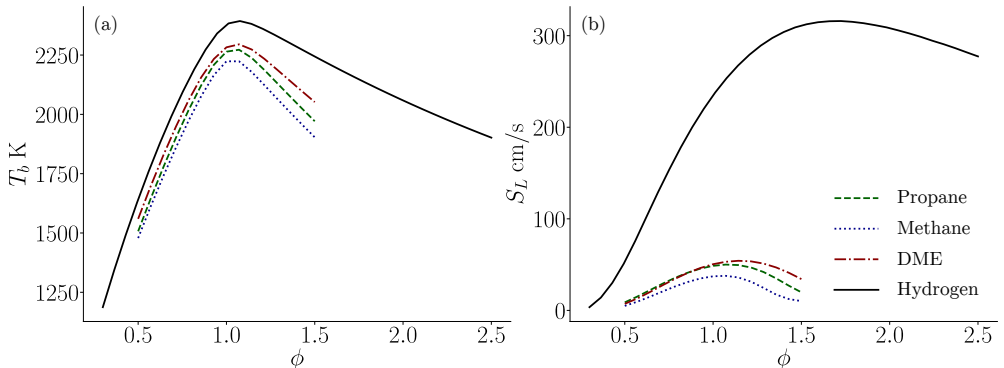


FIGURE 1.6 | (a) Adiabatic burning temperature T_b and (b) laminar burning velocity S_L calculated with Cantera for different premixed flames of propane, methane, DME and hydrogen at atmospheric pressure and $T_u = 298$ K.

The preheat zone is a region governed by convection and diffusion, which controls the propagation through the heating of reactants up to a sufficiently-high temperature for the reaction to begin. Therefore, the complete reaction wave propagates at a given speed –mixture, pressure and initial temperature dependent–, known as laminar burning velocity S_L (Fig. 1.6 (b)). To calculate its characteristic thickness and propagation velocity, one must take into account the energy released by the chemical reaction per unit area per unit time,

$$QY_F\Omega \left(\frac{\delta_T}{\beta} \right) = k_g \frac{(T_b - T_u)}{\delta_T}, \quad (1.3)$$

where k_g is the thermal conductivity of the fresh mixture, considered here constant with temperature. Also, for an isobaric process, the overall energy per unit mass of fuel added to the combustible mixture is

$$QY_F = c_p(T_b - T_u), \quad (1.4)$$

with c_p the specific heat at constant pressure of the fresh mixture, considered to be constant with temperature too. Identification of the previous equations yields the aforementioned thickness $\delta_T = \sqrt{k_g\beta/(c_p\Omega)}$. Furthermore, just by applying the conservation of mass for the fuel in a steady flow $\rho_u S_L = \Omega\delta_T$, being ρ_u the density of the unburned fresh mixture, we calculate the flame propagation velocity as

$$S_L = \frac{\sqrt{\Omega k_g / (c_p \beta)}}{\rho_u}, \quad (1.5)$$

obtaining a simple relation for the flame thickness,

$$\delta_T = \frac{D_T}{S_L}, \quad (1.6)$$

under the assumption of equidiffusive mixtures, with $D_T = k_g / (c_p \rho_u)$ the thermal diffusivity of the mixture. This simplified approach is good enough for a qualitative understanding of a premixed flame structure. The reader is invited to consult [12, 13], among others, for further detail.

Instabilities of premixed flames

Despite the promising aspects of using premixed flames, they present some drawbacks. Ideal considerations of totally planar premixed flames fail upon confrontation with reality, being innately unstable [13]. The following instabilities produce folding and wrinkling of the flame, strongly modifying its shape and dynamics. They can become an issue if they are not under control, decreasing the efficiency of the system or even causing an irreparable damage to the burners. Figure 1.7 shows the characteristic effects on the flame shape of the instabilities that are known to appear during the propagation of premixed flames:

- (a) *Darrieus-Landau* (DL). Premixed flames are inherently unstable due to the density jump across the reaction front [14, 15], from the fresh and heavy unburned mixture to the hot and light products.
- (b) *Rayleigh-Taylor* (RT). Gravity influences the propagation of flames due to buoyancy differences between light and heavy fluids [16, 17]. This effect is known to be destabilizing for upward-propagating flames, where the light gases (products) are under the heavy ones, and to produce an stabilizing effect to those moving downwards. The Froude number ($Fr^2 = S_L^2 / gh$), with g the acceleration of gravity and h the characteristic length (*i.e.*, the thickness of the burner), compares inertial to gravity-driven effects and characterizes the influence of this instability.
- (c) *Thermodiffusive* (TD). The competition between heat and mass diffusion is also a source of flame destabilization [18]. Its importance on the propagation of premixed flames is described by the Lewis number ($Le = D_T / D_i$), that compares thermal D_T to mass D_i diffusivities. However, this phenomenon is known to help stabilizing the flame front when $Le > 1$.
- (d) *Thermoacoustic* (TA). The unsteady release of heat by the chemical reaction couples with the acoustic waves present at confined or semi-confined combustion chambers, undergoing a feedback mechanism that strongly destabilizes the flame and makes it vibrate at the natural frequency of the combustion chamber [19, 20].

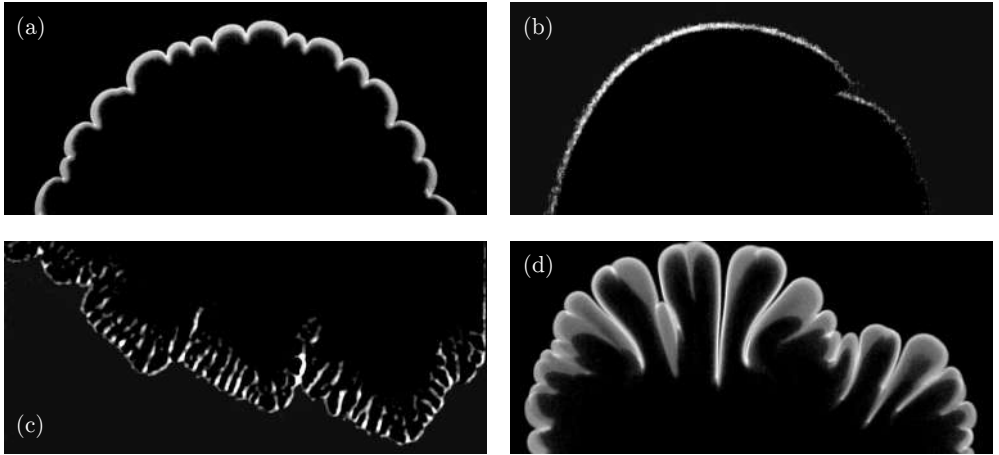


FIGURE 1.7 | (a) Lobes formed by the DL instability in a slightly rich methane flame propagating horizontally. (b) Bubble-shaped flame characteristic of the RT instability ($Fr^2 \sim 9 \times 10^{-3}$) found for an ultra-lean upward-propagating hydrogen flame. (c) Extremely wrinkled lean downward-propagating hydrogen-air flame front by the TD instability ($Le \sim 0.3$). (d) Finger-shaped vibratory rich DME flame propagating horizontally coupled with the acoustic waves found at the combustion chamber (TA).

- *Saffman-Taylor (ST)*. The viscosity jump between two fluids may be destabilizing [21] if the propagating fluid is less viscous than the quiescent one. We believe that for gaseous flames this phenomenon may only produce a stabilizing effect, as the propagating fronts leave behind hot combustion products that are more viscous than the unburned reactants. However, the relevance of this effect on flames is still open and in active discussion among the scientific community.

Understanding all these instability mechanisms is key to control any combustion process involving premixed flames, therefore improving the overall efficiency of any burning system. Moreover, some of them imply additional difficulties such as thermoacoustic instabilities, which may introduce a violent oscillatory motion of the flow that is transferred to the holding structure and can become dangerous, potentially leading to a catastrophic failure of the whole system. Furthermore, the possibility of finding new instability mechanisms is still open, mostly for alternative –not so common yet– fuels. Digging down to unknown burning conditions might show unpredicted flame propagation regimes that must also be reported, catalogued and understood.

1.2 Objectives

The main goal of this thesis is to study how different premixed flames of gaseous fuel-air blends propagate and destabilize when traveling in narrow geometries. In particular, we want to analyze and characterize experimentally how the following controlling parameters affect to the critical onset of thermoacoustic instabilities:

- *The effect of fuel properties and mixture composition.* In this work, hydrocarbons-, ether- and hydrogen-air mixtures are studied. They are chosen mostly because of their different diffusive properties, measured in terms of the Lewis number, and their potential application as future clean fuels. Additionally, we also change the composition of the mixture for each particular fuel, or equivalence ratio ϕ –defined as the relation between the actual fuel-to-oxidizer ratio to the stoichiometric one–, to determine its significance.
- *The effect of heat and acoustic losses.* To assess the main consequences of modifying the energy losses of the system, it is important to select wisely the geometry of the burner. Namely, the thickness of a thin channel will play a major role in modifying the relative heat losses and viscous damping of the flow.
- *The effect of gravity.* Buoyancy effects can be ruled out for horizontal vessels, where the transverse coordinate is of the order of millimeters. However, we can determine the influence of gravity by changing the direction of propagation of the flames, to be horizontal and vertical (both upwards and downwards).

Additionally, the importance of the flame shape (curvature, strain and effective burning surface) and differential diffusion regarding thermoacoustics will be studied. Also, it is interesting to analyze whether it is possible or not to appoint to an existing controlling parameter of the flames that could generally define the onset of thermoacoustic instabilities.

Finally, we want to introduce, report and explain two novel propagation regimes that were found for ultra lean hydrogen flames burning in very narrow channels. For these conditions, the high mass diffusivity of the fuel sustains the flames despite the high intensity of the relative heat losses to the surrounding walls. Understanding these phenomena is crucial for the security of hydrogen-based systems.

1.3 Experimental set-up

The study of flames in confined geometries is relevant to provide further insight on safety issues and undesired propagation of confined reactions in gaps, narrow channels and tubes. Also, it is interesting to the design and development of small-scale burners and the design and efficiency increment of internal combustion engines. It is widely-accepted that micro-combustion systems improved thanks to the study of numerous performance issues such as the flame instabilities listed before [22, 23], flame extinction and quenching [24], amongst others. The study of the propagation of premixed gaseous flames in narrow chambers is interesting to understand most of these phenomena, typically enhanced by the geometrical restrictions to the flow.

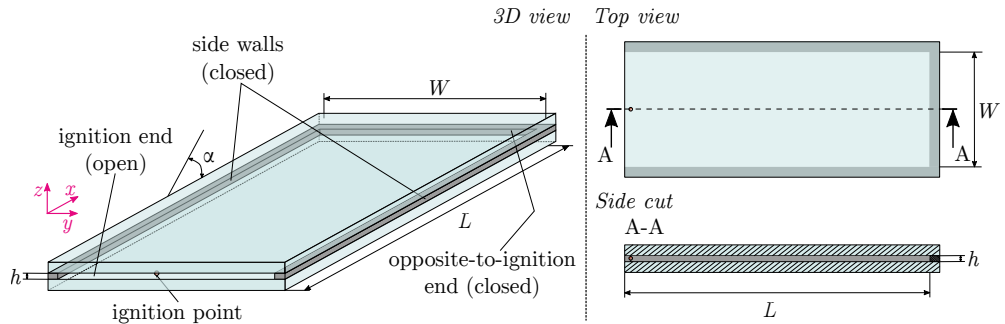


FIGURE 1.8 | Sketch of a Hele-Shaw (HS) cell modified to be used as a combustion chamber. The dimensions of the chamber are $L \times W \times h$ (Length \times Width \times Thickness). The angle between the horizontal and the cell is represented by α . Furthermore, we define here the coordinate system used for the whole experimental study.

Keeping that in mind, we chose to study, mostly experimentally, flames propagating in a Hele-Shaw (HS) cell to reach the proposed objectives of this thesis. This setup was originally used by Hele-Shaw [25] and Saffman and Taylor [21] to study viscous effects on different fluids. A HS cell (Fig. 1.8) is a simple domain formed by two parallel plates separated –ideally– by an infinitesimal gap. In real configurations, the gap between the plates h should be much smaller than both the length L and width W of the cell, that is $h \ll L \sim W$. Mathematically, the dynamics of the flow formed in the hollow gap of the cell can be formulated, in a simplified way, as a quasi-2D problem when the ratio $a = h/\delta_T \ll 1$ (see Appendix 5.A for further detail).

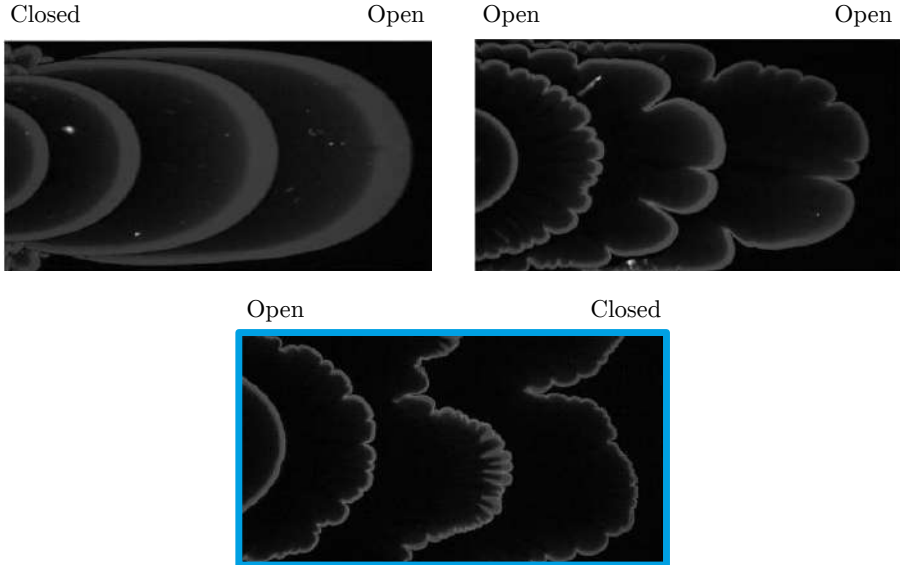


FIGURE 1.9 | Stoichiometric dimethylether (DME) flame shapes obtained with different boundary conditions [26]. The flames propagate from left to right and the upper comments define the geometrical boundary conditions at the ignition end (left) and the opposite-to-ignition end (right). The cyan rectangle highlights the chosen boundary conditions throughout the whole dissertation (Open - Closed) which promote the appearance of thermoacoustic instabilities.

There are additional reasons behind the choice of a HS cell as a burner. First, it is possible to investigate the effect of increasing heat and acoustic losses on the instability onset by decreasing the gap distance h between the parallel plates. These effects begin to be important when the thickness of the channel is below a critical value, which is determined by a compendium of properties involved in the process: the materials of the combustion chamber (represented mostly by their elasticity and heat conductivity), the relation between the characteristic time of the heat losses to the surrounding walls and the residence time of the propagating flame, *etc.* Second, for thicker channels, the reactive fronts behave in a similar qualitative way than for big-scale problems [27], allowing us to obtain lab-scale results that may be applicable to larger industrial systems. Third, its characteristic shape permits a complete visualization of nearly-two dimensional flames from several points of view: the top view, which is used for most of the recorded images (*e.g.*, Fig. 2.5), and the lateral view (*e.g.*, Fig. 2.6), obtained by recording the flame under a certain lateral angle. The combination of both provide additional and novel information to that obtained from the usual flames propagating in tubes.

Two different combustion chambers were built throughout the development of the thesis. Both follow the same general configuration sketched in Fig. 1.8, but show some discrepancies due to the available laboratory resources at Universidad Carlos III de Madrid, used to study the combustion of carbon-based fuels such as propane, methane and dimethylether (DME), and Karlsruhe Institute of Technology, focused on hydrogen flames. In addition to intrinsic conditions imposed by a thin Hele-Shaw cell, such as viscous stresses or heat losses to the plates, we were able to modify the boundary conditions that define the studied problem, by opening or closing the ignition or opposite-to-ignition end (the side walls always remain closed). The main instabilities arising at the front are strictly dependent on this choice (Fig. 1.9). With the aim of promoting the appearance of thermoacoustic instabilities, we opened the ignition end and closed the opposite one so that the flames propagate along the x -direction towards a closed wall in all cases, if not specified otherwise. This semi-confined configuration presents the best conditions as the pressure waves are amplified due to reflection at the closed end wall. Furthermore, the combustion chambers can be oriented to form a given angle α with the horizontal, to graduate the influence of gravity on the propagation of the flames, $g_{\text{eff}} = g \sin(\alpha)$. Given this definition, the effective gravity acceleration is negligible for horizontal propagation ($\alpha = 0^\circ$) and equals g and $-g$ for upward ($\alpha = 90^\circ$) and downward ($\alpha = -90^\circ$) propagation respectively.

1.4 Outline of the document

First, a general introduction has been presented in chapter 1, that highlights the need to study premixed gaseous flames of alternative fuels as part of the solution for the upcoming energetic problem, sets the objectives of this work and provides the reasons behind burning in such a particular geometry. Next, this thesis is divided into two thematic blocks that address the main unstable phenomena that arose during the experiments in the Hele-Shaw combustion chamber.

Part I analyzes thermoacoustic instabilities in the HS vessel for different fuels and conditions. In particular, chapter 2 examines the effect of the aforementioned parameters (*e.g.*, mixture composition, gap thickness and gravity) on the onset of thermoacoustic instabilities for hydrocarbon and ether flames. Chapter 3 considers only buoyant hydrogen lean flames and

goes into further detail about the influence of those parameters. Furthermore, chapter 4 provides a detailed discussion regarding the results, summarizes the main conclusions related to thermoacoustic instabilities in narrow channels and introduces the future work and open problems to be performed in forthcoming studies.

Part II addresses, to the best of our knowledge, two propagation regimes reported in this thesis for the first time. Here, we analyze in chapter 5 the predictions given by a numerical study of highly diffusive flames propagating under the effect of intense heat losses. Moreover, chapter 6 offers the experimental study of near-limit hydrogen flames that followed to check and verify the numerical predictions. Finally, the main conclusions obtained from the previous results are summarized in chapter 7, together with the future prospects needed to fully describe and understand the novel phenomena.

References

- [1] T. Appenzeller, Global warming has made iconic andean peak unrecognizable, *Science Magazine* (2019).
- [2] Y. Xu, V. Ramanathan, D. G. Victor, Global warming will happen faster than we think, *Nature* (2018).
- [3] P. Forster, A. Maycock, C. McKenna, C. Smith, Latest climate models confirm need for urgent mitigation, *Nature Climate Change* (2019).
- [4] Nasa global climate change, <https://climate.nasa.gov/>, accessed: 2019-12-03.
- [5] I. Rahman-Jones, Climate change: The cop25 talks trying to change the world, BBC (2019).
- [6] B. P. Energy Outlook, 2019 edition, London, United Kingdom, (2019).
- [7] O. Ellabban, H. Abu-Rub, F. Blaabjerg, Renewable energy resources: Current status, future prospects and their enabling technology, *Renewable and Sustainable Energy Reviews* 39 (2014).
- [8] J. Tollefson, The hard truths of climate change—by the publishers, *Nature* 573 (324–327) (2019).
- [9] I. Staffell, D. Scamman, A. V. Abad, P. Balcombe, P. E. Dodds, P. Ekins, N. Shah, K. R. Ward, The role of hydrogen and fuel cells in the global energy system, *Energy & Environmental Science* 12 (463–491) (2019).
- [10] B. Salvi, K. Subramanian, Sustainable development of road transportation sector using hydrogen energy system, *Renewable and Sustainable Energy Reviews* 51 (1132 - 1155) (2015). doi:<https://doi.org/10.1016/j.rser.2015.07.030>.
- [11] S. M. Correa, A review of nox formation under gas-turbine combustion conditions, *Combustion science and technology* 87 (329–362) (1993).
- [12] A. Liñán, F. A. Williams, Fundamental aspects of combustion (1993).

- [13] P. Clavin, G. Searby, Combustion waves and fronts in flows: flames, shocks, detonations, ablation fronts and explosion of stars (2016).
- [14] G. Darrieus, Propagation d'un front de flamme, *La Technique Moderne* 30 (18) (1938).
- [15] L. Landau, On the theory of slow combustion in: Dynamics of curved fronts (403–411) (1988).
- [16] R. Lord, Investigation of the character of the equilibrium of an incompressible heavy fluid of variable density, *Scientific Papers* (200–207) (1900).
- [17] G. I. Taylor, The instability of liquid surfaces when accelerated in a direction perpendicular to their planes. i, *Proceedings of the Royal Society of London. Series A. Mathematical and Physical Sciences* 201 (192–196) (1950).
- [18] G. I. Sivashinsky, Instabilities, pattern formation, and turbulence in flames, *Annual Review of Fluid Mechanics* 15 (179–199) (1983).
- [19] W. Mason, R. V. Wheeler, The propagation of flame in mixtures of methane and air. part i. horizontal propagation, *Journal of the Chemical Society, Transactions* 117 (36–47) (1920).
- [20] H. Coward, F. Hartwell, E. Georgeson, Studies in the mechanism of flame movement. part iv. the vibratory period, *Journal of the Chemical Society (Resumed)* (1482–1489) (1937).
- [21] P. G. Saffman, G. I. Taylor, The penetration of a fluid into a porous medium or hele-shaw cell containing a more viscous liquid, *Proceedings of the Royal Society of London. Series A. Mathematical and Physical Sciences* 245 (312–329) (1958).
- [22] M. Matalon, Flame dynamics, *Proceedings of the Combustion Institute* 32 (57–82) (2009).
- [23] M. Sánchez-Sanz, D. Fernández-Galisteo, V. Kurdyumov, Effect of the equivalence ratio, Damköhler publisher, Lewis publisher and heat release on the stability of laminar premixed flames in microchannels, *Combust. Flame* 161 (1282–1293) (2014).
- [24] M. Sánchez-Sanz, Premixed flame extinction in narrow channels with and without heat recirculation, *Combust. Flame* 159 (3158–3167) (2012).
- [25] H. S. Hele-Shaw, The flow of water (1898).

- [26] C. Vivanco-Silva, Estudio experimental de llamas de premezcla de dme, Trabajo fin de Grado (2018).
- [27] C. R. L. Bauwens, L. R. Boeck, S. B. Dorofeev, Understanding how mixture composition affects flame-acoustic interactions in large-scale vented explosions.

Part I

Thermoacoustic instabilities

"Bailas e faisme libre"

– Uxio Novoneyra (1966)

Opening remarks

The detailed physics behind the complex problem of acoustic-related instabilities in flames are still a kind of mystery. Part I aims to break down some knowledge barriers regarding acoustically self-excited flames of gaseous fuels in narrow channels, filling some existing gaps that would help to control and prevent this –mostly– undesirable phenomenon.

During our experimental tests, several conditions (*e.g.*, selected fuel, composition of the burned mixture, energy losses of the system and acceleration of gravity) were spotted as critical on the onset of thermoacoustics and the main characteristics of flames under their effect. We provide here a detailed dossier of their influence on acoustic-related instabilities. Additionally, we want to quantify the importance of the flame shape and how a particular front reacts to an external acoustic perturbation, trying to appoint to a controlling parameter that would determine whether a flame becomes stable or not.

This part is structured as follows to fulfill our objectives. Chapter 2 analyzes carbon-based fuels (propane, methane and dimethylether) with different properties, testing a wide variety of conditions to isolate the effects caused by the critical parameters listed before. After explaining our experimental setups and procedures, we burn horizontal flames to avoid a strong influence of buoyancy (*i.e.*, gravity) on the dynamics of the propagation, changing both the fuel and the composition of the mixture. Next, we analyze the importance of energy losses, such as heat or viscous dissipation. Next, we rotate the vessel and burn vertical-propagating flames (up and downwards) to assess the importance of the acceleration of gravity on thermoacoustics.

Chapter 3 follows the same structure but for lean hydrogen flames, that has its strong particularities when oxidizing, such as a high mass diffusivity. To close this part, chapter 4

discusses in detail the influence of the flame shape and preferential diffusion on thermoacoustics, listing later a number of conclusions that are reached on light of our results. Furthermore, we present our ideas for future prospects and introduce some open problems for which preliminary results have already been obtained.

CHAPTER 2

Thermoacoustic instabilities in hydrocarbon and ether gaseous flames

In the absence of a sudden technology breakthrough, oil, coal and natural gas will dominate the energy production during the upcoming decades (Fig. 1.4). The portfolio of alternative gaseous fuels, with better carbon footprints, has increased tremendously during the last years and, many of them, can be seen as energy vectors capable of taking renewable energies to non-electrified, power-starving applications. Low-carbon fuels (CH_4), gaseous ether (DME), biofuels and hydrogen are characteristic examples of the possible chemical compounds where wind or solar power can be stored for long periods of time. They offer to keep our energetic demand constant, or even rise it, while reducing the amount of pollutants responsible for the global warming, being CO_2 the most problematic species. Analyzing the dynamics of premixed flames of these fuels with air, and comparing them to those of more conventional fuels (*e.g.*, propane; C_3H_8), is important to promote their safe use. In particular, it is critical to understand the instabilities that may arise during their propagation (Fig. 1.7), as they have a strong influence on the outline of the flames and on their behavior, thus having a direct impact on the performance of any combustion-based system.

In particular, we address here the vibratory motion of premixed flames, firstly reported by Mallard and Le Chatelier [1]. The so-called thermoacoustic instabilities appear as a result of the coupling between the flames and the acoustic pressure waves that remain trapped in confined or semi-confined combustion chambers, which can potentially lead to critical failure of the system. Following the original Rayleigh's criterion [2], pressure waves are amplified –theoretically– if

they are in phase with the unsteady heat released by the flame. This transfer of energy between the front and the acoustic waves competes against the different damping mechanisms that arise in real configurations, such as viscous layers or heat losses. The competition between various effects may lead to an amplification, thus yielding a destabilizing effect, or to an attenuation of the acoustic waves. An extensive overview of the experimental, numerical and theoretical studies on the matter is given in the following paragraphs.

To begin with, first experimental studies reported the marked behaviour of oscillating flames under smooth and violent regimes [3, 4], and directly related it to acoustic coupling. Later, additional studies investigated the behaviour of premixed downward-propagating hydrocarbon flames in tubes [5–7], always moving towards the closed end of the chamber. In particular, Searby [6] described the development of thermoacoustic instabilities in propane flames traveling downwards in a tube with the ignition end open to the atmosphere. In a different experiment, Aldredge and Killingsworth [8] tested a premixed methane flame propagating downwards in a Taylor-Couette burner. In their experiments with methane, they found rich flames to be more stable than lean flames, an opposite behaviour to that of the propane flames reported by Searby. Additionally, they appointed to the Markstein number \mathcal{M} –to be discussed in chapter 4– as an important parameter for studying the onset of thermoacoustics. In turn, Yañez et al. [9] repeated the experiment in a wide quadrangular combustion chamber using hydrogen mixtures to find oscillating flames only for very lean mixtures. Modifying the boundary conditions, Connelly and Kyritsis [10] and Yang et al. [11] carried out experiments with propane flames propagating along narrow tubes open at both ends. As in the experiments by Searby, the flames propagate with large and small-amplitude oscillations depending on the stoichiometry of the mixture. Almarcha et al. [12], Gross and Pan [13] and Shariff et al. [14] studied experimentally flames of propane and hydrogen propagating in a Hele-Shaw cell open at the ignition end. Nobody reported any oscillatory phenomenon in their experiments. However, two main regimes of the acoustic-driven oscillatory flames are recurrently found by the former authors as a result of the aforementioned coupling mechanism: the primary instability, a smooth and unwrinkled front vibration, and the secondary instability (also referred to as self-excited parametric), violent pulses of the corrugated front. Since the work on pyro-acoustic interaction presented in [15], it seems clear that the secondary acoustic instability is caused by pre-existing finite-amplitude acoustic oscillations and, therefore, a significant amount of work has been dedicated to explain

their origin [16, 17]. Two mechanisms were considered to explain the generation of the primary acoustic instability in tubes: the direct sensitivity of the reaction rate to acoustic pressure and the variation of the flame front area induced by acoustic acceleration. A detailed account of the progress on flame thermoacoustic instabilities in tubes can be found in the book by Clavin and Searby [18].

On behalf of numerical studies, Petchenko et al. [19] found again two different oscillatory regimes, attributed to flame-acoustics resonance, in a flame propagating towards the closed end in a narrow channel. According to their results, the acoustic oscillations produce an effective acceleration field at the flame front leading to a strong Rayleigh-Taylor instability which intensely wrinkles the flame front increasing the rate of reaction. Later, in a paper by the same author [20], the effect of the parameter $a = h/\delta_T$ was included, being h and δ_T the channel and flame thickness respectively. According to their results, the oscillations of the flame become stronger in wider domains, inducing flame folding in sufficiently wide tubes. On the other hand, small-amplitude flame oscillations were obtained in their calculations even in very narrow tubes $a = 10$. However, Kurdyumov and Matalon [21] found a non-oscillatory propagation speed for a flame advancing towards a closed end when solving the same problem numerically in the limit of very narrow channels $a \ll 1$ and including the effect of gas compressibility in their formulation. Fernández-Galisteo et al. [22] used the low-Mach number approximation $M = S_L/c \ll 1$ to compute numerically a flame propagating in a Hele-Shaw cell in the limit $a \ll 1$. They found instabilities that wrinkled the flame increasing the surface area and the propagation speed but, since they neglected the compressibility of the gas, they could not reproduce the acoustic variations affecting the flame.

Finally, on the account of theoretical studies, the first analytical models to explain thermoacoustic instabilities appeared under the context of project SQUID after World War II by Markstein [23, 24], who proposed the parametric instability driven by an imposed oscillating flow interacting with the flame [25]. His ideas were accepted and later revisited by other authors [8, 15]. Their analyses lead to a derivation of Mathieu's equation under several strong assumptions (*e.g.*, infinitely thin reaction region and equidiffusive mixtures) to define stability maps of the form shown in Fig. 2.1, which link the amplitude and frequency of the oscillatory velocity and the wavenumber of the perturbation. The derived stability diagrams were found to be strongly affected by diffusive and curvature effects and therefore controlled by the Markstein

number \mathcal{M} . However, these studies focus on the stability of the flame response upon an external imposed periodic acoustic field of relatively small amplitude, also referred to as parametric instability. The self-excited acoustic oscillations of a flame –the ones addressed here– were only explored theoretically in recent studies [26, 27] as an effort to extend the parametric instability case.

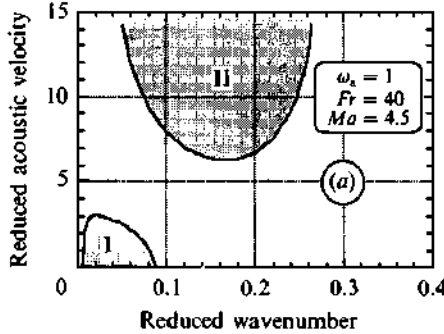


FIGURE 2.1 | Stability diagram which relates the velocity derived from acoustics and the wavenumber of the perturbations at the fronts obtained via the derivation of Mathieu’s equation for a parametric oscillatory instability. Here, I and II represent the primary and secondary thermoacoustic instability regimes respectively. The blank region is found to be stable. The figure is taken from [15], $Ma = \mathcal{M}$ is the Markstein number, $\omega_a = \omega$ is the angular frequency and Fr the Froude number.

Most of the experimental, theoretical and numerical studies found in the literature focused their attention on flames propagating in tubes. We present in this chapter an experimental study of premixed flames propagating in a quasi-two-dimensional geometry, where the viscous damping mechanisms can be adjusted by changing the channel thickness and visual inspection can provide quantitative data. We aim to contribute to the understanding of the transition between the primary and secondary instabilities for different gaseous hydrocarbons and ether fuels, chosen mostly because of their unalike diffusive characteristics (*i.e.*, Lewis number). We first address the effect of the mixture composition for all the selected fuels considering non-buoyant conditions, that is $\alpha = 0^\circ$ or horizontal channels. Additionally, the effect of the combustion chamber thickness h is analyzed, first introducing an order of magnitude analysis to estimate the importance of heat and viscous dissipation, being later supported by non-buoyant experiments done with DME. Finally, the influence of gravity is checked by positioning the combustion chamber vertically. With this modification, we can assess its importance for downward ($\alpha = -90^\circ$) and upward-propagating ($\alpha = 90^\circ$) flames.

2.1 Experimental setups and procedures

The experimental setup used for the study of non-buoyant flames was designed and built at the Universidad Carlos III combustion laboratory, sketched in Fig. 2.2. The combustion chamber is formed by two flat plates disposed horizontally ($\alpha = 0^\circ$) and separated by a PMMA hollow frame, enclosing a maximum volume of $L \times W \times h = 900 \times 500 \times 10 \text{ mm}^3$. Nevertheless, the observation length of the chamber from the glow plug to the opposite end is 800 mm. The top cover is a 19 mm-thick tempered-glass plate while the lower one is a rigid aluminum table insulated with a 1-mm vinyl layer. The gap between the plates can be varied from 10 to 1 mm by staking 3-mm-thick PVC laminae inside the hollow frame. The chamber is filled with a fuel-air mixture prepared before injection using two mass flow controllers (Sierra SmartTrak 100 for fuel and Omega FMA5418A 0-5 slm for air) to regulate its composition.

Non-buoyant flames

The experimental procedure starts by injecting the mixture into the chamber at the ignition end, *via* four regularly-spaced injection ports. During the charge of the reactants, the ignition end of the vessel is kept sealed while the opposite end is opened for venting. Upon the complete charge, when the stopcock is closed, both ends are shut to allow the gases to come to rest. Then, the ignition end is reopened and the mixture is ignited using a glow plug (BOSCH Duraspeed) powered with an amount of electrical energy that is held constant for all the experiments of a determined fuel. The whole section $W \times h$ at the ignition end is available to freely vent the high-temperature combustion products off the chamber. No valve nor gas extraction device was used, avoiding any possible disruption of the exhaust gases outflow.

The luminous emissions of the flame are recorded with a high-speed camera (MEMRECAM HX-3) shooting at 4000 fps, if not specified otherwise. The experimental setup allows recording videos from two points of view to capture both the top and side views of the flames, as shown in Fig. 2.2. The top view is used to obtain accurate quantitative data from the recording (*e.g.*, oscillation frequencies, burned volume fraction, flame velocity, *etc.*). The side view offers a novel three dimensional perspective of the front that reveals important features of the flame propagation. Simultaneously, the acoustic signal is recorded using a microphone located at the open ignition end. Image and audio post-processing analyses are detailed in Appendix 2.A.

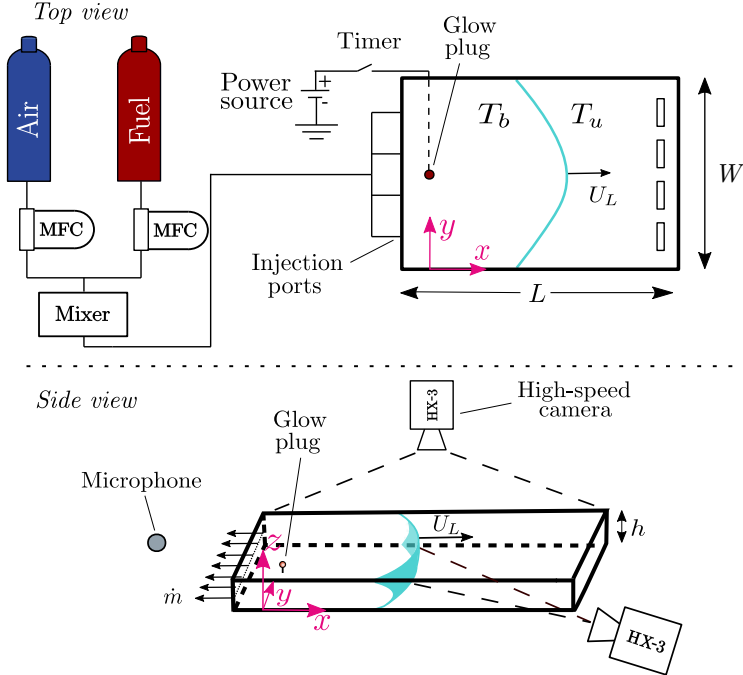


FIGURE 2.2 | Schematic representation of the horizontal ($\alpha = 0^\circ$) experimental apparatus. In the figure we depict the top and side view of the Hele-Shaw cell indicating its dimensions $L \times W \times h$, the location of the glow plug and the different positions of the high-speed camera to record the flame from two different points of view. In the figure, the black arrow lines located at the ignition end indicate the flow \dot{m} of high-temperature gas off the Hele-Shaw cell.

Buoyant flames

The effect of gravity is assessed by testing flames that propagate vertically. The experimental setup used for this purpose is the Hele-Shaw chamber ($\alpha = \pm 90^\circ$) described in Fig. 2.2, in which we substituted the insulating layer by a 10-mm-thick PVC plate and changed the position of the pressure sensor, now located inside the combustion chamber instead of being outside the exhaust section. Likewise, the vertical experiments are only recorded in a perpendicular view of the chamber at 1000 fps (Fig. 2.3 (a)). Additionally, some equipment improvements and fully automation of the experimental procedure modified the holding structure of the combustion chamber (from Fig. 2.3 (b) to (c)) [28]. We are aware of a very strong influence of the structure stiffness on the onset and development of thermoacoustic instabilities, an aspect that has only been phenomenologically explored by [29] and [30] and is still open

to contributions (chapter 4, **Future work**). We therefore know that the results presented in this section are found under somehow different structural conditions compared to those of non-buoyant flames, yielding different quantitative results (*e.g.*, equivalence-ratio transition point, maximum acoustic pressure, *etc.*) but capturing the overall qualitative nature of the phenomena. Furthermore, the experimental procedure requires some modifications as gravity is no longer negligible. The main differences appear when filling the chamber and igniting the mixture. Note that the upcoming buoyancy-driven phenomena appear independently on the burning conditions. However, they act in an opposite way for up- and downward-propagating tests, as the injection ports and the glow plug are always located at the ignition end. The reader shall note that, this end is placed at the top (bottom) of the geometry when the flames propagate downwards (upwards).

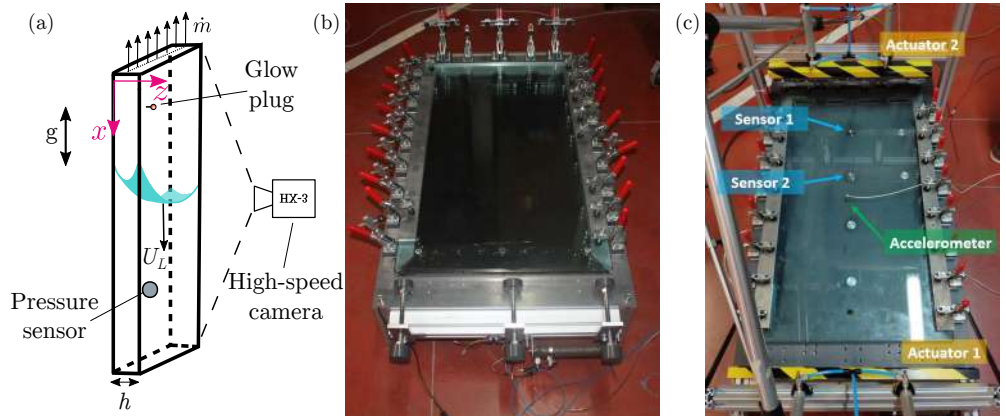


FIGURE 2.3 | (a) 3D sketch of the vertical ($\alpha = \pm 90^\circ$) experimental setup. (b) Apparatus used for non-buoyant tests. (c) Resultant setup after the modifications listed in [28].

The filling of the chamber succeeds when injecting a methane-air mixture for a downward-propagating flame test if we keep the previous filling boundary conditions, closed ignition end and the opposite-to-ignition end open. However, it fails when feeding the chamber with propane and DME blends. Why? The brief answer: buoyancy. More in detail, gravity acts on the fuel-air mixtures while injecting them into the combustion chamber containing quiescent air, and generates a buoyancy-induced velocity that makes them move preferentially upwards when they are lighter (methane) or downwards if heavier (propane and DME) than air.

To estimate this effect, consider the best case scenario where a lean methane ($\rho_{CH_4} = 0.656 \text{ kg/m}^3$) and air ($\rho_{air} = 1.225 \text{ kg/m}^3$) mixture ($\phi \sim 0.6$) is injected in the combustion chamber at ambient conditions. Keeping a constant air mass flow rate of $\dot{m}_{air} = 2.88 \text{ g/min}$, the amount of fuel required is $\dot{m}_{CH_4} = 0.1 \text{ g/min}$, and therefore the average density of the mixture yields $\rho_u = 1.206 \text{ kg/m}^3$, very similar to that of air but sufficient to introduce stratification problems. The buoyancy-induced upwards velocity of such mixture is $|U_{strat}| \sim \sqrt{(1 - \rho_u/\rho_{air})gh} \sim 0.04 \text{ m/s}$. Given its magnitude and the long filling times of our experimental procedure ($t_{fill} = 120 \text{ s}$), stratification should be considered during the tests. This would be the slowest velocity of all the tested mixtures, finding downward-induced speeds up to 0.09 m/s if rich ($\phi = 1.2$) DME mixtures are injected.

Therefore, the ascending motion of the light mixture is neutralized by the presence of a wall at the top of the vessel. However, the heavy mixtures preferentially move downwards and would directly leave the Hele-Shaw cell through the open bottom orifices and the vessel would never fill. To avoid this, we switch the filling boundary conditions, the opposite-to-ignition end is closed and the ignition end is kept open when working with heavy fuels. Moreover, it is important to remark that the opposite scenario is found when the flames propagate upwards. To make it clear, we close the ignition end and open the opposite-to-ignition end when feeding the chamber with heavy mixtures and switch the geometrical boundary conditions when using methane.

Regarding ignition, the glow plug heats up the mixtures at its surroundings, creating a buoyant flow (upwards) close to the heat source. The most critical conditions appear when analyzing downward-propagating flames. It is important to impede the preheated mixture *exodus* from the combustion chamber prior to ignition. For that, instead of reopening the ignition end once the filling is completed, we now keep it closed while the mixture does not reach the required temperature, which depends on its composition. Attention must be taken to manually reopen the ignition end just before the flame begins to propagate to maintain the same boundary conditions as for the non-buoyant case. It should be kept in mind that the flames always propagate from an open towards a closed end (Fig. 1.9). For upward-propagating cases, the heated mixture ascends within the chamber and there is no need to change the ignition procedure. Nevertheless, this phenomenon also modifies the initial conditions at the vessel and might be of importance on the propagation dynamics of the flames (Fig. 2.20).

Tested mixtures and their properties

A summary of the properties of the flames tested in our experiments is included in Table 2.1. This table encompasses the planar burning velocity S_L , the flame thickness $\delta_T = D_T / S_L$ and the adiabatic flame temperature T_b at equilibrium for propane, methane and DME, calculated using COSILAB.

With the idea of contributing to the understanding of the transition from the primary to the secondary instability described in [6], we also added in Table 2.1 the effective Lewis number Le_{eff} and the Markstein number M , proposed by [8] as an important parameter to explain the effect of acoustic fluctuations on local flame stretch. The values of the Markstein number are taken from [31] for methane and propane and from [32] for DME. The effective Lewis number Le_{eff} , introduced by [33] and [34], controls the amplification of the hydrodynamic instability due to diffusion effects [33]. It is calculated as

$$Le_{eff} = \frac{Le_O + (1 - \tilde{\phi})Le_F}{2 - \tilde{\phi}} \quad (2.1)$$

for lean flames and

$$Le_{eff} = \frac{Le_F + (1 + \tilde{\phi})Le_O}{2 + \tilde{\phi}} \quad (2.2)$$

for rich flames, with $\tilde{\phi} = \beta(\phi - 1)$, where the subscripts O and F refer to oxidizer and fuel respectively [31].

2.2 Effect of the mixture composition for non-buoyant flames

In this section, we burn different fuels in an horizontal Hele-Shaw combustion chamber, selected by their diffusive properties, that are measured in terms of the Lewis number Le , and for being characteristic examples of a group of fuels. Propane ($Le \sim 1.8$) represents conventional hydrocarbon gaseous fuels, methane ($Le \sim 1$) is a low-carbon gas which can lead the upcoming energetic transition and DME ($Le \sim 1.7$) is a gaseous ether bio-fuel. Furthermore, the mixture composition (*i.e.*, the equivalence ratio ϕ) is changed for each particular fuel to assess its effect on the onset of thermoacoustic instabilities.

TABLE 2.1 | Properties of the fuel-air mixtures calculated at room temperature $T_u = 298$ K with $E = 125.4$ kJ/mol [35] for C_3H_8 (propane), $E = 132.13$ kJ/mol [36] for CH_4 (methane) and $E = 250.8$ kJ/mol for DME, calculated by fitting the experimental values of the planar flame speed S_L measured by [32], to the flame speed calculated using an Arrhenius expression for the reaction rate Ω , with $A = 1 \times 10^{31}$ in $\text{cm}^3/\text{mol s}$ and $\mathcal{R} = 8.31$ J/mol K. The adiabatic flame temperature T_b and the planar flame speed S_L are calculated using the San Diego mechanism. For DME flames, the values of \mathcal{M} for $\phi < 0.7$ are extrapolated. The thermal flame thickness is given by $\delta_T = D_T/S_L$ with $D_T = 2 \times 10^{-5} \text{ m}^2/\text{s}$. The small-amplitude oscillations are observed in flames with the equivalence ratios highlighted in gray.

	ϕ	T_b [K]	S_L [cm/s]	δ_T [mm]	Le_F	Le_O	Le_{eff}	β	\mathcal{M}
C_3H_8	0.70	1884.80	21.95	0.09	1.85	1.06	1.66	7.10	3.16
	0.80	2048.10	28.91	0.07	1.84	1.06	1.61	6.63	2.98
	0.87	2143.76	33.17	0.06	1.83	1.06	1.55	6.08	2.92
	0.90	2184.90	35.00	0.06	1.83	1.05	1.53	6.28	2.79
	1.00	2271.50	38.91	0.05	1.82	1.05	1.44	6.08	2.35
	1.10	2268.10	40.50	0.05	1.81	1.05	1.34	6.09	1.96
	1.20	2200.60	38.62	0.05	1.80	1.04	1.27	6.24	1.77
	0.70	1833.71	15.41	0.13	0.98	1.10	1.01	7.26	0.75
CH_4	0.80	1992.31	24.12	0.08	0.98	1.10	1.02	6.78	0.77
	0.90	2130.22	32.50	0.06	0.98	1.10	1.03	6.42	0.81
	0.95	2176.19	34.79	0.06	0.98	1.09	1.03	6.33	0.81
	1.00	2222.16	37.08	0.05	0.98	1.08	1.03	6.19	0.88
	1.10	2206.32	35.01	0.06	0.98	1.08	1.04	6.23	0.96
	1.20	2132.02	32.18	0.06	0.98	1.09	1.06	6.41	1.02
	0.50	1563.20	7.09	0.28	1.82	1.06	1.71	10.41	4.09
	0.55	1669.40	11.74	0.19	1.81	1.06	1.69	9.91	3.90
DME	0.60	1756.30	15.55	0.13	1.80	1.06	1.67	9.51	3.72
	0.70	1932.60	24.79	0.08	1.79	1.05	1.63	8.80	3.35
	0.80	2088.00	33.06	0.06	1.78	1.04	1.58	8.26	2.98
	0.90	2212.60	39.62	0.05	1.76	1.04	1.50	7.86	2.39
	1.00	2289.80	44.04	0.05	1.75	1.03	1.39	7.64	1.86
	1.10	2296.20	45.97	0.04	1.74	1.03	1.28	7.62	1.75
	1.20	2246.00	45.13	0.04	1.73	1.02	1.22	7.77	1.61

2.2.1 Propane flames

The aforementioned methodology is first applied here to propane-air mixtures, as a representative example of conventional hydrocarbon gaseous fuels. The evolution with time of both the burned volume and the flame velocity are plotted versus time in Fig. 2.4. The burned volume fraction of burned gases is defined here as the ratio between the volume of the chamber occupied by the high-temperature gas V_b , obtained from the images, and the total chamber volume $V_{tot} = W \times L \times h$. Furthermore, the flame velocity is calculated assuming a flat flame with the same burned volume as observed in the experiments $U_L = (Wh)^{-1} dV_b/dt$.

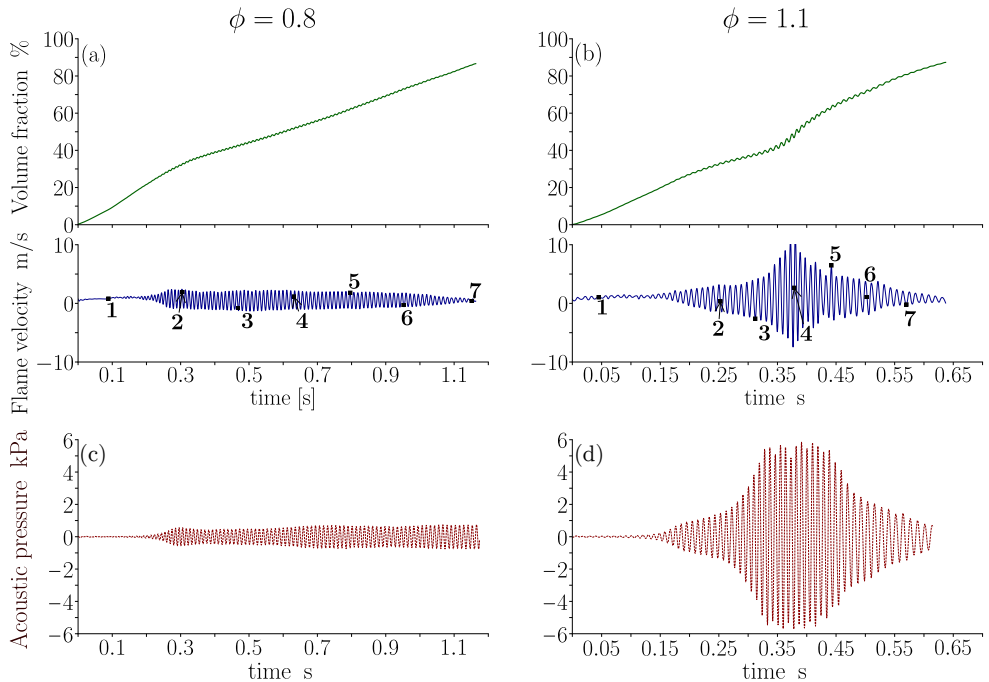


FIGURE 2.4 | (a) and (b) Time evolution of the relative burned volume V_b/V_{tot} (upper thick-solid lines) swept by a propane-air flame and the flame velocity calculated from the burned volume $U_L = (Wh)^{-1} dV_b/dt$ (lower thin-solid lines). The error in the determination of the equivalence ratio is ± 0.05 and the maximum uncertainty of the burned volume measurements is $\pm 2.75\%$. (c) and (d) Acoustic pressure as a function of time.

The data plotted in this figure illustrates the two different oscillatory behaviours measured in our experiments. The lean flame, Fig. 2.4 (a) and (c), propagates along the Hele-Shaw cell with a propagation velocity that oscillates around a positive mean value. The amplitude of the

oscillation is small, of around 8 mm, and remains stable until the flame reaches the end of the combustion chamber.

Contrarily, the amplitude of the flame oscillation is as large as 30 mm for rich-enough mixtures, inducing changes of around 2.5% in the burned volume fraction, with peak velocities close to 10 m/s, as obtained via image analysis in Fig. 2.4 (b). Similarly to the experiments by Searby [6], the average propagation velocity increases during this phase, proved by the increment of the slope at approximately halfway of the chamber in Fig. 2.4 (b). The transition between oscillatory regimes takes place suddenly at a critical equivalence ratio measured to be $\phi_c = 0.87 \pm 0.05$. Based on our experimental observations, we consider that a flame experiences secondary acoustic oscillations when the over-pressure peak exceeds 1 kPa approximately, the flame position (Fig. 2.4 (a) and (b)) shows a sudden slope change while transitioning and there are important modifications in the overall outline of the front (Fig. 2.5 (b)).

The oscillations of the flame can be compared to the acoustic pressure registered by the microphone, plotted in Fig. 2.4 (c) and (d). After an initial period, during which the microphone records the ignition event, the device measures the sound generated by the flame. This figure shows a sudden increase in the amplitude of the acoustic pressure that becomes an order of magnitude larger for $\phi = 1.1$ ($p_{max} \sim 6$ kPa) than for $\phi = 0.8$ ($p_{max} \sim 0.5$ kPa). The match between the signal from the microphone and the flame oscillations suggests a coupling between the sound waves propagating within the chamber and the behaviour of the flame that will be further examined later.

To illustrate the change in the flame structure, we show in Figs. 2.5 and 2.6 the top and lateral views of the flame luminous emissions recorded by the camera for lean ($\phi = 0.8 < \phi_c$) and rich ($\phi = 1.1 > \phi_c$) propane-air flames propagating, from left to right, towards the closed end of the chamber. The superposed images correspond to the times marked with the respective numbers in Fig. 2.4 (a) and (b).

As it can be seen in Fig. 2.5 (a), 70 ms after ignition (stage 1) the lean flame ($\phi = 0.8$) wrinkles to form medium-size cells ($\bar{\lambda} \sim 18$ mm $> h$) as a consequence of the Darrieus-Landau instability. Soon after, at approximately 300 mm from the ignition source, the flame starts a small-amplitude oscillation that lasts until it reaches the end of the chamber. The flame is flattened in the $x - y$ plane by the acoustic waves, undergoing a smooth oscillatory motion thus slowing its propagation rate down from $U_L = 1$ m/s to $U_L = 0.44$ m/s, still faster than

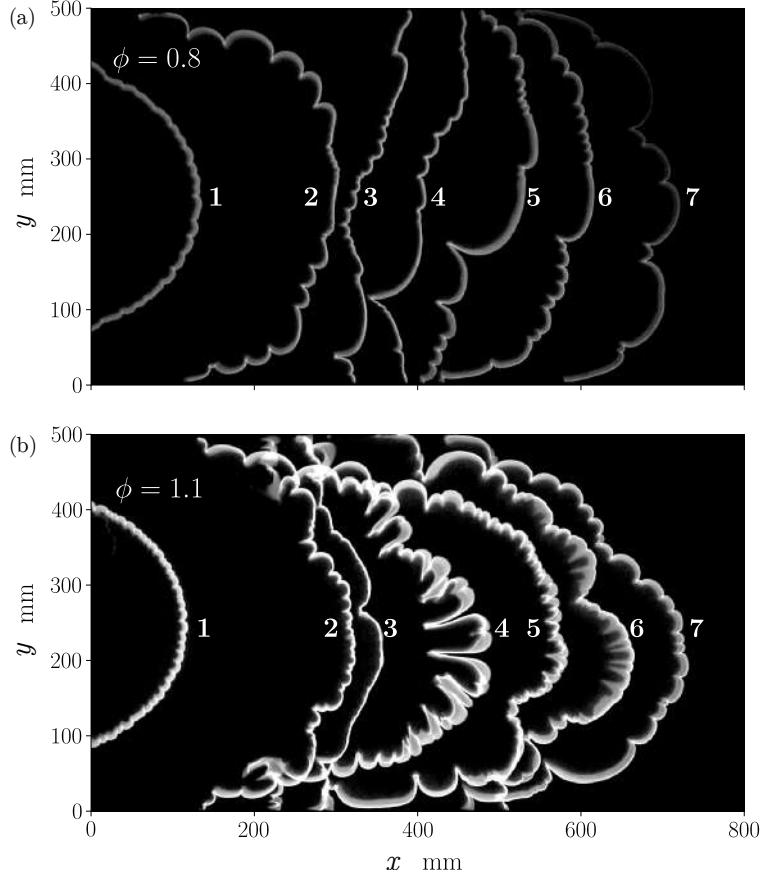


FIGURE 2.5 | Luminous emissions of a (a) $\phi = 0.8$ and a (b) $\phi = 1.1$ flame recorded by the high-speed camera at the times indicated by the numbers 1 to 7 included in Fig. 2.4.

the velocity of a laminar planar flame ($S_L = 0.28$ m/s). At this stage, neither the form of the flame nor the size of the cells change substantially, as inferred also from a side view of the flame displayed in Fig. 2.6 (a). The flame-front cusps, as seen from above, form and merge in a similar way as shown by Almarcha et al. [12] in a downward-propagating propane flame with $\phi = 0.6$, despite the fact that no oscillations of the front were reported there.

The flame-propagation dynamics change drastically in richer mixtures, as can be seen in Fig. 2.4 (b) and (d) for a rich propane flame $\phi = 1.1$. At the first instants, 40 ms after ignition (stage 1), smaller cells than those found for leaner flames are formed on the reaction surface ($\bar{\lambda} \sim 11$ mm $\sim h$) and it undergoes an oscillation of small amplitude, characteristic of the

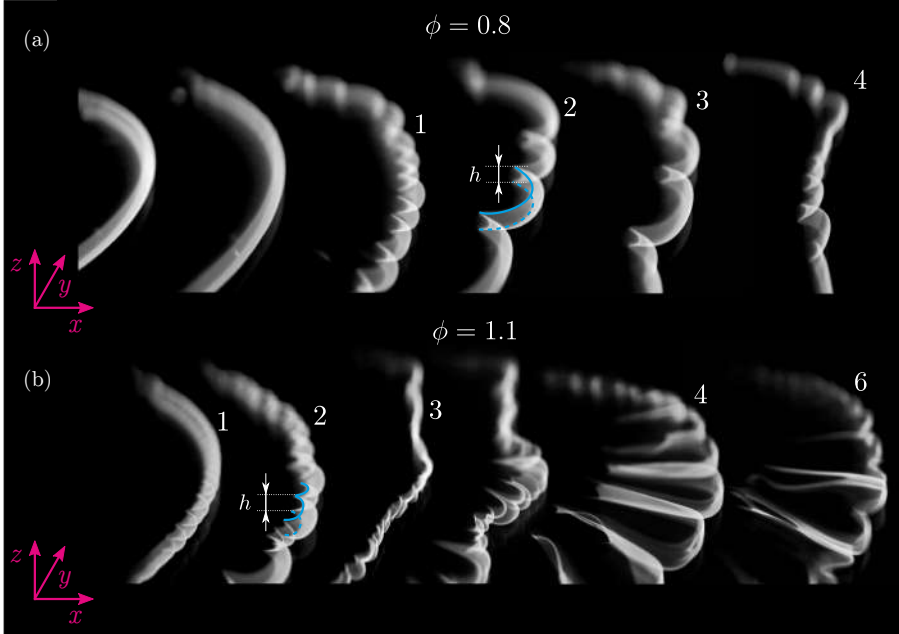


FIGURE 2.6 | Side view, with the camera placed laterally as indicated in the sketch of Fig. 2.2, of two propane flames with $\phi = 0.8$ and $\phi = 1.1$ and a cell thickness of $h = 10$ mm. The images displayed in this figure and those shown in Fig. 2.5 are taken in different runs of the experiment. The numbers in the image indicate that the flame is approximately at the same stage within the Hele-Shaw cell than the flame with the same number in Fig. 2.5. The solid and dashed cyan lines indicate where the flame touches the upper and lower horizontal plates, respectively.

first thermoacoustic instability, that flattens the flame before reaching the first quarter of the chamber. Right after, when the reactive front progresses towards the half of the chamber, the oscillations grow rapidly in amplitude and frequency, accelerating the flame which adopts a marked cellular finger-like shape as observed at stage 4 in Figs. 2.5 (b), 2.6 (b) and 2.7.

Deeper understanding is achieved by observing the shape of the flame in the transverse direction to the flame propagation (coordinate z). To do so, we placed the high-speed camera laterally under a certain angle. The side views of both lean and rich flames at their early stages are included in Fig. 2.6 (a) and (b) respectively. In these flames, the Darrieus-Landau instability induces the formation of cells, smaller as the mixture gets richer, that wrinkle the flame in the x - y plane. A smooth parabolic shape in the transversal z -direction, convex towards the fresh mixture, is kept in the early stages of the propagation for both lean and rich mixtures, as can

be appreciated in Fig. 2.6. Afterwards, for the lean flame (a), the same parabolic shape is conserved all along its way. On the other hand, the rich flame (b) flattens in both transverse and span-wise directions as the flame reaches 350 mm of the chamber length (stage 3), consequence of the interaction of the flame with the acoustic waves [6, 8]. More detailed photographs of the flame shape during an oscillation cycle performed at this stage are displayed in Fig. 2.7 (a). In this figure, we see that the flame front becomes a thin reaction region, nearly confined in the y - z plane, and shows small bulges on its surface as a consequence of a wrinkling instability that seems to enhance the oscillatory motion. In the next frames of this picture, the size of the corrugations increases and the flame accelerates building up the pressure in the confined fresh gases before retreating to a new cycle start in the form of an almost-planar wrinkled surface.

Returning to Fig. 2.6 (b), we can track clearly how the small-sized bulges, formed on stage 3, grow across the flame surface, deforming it until it adopts a finger-shaped structure (stage 4). Later on, the flame initiates the high-amplitude oscillations that extend the reaction front further towards the high-temperature gas region (stages 4 and 6). Again, we show in Fig. 2.7 (b) a sequence of detailed photographs of the flame during an oscillation cycle once the finger-shaped structure has been developed. During the oscillation, the portion of the flame located at the foremost position (indicated by arrows in the figure) gets delayed forming funnels pointing towards the burned gas during the drawing back of the flame. The violent oscillations continue until the flame reaches the end of the chamber, where small-amplitude vibrations are recovered.

Oscillation frequency analysis

The comparison between the flame velocities and the acoustic waves shown in Fig. 2.4 suggests a coupling between the two signals. To further investigate this aspect, we represented the Fourier spectrograms of a lean $\phi = 0.8$ (left panels) and a rich $\phi = 1.1$ (right panels) propane flame in Fig. 2.8. This figure displays a contour map of the evolution with time of the power level $P = 20 \log_{10} (\mathcal{A}/\bar{\mathcal{A}})$ [dB] stored in every frequency for an oscillatory signal with an instantaneous amplitude \mathcal{A} and average amplitude $\bar{\mathcal{A}}$. According to the color map chosen, the darker the color the more energy is stored in the corresponding frequency. Figures 2.8 (a) and (c) and 2.8 (b) and (d) show the Fourier spectrograms of the burned-area oscillations of the flame images f_p and of the sound signal f_s respectively.

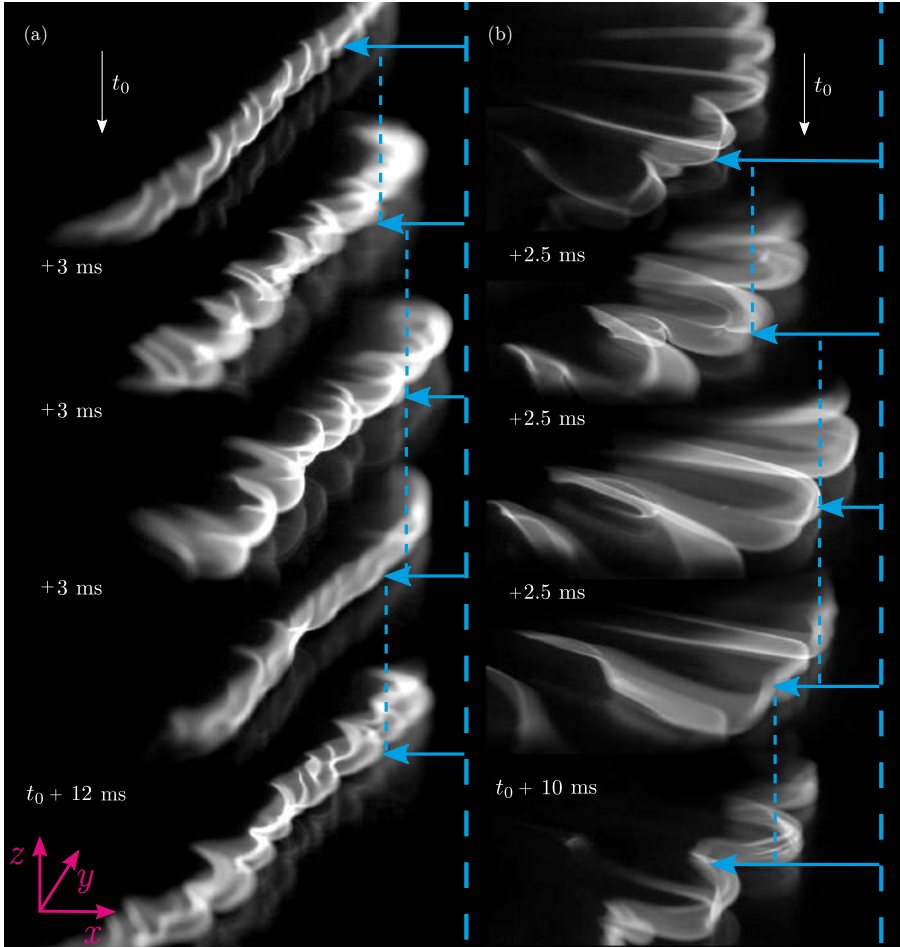


FIGURE 2.7 | Time sequence illustrating one oscillation cycle of a rich propane flame (a) in the transition stage from the primary to the secondary instability and (b) once the high-amplitude oscillations are fully developed. Vertical dashed lines establish a common reference for the displacement along each cycle.

For lean propane flames ($\phi = 0.8$), small-amplitude oscillations appear at $t_1 \simeq 0.2$ s when the reaction front reaches 200 mm of the total chamber length, at a frequency around 100 Hz that coincides with the frequency of the recorded sound. As the propagation continues along the chamber, the frequency of both the flame oscillations and the pressure wave signal reduces continuously to reach a minimum of 80 Hz at $x = L$. In Fig. 2.9, we plot the Fourier spectra at $t_1 = 0.3$ s, $t_2 = 0.6$ s and $t_3 = 0.9$ s comparing the flame-position oscillation and the sound level, where the peak amplitudes match the same frequencies.

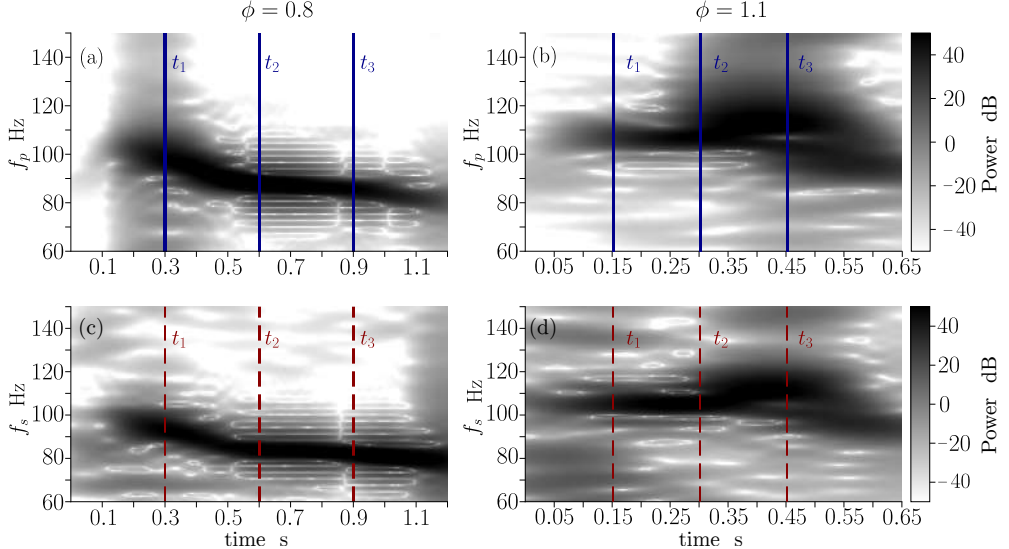


FIGURE 2.8 | Fourier spectrograms of the flame position f_p and of the sound level signal f_s for a lean $\phi = 0.8$ (a) and (c) and rich $\phi = 1.1$ (b) and (d) propane-air flame.

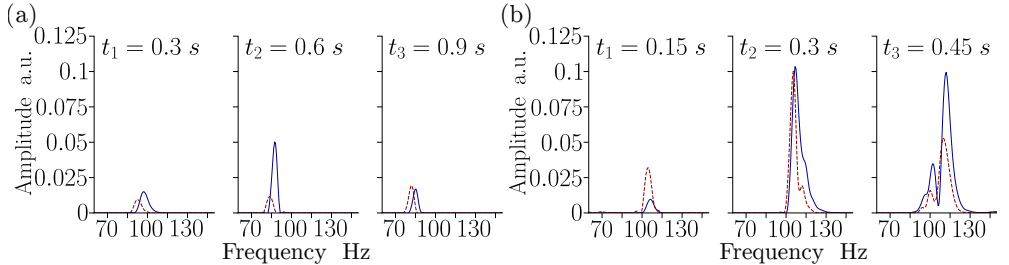


FIGURE 2.9 | Fourier spectra of the flame position (solid lines) and of the sound level (dashed lines) signals at times $t_1 = 0.3$ s, $t_2 = 0.6$ s and $t_3 = 0.9$ s for the lean flame (a) and $t_1 = 0.15$ s, $t_2 = 0.3$ s and $t_3 = 0.45$ s for the rich flame (b) indicated in Fig. 2.8. The error of the frequency measurements is ± 3 Hz.

As expected, rich propane flames ($\phi = 1.1$) oscillate with small amplitudes at a frequency around 100 Hz, until the flame-front arrives at the half of the chamber. At this time, the secondary instability emerges and the flame responds undergoing large-amplitude oscillations at frequencies ranging from 100 to 115 Hz. Towards the end of the chamber, the motion is smoothed and the frequency reduces to near 90 Hz. As for lean flames, the Fourier spectra plotted at $t_1 = 0.15$ s, $t_2 = 0.3$ s and $t_3 = 0.45$ s in Fig. 2.9 show the peak amplitudes of the flame oscillation and of the sound level at the same frequency. It is important to note that the

tips at the mid-position of the flame cells will form the long funnels in the next period. This curious behaviour results in a period doubling only at these particular points (mid-points of the cells and funnels). Nevertheless, the average frequency of the motion matches still that of the pressure waves, as stated by Markstein [5] and Searby [6].

2.2.2 Methane flames

We study here the behaviour methane flames, an example of low-carbon fuels. Contrary to conventional propane flames, the secondary acoustic instability is observed in lean methane flames ($\phi < \phi_c \approx 0.95 \pm 0.05$), as can be checked in Fig. 2.10. Lean (rich) methane flames exhibited flame oscillations of similar characteristics to those described before for rich (lean) propane flames.

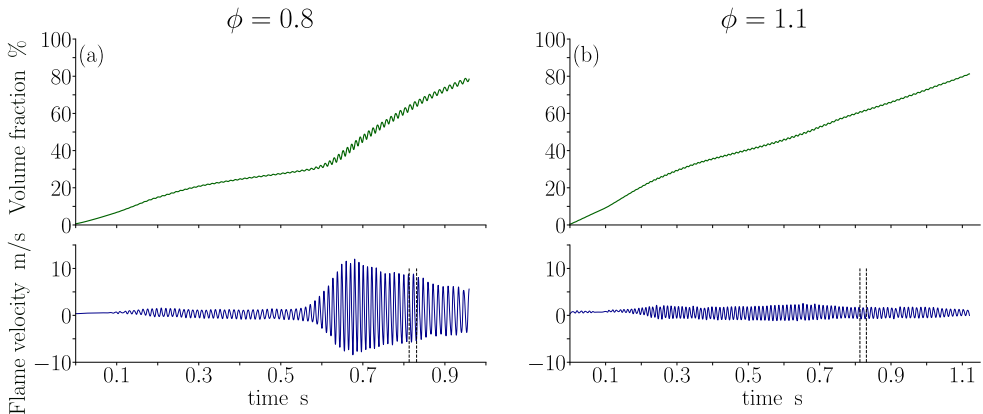


FIGURE 2.10 | Time evolution of the burned volume fraction V_b/V_{tot} (upper thick-solid line) and flame velocity $U_L = (Wh)^{-1}dV_b/dt$ (lower thin-solid lines) for a lean ($\phi = 0.8$) (a) and a rich ($\phi = 1.1$) (b) methane-air flame. The maximum uncertainty of the burned volume measurements is $\pm 2.75\%$. The dotted vertical lines represent the period of oscillation covered by the sequence of images displayed in Fig. 2.11.

The evolution of both the burned volume fraction and the flame velocity with time is shown in Fig. 2.10 (a) and 2.10 (b) for lean and rich flames respectively. The oscillation frequency varies with the equivalence ratio and also changes during the propagation of the flame for all the studied cases, although it always remains around 100 Hz. Also, the frequency analysis of the sound generated during the propagation shows a matching with the flame-position oscillation similar to that of propane, but was not included here to avoid repetition.

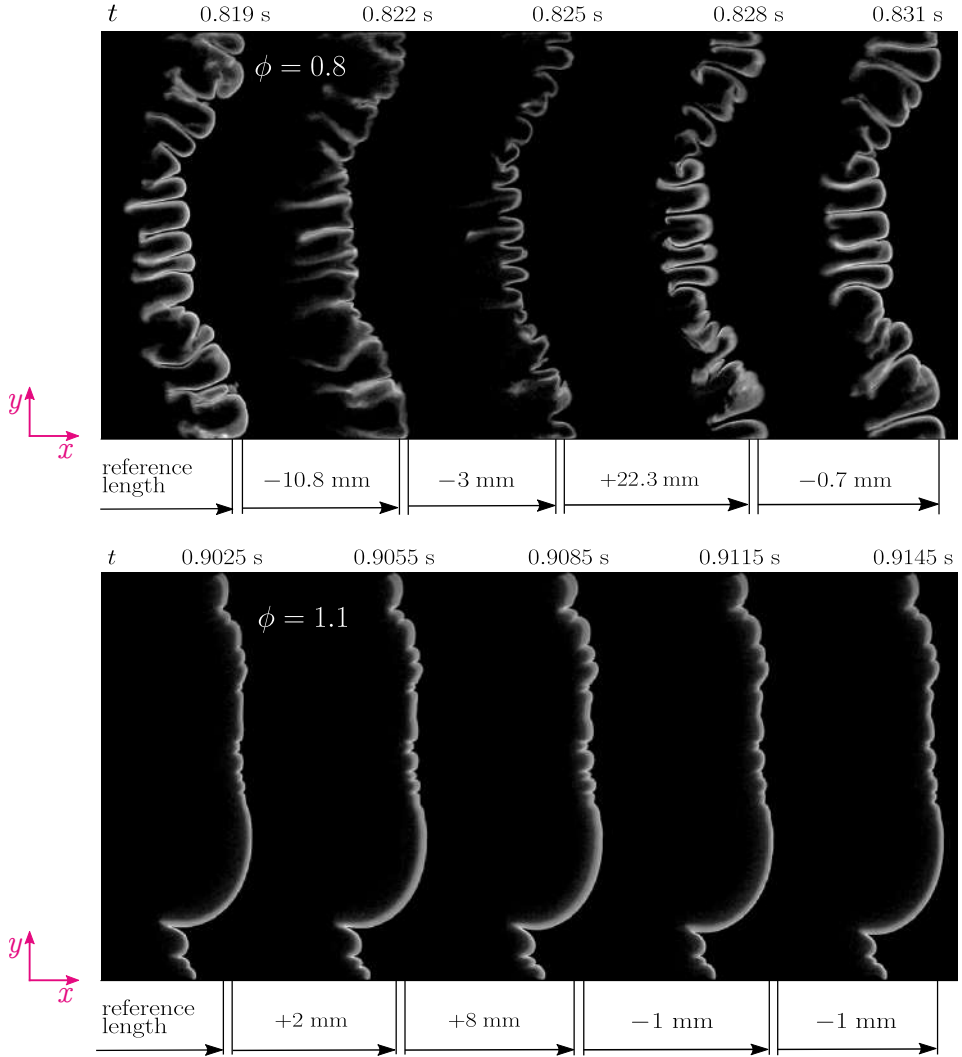


FIGURE 2.11 | Top view of methane flames during the oscillation cycle indicated by the vertical dashed lines included in Fig. 2.10. The leftmost image of the sequence was taken at $t = 0.819$ s for $\phi = 0.8$ and at $t = 0.9025$ s for $\phi = 1.1$ with the frames separated $\Delta t = 0.003$ s. At the bottom of the figure we include the relative distance traveled by the flame between two consecutive frames. The error in the determination of the equivalence ratio is ± 0.05 and the maximum uncertainty of the burned volume measurements is $\pm 2.75\%$.

In Fig. 2.11 we composed a sequence of images that tracks a lean methane flame ($\phi = 0.8$) during an oscillation cycle in which the flame travels from $x \approx 0.47$ m to $x \approx 0.48$ m, with

the leftmost picture taken 0.819 s after ignition and with the photographs shown every 0.003 s. To give an idea of the distance covered by the flame during one oscillation cycle, we included the relative distance traveled by the flame between two consecutive frames measured at one half of the chamber height $y = W/2$. At the beginning of the oscillation cycle, the flame moves backwards a total distance of -13.8 mm at 2.3 m/s. At half of the cycle, the flame swaps the propagation direction to travel forward 22.3 mm with a peak velocity of 7.4 m/s. During the last fourth of the cycle, the flame slowly recedes -0.7 mm at 0.23 m/s. The average displacement velocity during this cycle is 0.65 m/s, larger than the flame velocity of a planar flame $S_L = 0.24$ m/s.

When working with methane, the transition from the primary to the secondary instability takes place at an equivalence ratio close to unity. As shown in Fig. 2.11 for a rich methane-air flame ($\phi = 1.1$), only small-amplitude oscillations, representative of the primary instabilities, are detected. The net displacement along the selected cycle is 8 mm, slightly shorter than the distance traveled by the lean flame ($\phi = 0.8$) under the secondary regime, and the average velocity at this stage of propagation is 0.67 m/s. Also, the shape of the front only presents minor changes when experiencing these small-amplitude oscillations, as shown in Fig. 2.11.

2.2.3 Dimethylether (DME) flames

For alternative gaseous ether bio-fuels, such as DME, thermoacoustics seem to behave in a similar way as for propane $Le > 1$, being the secondary instability only observed for equivalence ratios above a critical value that turns out to be approximately $\phi_c \approx 0.55 \pm 0.05$. As illustrated in Fig. 2.12, the evolution of the burned volume fraction and of the flame velocity with time for $\phi = 0.5 < \phi_c$ and $\phi = 0.6 > \phi_c$ shows the previously-observed characteristics of propane and methane flames oscillating in the primary and secondary acoustic instability regimes, respectively. Note that the vertical scales of the flame velocity were modified for clarity. It is only in the case $\phi = 0.6 > \phi_c$ when the finger-shaped, large-amplitude flame oscillations are observed, with maximum and minimum oscillation velocities near 13 and -7 m/s respectively.

To achieve the combustion of flames as lean as $\phi = 0.5$ we did not preheat the gas nor the cell walls, and the experimental procedure was identical to that described above in section 2.1. Such lean flames showed considerably longer propagation times, of around 2 s, and the post processing of the images was much harder and noisier due to the low emissivity of these flames.

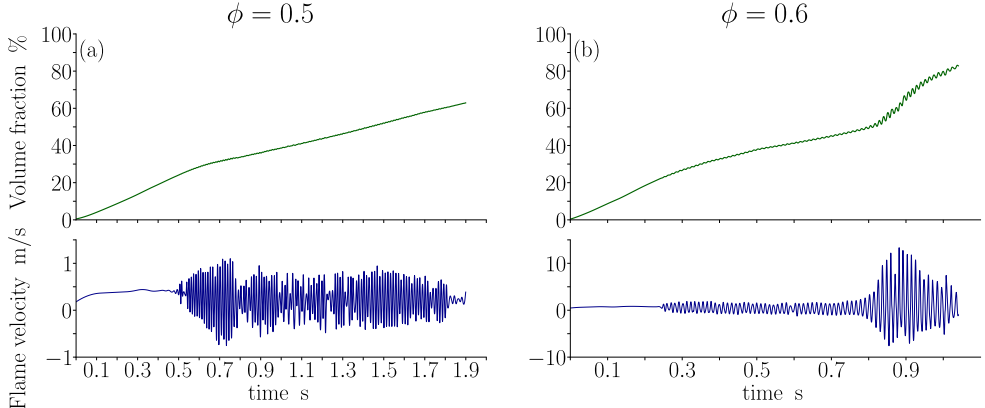


FIGURE 2.12 | Time evolution of the burned volume fraction V_b/V_{tot} (upper thick-solid line) and the flame velocity $U_L = (Wh)^{-1} dV_b/dt$ (lower thin-solid lines) for an equivalence ratio $\phi = 0.5 < \phi_c$ (a) and $\phi = 0.6 > \phi_c$ (b) of a DME-air flame. The maximum uncertainty of the burned volume fraction measurements is $\pm 2.75\%$. The range of the vertical axes is different for the flame velocity plots.

2.3 Effect of the combustion chamber thickness h

Petchenko et al. [19, 20] performed a numerical study of a flame propagating towards the close end of a 2-D channel. They reported the violent folding of the flame due to flame-acoustic resonance. According to the authors, as the ratio $a = h/\delta_T$ was reduced, the amplitude of the flame oscillation decreased but never disappeared. To test their results, we modified the chamber thickness by stacking 3 mm-thick PVC laminae to progressively reduce the gap between the horizontal plates from $h = 10$ mm to $h = 1$ mm. The evolution of the burned volume fraction and the flame velocity with time for $h = 10, 7, 4$ and 1 mm are plotted in Fig. 2.13 for DME with $\phi = 1$.

In the widest chamber ($h = 10$ mm) the flame front presents high-amplitude oscillations similar to those shown before for propane, methane and DME. The flame travels along the chamber with a flame speed that oscillates between a maximum of 8 m/s and a minimum of -5 m/s approximately. The high-amplitude oscillations were not observed when the chamber thickness was reduced to $h = 7$ mm. Both the burned volume fraction and the flame velocity display small oscillations that are characteristic of the primary acoustic instability regime. Farther reduction of the chamber height ($h = 4$ mm and $h = 1$ mm) completely eliminates the flame oscillations and the flame propagates with a non-oscillatory velocity along the chamber.

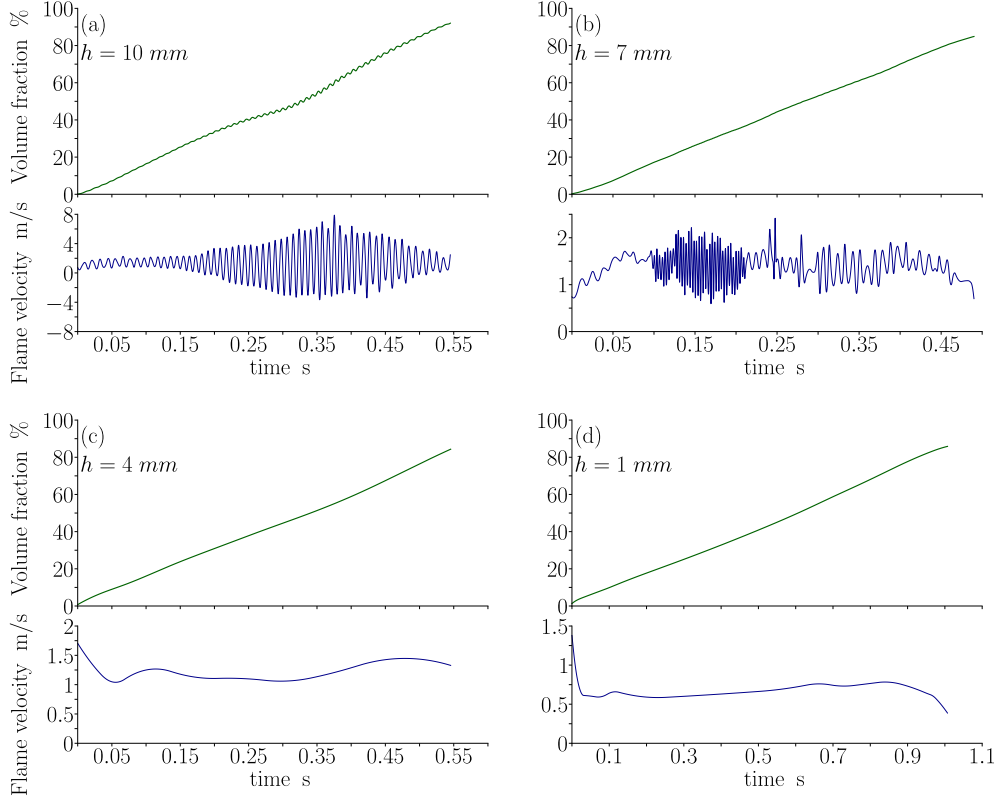


FIGURE 2.13 | Burned volume fraction and flame velocity of a DME flame with $\phi = 1$ in a channel of thickness (a) $h = 10 \text{ mm}$ (b) $h = 7 \text{ mm}$, (c) $h = 4 \text{ mm}$ and (d) $h = 1 \text{ mm}$. The range of the axes is different in each plot.

The transition to the secondary instability is also observed in narrower channels in our experiments when richer DME-air mixtures were used. For example, for $h = 7 \text{ mm}$ and $h = 4 \text{ mm}$, high-amplitude oscillations are only observed for $\phi > \phi_c = 1.175 \pm 0.05$ and $\phi > \phi_c = 1.325 \pm 0.05$, respectively.

According to the numerical studies by Petchenko et al. [19, 20], the large-amplitude oscillations and flame folding would disappear for $a = h/\delta_T < 25$. In our experiments, they were not observed for $a < 200$. The small-amplitude oscillations, characteristic of the primary acoustic instability, also ceased for $80 < a < 140$, a behaviour not reported in [20] but in agreement with the predictions by Kurdyumov and Matalon [21] in the limit $a \ll 1$. In light of

the experimental observations, it is worth analyzing the impact of the several losses that happen when propagating along narrow channels.

2.3.1 Heat losses

In this subsection, we perform an order-of-magnitude analysis comparing the characteristic values of the different heat-loss mechanisms that might affect the flame propagation under the prescribed conditions, an important point that was recurrently disregarded in previous studies. Papers of several authors [6, 9, 12–14] did not mention the influence of heat losses on their results, while Aldredge and Killingsworth [8] simply indicated that their effect was not important. In turn, Yoon et al. [7] only took acoustic losses into account.

Considering the worst case scenario, at which the inner faces of the horizontal plates are at the same room temperature as the unburned reactants (T_u), we can estimate the relative importance of the heat losses by comparing the conductive heat losses $q_k \sim W\delta_T k_g(T_b - T_u)/h$ from the flame to the horizontal plates per unit time through an area $W\delta_T$, and the heat released by the flame per unit time $q_f \sim \rho S_L QY_F hW$, yielding

$$\frac{q_k}{q_f} \sim \left(\frac{\delta_T}{h} \right)^2, \quad (2.3)$$

where $QY_u = c_p(T_b - T_u)$ is the heat release per unit of fuel mass consumed, Y_F the fuel mass fraction of the unburned gas and c_p and k_g are the air specific heat and the thermal conductivity, respectively. Using the data summarized in Table 2.1 to provide the characteristic values for stoichiometric propane-air flames ($\delta_T = 0.05$ mm, $h = 10$ mm), we obtain typical values of $q_k/q_f \sim 25 \times 10^{-6} \ll 1$, which confirm the small influence of the heat losses in the widest-channel experiments. As the channel height h was progressively reduced by setting the horizontal plates closer to each other, the effect of the heat losses would become more important, leading to flame extinction for values of $\delta_T/h \sim O(1)$.

The heat lost by conduction to the channel's walls, even when small compared to the heat released by the flame, might be conducted longitudinally along the solid wall upstream of the flame and transferred back to the gas, preheating the mixture before the arrival of the reaction front. The time for this to occur in a distance δ_T upstream of the traveling flame

along the solid wall is $t_{k,w} \sim \delta_T^2/D_{T,w}$, where $D_{T,w}$ is the thermal diffusivity of the solid wall. When compared with the residence time of the flame $t_r \sim \delta_T/S_L$, it is possible to neglect the preheating of the gas close to the solid surfaces as long as the ratio $t_{k,w}/t_r \sim D_T/D_{T,w} \gg 1$. In the case of the glass ($D_{T,w} = 3.4 \times 10^{-7} \text{ m}^2/\text{s}$) and the vinyl sheet ($D_{T,w} = 5 \times 10^{-8} \text{ m}^2/\text{s}$) that form both the upper and lower horizontal plates of our experimental setup, the criterion $t_{k,w}/t_r \gg 1$ is satisfied. In experiments that use quartz ($D_{T,w} = 1.4 \times 10^{-6} \text{ m}^2/\text{s}$) or metal covers ($D_{T,w} \sim 10^{-4} \text{ m}^2/\text{s}$), one should be cautious to properly assess the influence of this effect on their results.

Most of the heat losses take place in the burned region from the high temperature gas to the walls. Its potential importance on the flame propagation can be estimated by calculating the characteristic temperature gradient downstream of the flame. By considering the heat losses to the walls $k_g(T_b - T_u)/h$ in a reference system attached to the flame, we can estimate the temperature change in a portion of the channel of length l by doing an energy balance in a control volume of height h with the sides against the upper and lower walls to give $(T_b - T_l)/(T_b - T_u) \sim (\delta_T/h)(l/h)$, being T_l the gas temperature at a distance l downstream of the flame and T_u the solid wall temperature. For the flame to be affected by the negative temperature gradient downstream of the flame, the temperature change in a region $l \sim \delta_T$ should be of the order $(T_b - T_l)/(T_b - T_u) \sim (\delta_T/h)^2 \sim \beta^{-1}$ [37], where β is the Zeldovich number. Using the data included in Table 2.1, we obtain $(\delta_T/h)^2 \ll \beta^{-1}$ in most of the cases tested in our experiments. It is only in very narrow channels $h = 1 \text{ mm}$ when the negative temperature gradient $(\delta_T/h)^2 \sim \beta^{-1}$ seems to affect the propagation of the flame, as shown in Fig. 2.13 for a stoichiometric DME flame. Note that the large values of β would make this effect more restrictive than the direct heat losses of the flame to the walls analyzed above to write Eq. 2.3.

As expected by the estimations given above, the smaller the chamber thickness the longer it takes to the flame to reach the end of the chamber due to the effect of the heat losses as the volume-to-surface ratio is increased. Using Fig. 2.13 to obtain the average propagation velocity, we can conclude that flames propagating in chambers with $h = 10, 7$ and 4 mm , with approximately the same propagation time, are weakly affected by the heat losses. It is only in the case $h = 1 \text{ mm}$ when the deceleration of the flame becomes noticeable, presumably because of the heat losses. Such small effect of h in the flame velocity seems to indicate that heat losses

could be considered negligible except in very narrow channels. These estimations have been examined numerically by Kurdyumov and Fernández-Tarrazo [38], Daou and Matalon [39] and Sánchez-Sanz [40] confirming the small influence of heat losses for sufficiently wide channels.

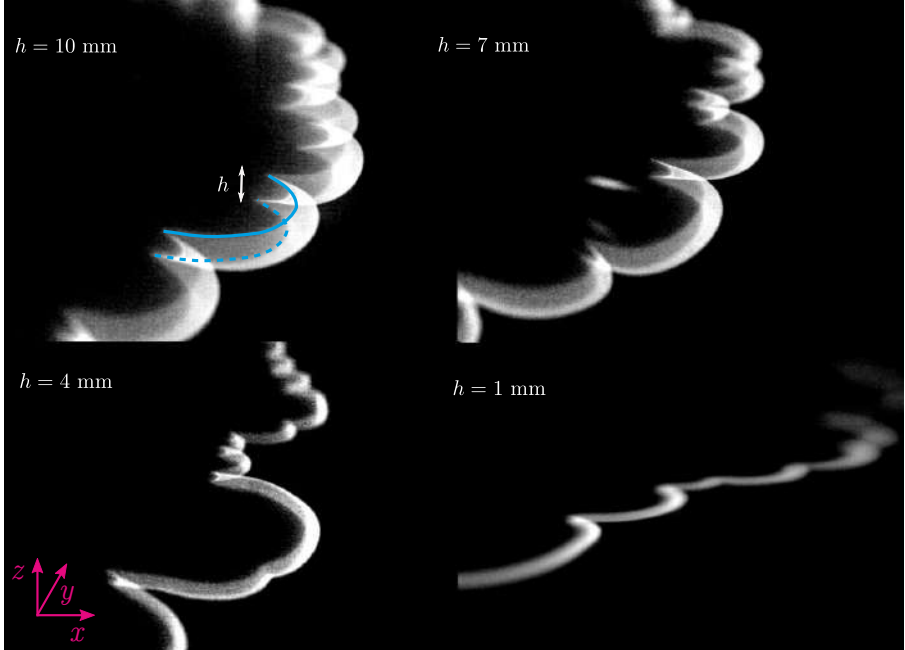


FIGURE 2.14 | Lateral view of a stoichiometric DME flame propagating in a $h = 10$ mm, $h = 7$ mm, $h = 4$ mm and $h = 1$ mm cell. The solid and dashed cyan lines indicate where the flame touches the upper and lower horizontal plates, respectively.

Previous numerical studies [21, 22, 41] reduced the computational cost of their computations by reducing the number of dimensions of the problem by assuming that, in the limit of very narrow channels $a = h/\delta_T \ll 1$, the transverse profiles (z axis) of temperature and mass fraction are uniform. To check this point, we studied the effect of the channel gap on the flame shape in Fig. 2.14. In this figure we included the lateral view taken at $x \sim 150$ mm of a stoichiometric DME flame propagating in a chamber with $h = 10, 7, 4$ and 1 mm. Here we can observe how the reaction region keeps its parabolic shape even in very narrow channels $h = 1$ mm in which the parameter $a \sim 20$. Much narrower channels seem to be necessary to reach uniform transverse profiles of temperature and mass fraction.

2.3.2 Viscous layer

To understand the effect of the channel height on the flame oscillations, it is interesting to estimate the order of magnitude of the acoustic energy and viscous dissipation. When an harmonic sound wave, with angular frequency ω , propagates along a channel, an acoustic boundary layer of thickness $\delta_v \sim (2\nu/\omega)^{1/2}$, being ν the kinematic viscosity, appears near to the channel walls to accommodate the fluid particle oscillation amplitude from its value in the mainstream to zero on the wall's surface. At a sound frequency of around 100 Hz measured in our experiments, the acoustic boundary layer is of order $\delta_v \sim 0.2$ mm in the cold gas ($T_u = 298$ K, $\nu = 15.06 \times 10^{-6}$ m²/s) and grows to be as thick as $\delta_v \sim 1.12$ mm in the burned gas ($T_b = 2000$ K, $\nu = 39.43 \times 10^{-5}$ m²/s). Such a thick acoustic boundary layer brings associated a strong dispersion of acoustic energy that can be estimated easily by comparing the residence time of a sound wave $t_s \sim 2L/c$, with $c \approx 695$ m/s representing the sound velocity at a characteristic temperature $T \sim (T_b + T_u)/2 \sim 1000$ K, and the acoustic dissipation time $t_{s,d} \sim \rho h^2/\mu$, calculated by comparing the energy of the acoustic sound wave per unit volume ρw^2 , and the viscous dissipation rate $\mu(w^2/h^2)$, with w being the velocity induced by the acoustic pressure wave. Comparing both characteristic times we obtain

$$\frac{t_s}{t_{s,d}} \sim \frac{2\nu L}{ch^2} \sim \begin{cases} 0.005 & \text{for } h = 10 \text{ mm.} \\ 0.497 & \text{for } h = 1 \text{ mm.} \end{cases} \quad (2.4)$$

Therefore, for $h = 10$ mm, the acoustic time is much shorter than the acoustic dissipation time, what indicates that the pressure wave has time enough to interact with the flame before its attenuation. Contrarily, in smaller chamber gaps, the dissipation time is of the order of the acoustic time, limiting the effect of the acoustic wave on the flame. The parametric dependence of the ratio $t_s/t_{s,d}$ coincides with the dissipation rate due to viscosity $(\nu L/ch^2)^{1/2}$ of a pressure wave traveling along a channel of height h calculated by Blackstock [42] and by Clanet et al. [17]. Note that the characteristic time for the radiative damping through the open end $t_{rad} \sim cL/(\omega h)^2$ [17] is much longer than t_d and can therefore be neglected.

2.4 Effect of buoyancy

We introduce in this section the complex dynamics of premixed flames when they are under the effect of buoyancy. We show how gravity has a non negligible effect neither on the propagation of the flames nor on thermoacoustics. Its influence is generally evaluated by the Froude number $\text{Fr}^2 = S_L^2 / gh$, which compares inertial to gravity effects (Table 2.2). The impact of the buoyancy-driven Rayleigh-Taylor instability [43] on the flame-acoustic coupling for the combustion of the aforementioned mixtures is evaluated by rotating the combustion chamber ($\alpha = \pm 90^\circ$) and therefore the flames propagate vertically (both up- and downwards). The channel gap size is kept constant, $h = 10$ mm, and we just varied the equivalence ratio and the fuel to modify the speed and thermal thickness of the flames. Given a constant acceleration of gravity g , the dynamics of slow and thick (lean or rich enough) flames are modified by the increasing importance of buoyant hot products.

TABLE 2.2 | Squared Froude number for the tested hydrocarbon and ether gaseous flames calculated at ambient temperature and pressure. The shadowed compositions are only ignited for upward-propagating tests.

$\text{Fr}^2 \times 10^{-3}$			
	Methane	Propane	DME
0.5	-	-	51
0.6	92	229	246
0.7	242	491	587
0.8	593	852	1114
ϕ	1077	1249	1600
1	1402	1543	1977
1.1	1249	1672	2154
1.2	1056	1520	2076
1.3	612	1395	1973
1.4	157	743	1714

We want to remark that the velocity U_L and pressure signals are not displayed in this section because they have the same shape as those shown before (*e.g.*, Fig. 2.4). For the sake of conciseness and to avoid repetition, only the overall flame shape, some interesting details and the maximum acoustic pressure recorded by the sensor within the chamber are given to describe the propagation of these buoyant flames.

2.4.1 Downward-propagating flames

When the acceleration of gravity acts in the same direction than that of propagation, which happens for downward-propagating flames, long wavelengths that may appear at the front are found to be stable under a linear stability analysis [44]. We show here how this stabilizing effect influences the onset of thermoacoustics and the overall dynamics of premixed flames.

Before picturing the results, it is interesting to give a brief remark on how buoyancy affects all the studied flames at regions close to the ignition heat source. Figure 2.15 shows the first time steps of a downward-propagating lean DME ($\phi = 0.7$) flame. Just after ignition ($t = 14$ ms), both the hot reaction products and the extra heat liberated by the glow plug created a candle-like structure due to the gravity-induced velocity U_g at the region, showing an elongated tail appointing upwards in the flame front. To estimate U_g , consider that the glow plug is at a maximum temperature $T_{\text{plug}} = 1600$ K [45] and that the local burned products at its surroundings are at a similar temperature, much higher than the gas far from the ignition source. Applying the said conditions, the Rayleigh number $Ra = g\kappa(T_{\text{plug}} - T_u)h^3/(\nu D_T) \sim 500$, being $\kappa = 1/T$ the inverse of the preheat temperature for ideal gases and considering the thermal diffusivity ($D_T = 2 \times 10^{-4}$ m²/s) and kinematic viscosity ($\nu = 1.5 \times 10^{-4}$ m²/s) of air at the mean temperature $T = (T_{\text{plug}} + T_u)/2$, is much higher than one and so the effect of viscosity can be neglected when compared to free convection. From the balance between convective and buoyancy terms in the momentum conservation equation (Eq. 5.9), the hot-gas buoyant velocity is given by $U_g \sim \sqrt{(1 - \rho_{\text{plug}}/\rho_u)gh} = \sqrt{(1 - T_u/T_{\text{plug}})gh} \sim 0.28$ m/s, similar to the laminar burning velocity $S_L = 0.25$ m/s and fast enough to pull-up the curved front propagating at a velocity U_L .

Later ($t = 62$ ms), the flame front keeps propagating downwards but the gas near the still-on glow plug is strongly affected by buoyancy, stretching the flame and, eventually –not in the particular case shown in Fig. 2.15–, inducing a local quenching ($t = 195$ ms) that splits the flame front. Despite the latter, the flame usually recovers a continuous front sufficiently far downstream from the heat source. Although being considerably small, its effect on the initial conditions of the problem cannot be neglected in the development of the front dynamics, becoming more intense at lower Froude numbers.

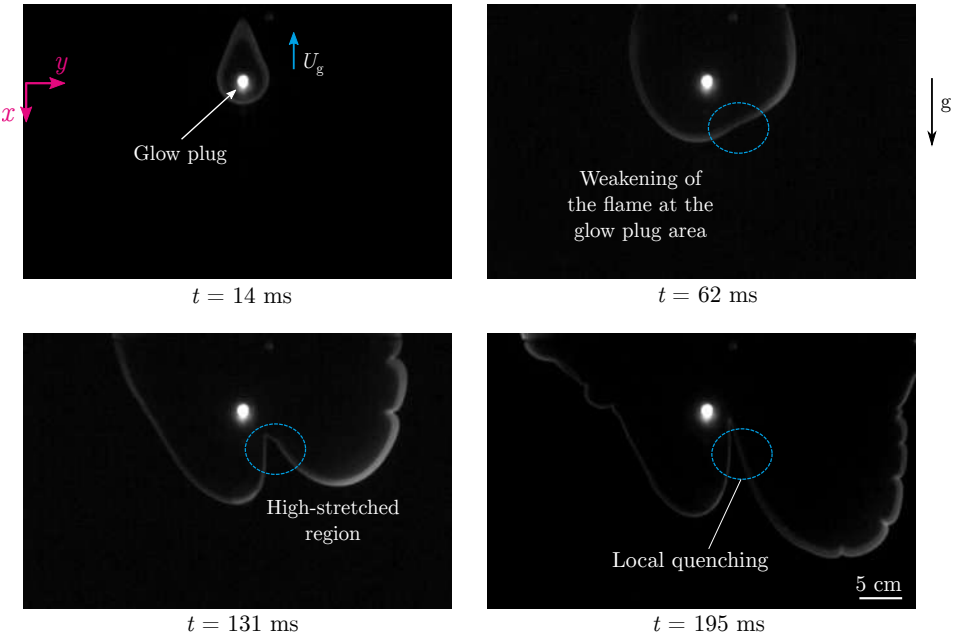


FIGURE 2.15 | Influence of the ascendant buoyant flow generated by the ignition system to a $\phi = 0.7$ DME flame.

Propane and DME flames ($Le > 1$)

Propane and DME flames behave –qualitatively– in the same manner (section 2.2; [46]). To avoid repetition, both are studied together despite the potential quantitative differences that might exist, such as the transition point to the secondary thermoacoustic regime or the maximum acoustic pressure within the combustion chamber. Figure 2.16 shows two pictures of (a) a propane and (b) a DME flame under the primary and the secondary regimes respectively, that propagate from the top to the bottom of the combustion chamber. The fuels could be swapped –always considering flames under the same thermoacoustic regime– without introducing major discrepancies.

There are not huge differences if one compares horizontal cases [46] to downward-propagating flames. As before, the lean-enough flame propagates undergoing a smooth oscillation with maximum acoustic pressures around 300 Pa (Fig. 2.17). Its dynamics are now partially influenced by the effect of buoyancy that appears for a sufficiently low Froude number ($Fr^2 < 1$), which corresponds to slow flames. Such a big hot and light gases region

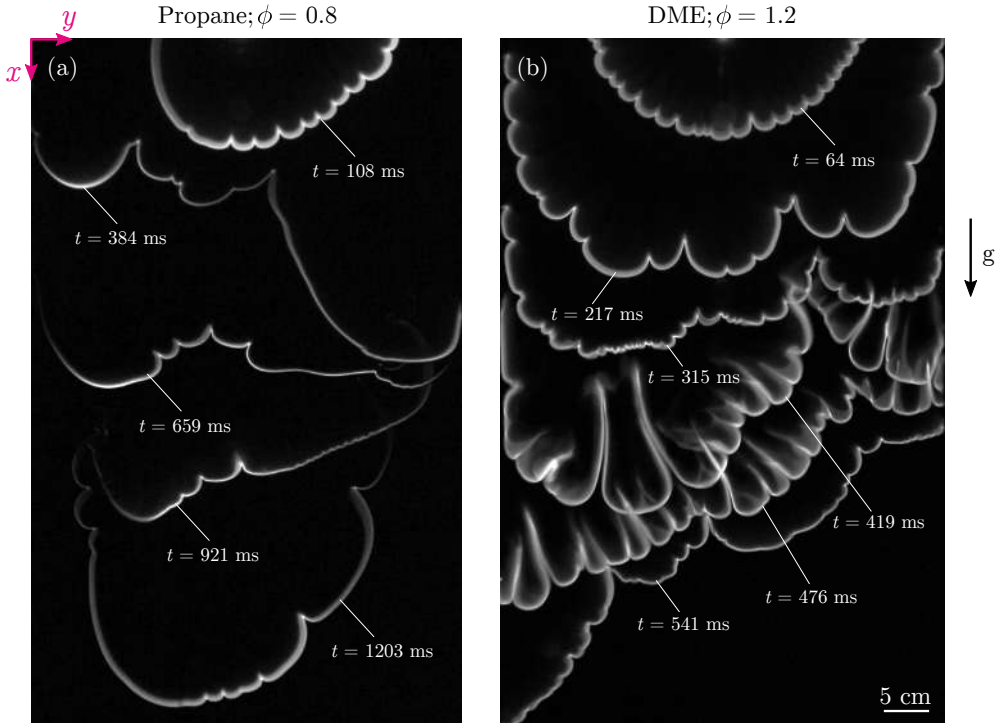


FIGURE 2.16 | Downward-propagating (a) $\phi = 0.8$ propane flame under the primary thermoacoustic regimes and (b) $\phi = 1.2$ DME flame suffering a strong influence of the secondary thermoacoustic instabilities. Both fuels are depicted together and could be swapped as they behave in the same way under the same thermoacoustic regime.

above the propagating front has a non-negligible effect on its shape and behaviour. One of the most important features being the existence of local quenching near the lateral frame from buoyancy-induced stretch similar to that introduced close to the glow plug. It permits the exit of the acoustic waves without interacting with the flame at some parts of the domain, reducing the flame-wave interaction (*i.e.*, lower acoustic pressure). Furthermore, the velocity field is modified both local and globally when the flame is broken, creating a somehow chaotic behaviour of the flames that promote the propagation at certain areas. In the case shown in Fig. 2.16 (a), the flame at $t = 384 \text{ ms}$ moves preferentially close to the right wall. Later, the same flame suffers partial quenching near the lateral walls and the front is never able to reach them again.

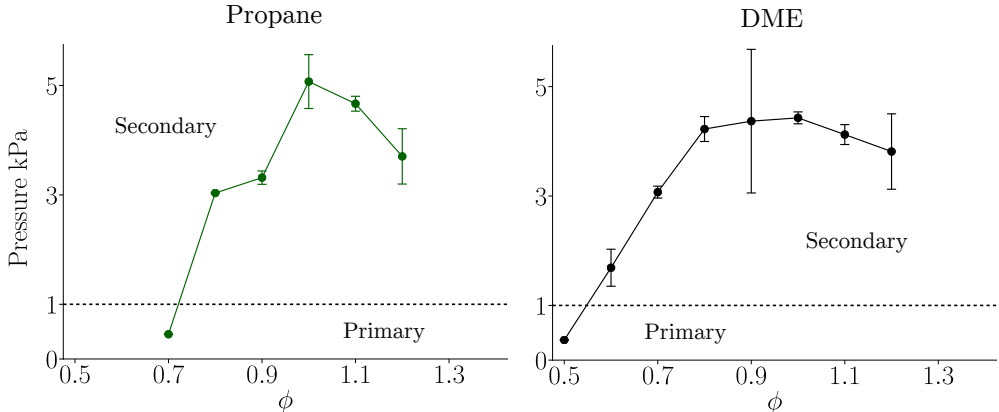


FIGURE 2.17 | Maximum acoustic pressure obtained for downward-propagating propane and DME flames ($Le > 1$).

Faster flames ($Fr^2 > 1$) are not so influenced by the buoyant flow generated by the hot reaction products. Richer mixtures than a critical value ($\phi_c \sim 0.80 \pm 0.05$ for propane and $\phi_c \sim 0.50 \pm 0.05$ for DME given our particular conditions), suffer strong oscillations ($p_{max} \sim 4000$ Pa, Fig. 2.17) as they are in the secondary thermoacoustic regime. The flame shape is completely dominated by acoustics (Fig. 2.16 (b)) and the only remaining effect of buoyancy is a slightly planar front at, for example, $t = 476$ ms. As stated in [44], gravity stabilizes the long wavelengths of the front, making it more planar than non-buoyant flames.

Methane flames ($Le \approx 1$)

Methane flames require particular treatment as they behave exactly in the opposite way than fuels with $Le > 1$. As for horizontal flames [46], Fig. 2.18 shows how a lean methane flame undergoes a wild vibratory propagation ($p_{max} \sim 3000$ Pa for $\phi = 0.7$, Fig. 2.19) and totally modifies the front shape displaying the characteristic finger-like lobes. Richer mixtures ($\phi > 1.1$) are not able to transit to the secondary regime and just propagate oscillating smoothly ($p_{max} < 1000$ Pa). Additionally, the effect of the buoyant products is again somehow noticeable. Some quenched regions can be found, for example, at $t = 2364$ ms.

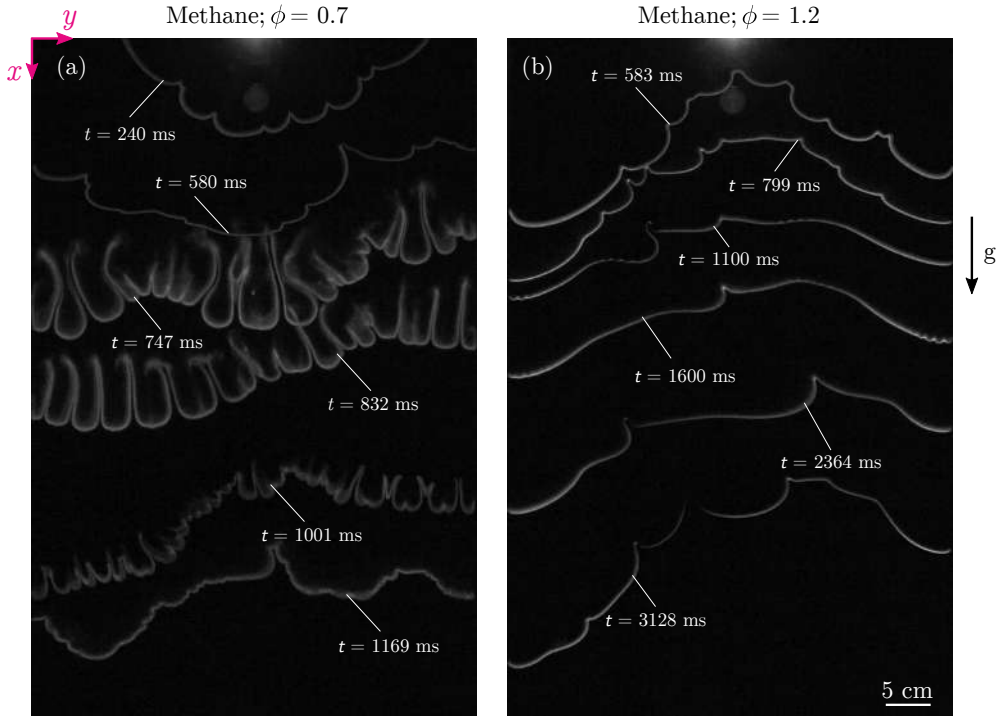


FIGURE 2.18 | (a) Lean $\phi = 0.7$ downward-propagating methane flame at the secondary thermoacoustic regime. (b) Rich $\phi = 1.2$ methane flame undergoing a smooth vibration in the primary thermoacoustic regime.

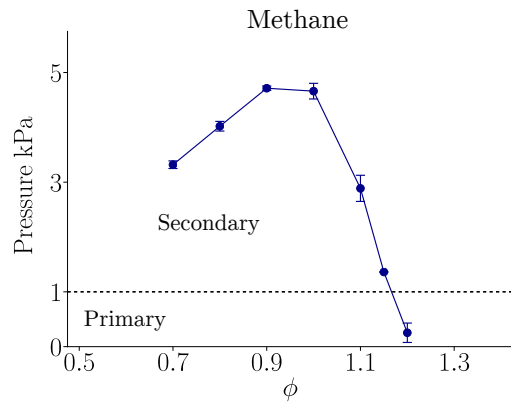


FIGURE 2.19 | Maximum acoustic pressures recorded for several methane flames with different equivalence ratios that propagate downwards.

To sum up, gaseous flames that propagate downwards behave in a similar way to non-buoyant ones [46]. The secondary thermoacoustic regime is found for rich-enough flames –mixture dependent– when we burn heavy fuels mixtures, such as propane and DME, and for sufficiently lean flames when the fuels are light (*e.g.*, methane).

2.4.2 Upward-propagating flames

We burn now vertical flames that propagate from the bottom towards the top of the combustion chamber and check if buoyancy-driven phenomena influence the dynamics of the propagation of the front. When traveling upwards, the hot products are located below the reaction front, widening both lean and rich flammability limits as a consequence of buoyancy. This feature allowed us testing slower flames that become totally influenced by gravity where the Rayleigh-Taylor instability dominates their dynamics. We show here how this phenomenon, among others, influence the appearance of thermoacoustic instabilities.

Besides this effect, related to the inherent nature of combustion, changing the orientation of the vessel introduces additional issues to the studied problem. One important feature related to the ignition system is recurrently found: we use a glow plug to trigger the chemical reactions that, depending on the burned fuel and its equivalence ratio, needs from 2 up to 8 s to ignite the mixtures. The maximum temperature reached by the heater is $T_{\text{plug}} = 1600$ K approximately one second after turning on the electrical system that feeds it [45]. Such a high temperature at the region heats up its surroundings, thus reducing the density of the non-ignited mixture and provoking an upward motion due to buoyancy at a determined velocity U_g (Fig. 2.20 (a)) that somehow modifies the initial conditions within the combustion chamber.

To estimate this velocity, we can consider that the preheated mixture is at $T_{\text{hot}} \sim 600$ K, which is lower than the auto-ignition temperature of all the tested mixtures. Neglecting viscosity again, the buoyancy induced velocity is calculated by $U_g \sim \sqrt{(1 - \rho_{\text{hot}}/\rho_u)gh} = \sqrt{(1 - T_u/T_{\text{hot}})gh} \sim 0.2$ m/s. Note that as T_{hot} can reach higher values the higher the auto-ignition temperature of the mixture, the induced velocity by this phenomenon also increases, being methane the most restrictive fuel. Furthermore, if the glow plug keeps heating for longer times the consequent effect is even worse. Therefore, the influence of this phenomenon cannot be neglected as U_g is found to be of the order of magnitude of the laminar burning velocity S_L of the mixtures studied here.

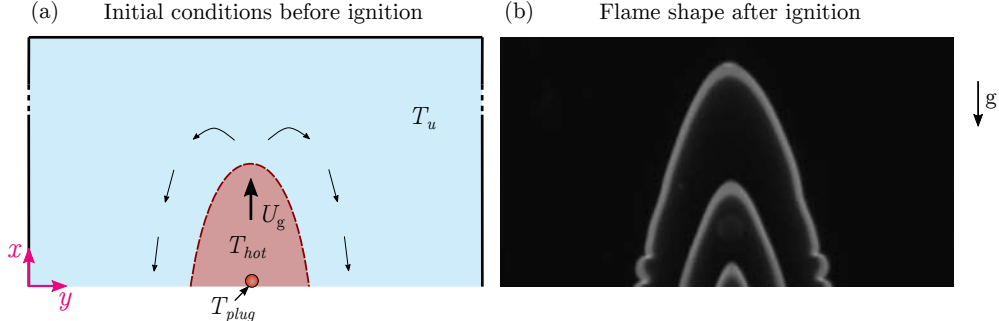


FIGURE 2.20 | (a) Conceptual sketch of the buoyancy-driven flow generated by the ignition system (glow plug). (b) Arrow-like flame shape short after ignition.

Also, while the hot light bubble ascends, it displaces the quiescent fresh mixture and creates a recirculatory velocity field at the combustion chamber that yields a modification of the initial conditions at the Hele-Shaw cell, which affect the dynamics of the flame once it begins its propagation. Figure 2.20 (b) shows the arrow-like flame that appears at short times after ignition. The central area affected by the aforementioned ascendant motion propagates faster, producing this characteristic form of the front. Furthermore, this effect adds to the also upward motion of the hot reaction products and accelerates the flames, mostly in regions close to the center of the vessel and the glow plug.

Additionally, the reaction products below the propagating front totally modify its outline. Linear perturbation analyses anticipate that if gravity acts in the opposite direction to that of flame propagation, it would destabilize the flame for all the possible wave numbers [18]. Therefore, one would expect smaller lobes in upward than in downward-propagating flames. However, the commented upward motion of light products due to buoyancy and the additional effect of the curvature of the flame tip, induce a transverse flow tangential to the reactive front that convects the small-wavelength perturbations away from the center towards the lateral channel walls [47]. Therefore, it stretches the flame and forces the smooth bubble-like reactive front observed in the propagating pictures (Fig. 2.23 and 2.25) despite of the overall destabilizing effect introduced by gravity.

Figure 2.21 gives a detail of the explained tangential convection at the early stages of a $\phi = 0.8$ propane flame. The cyan lines help following one of the generated lobes at the front for 70 ms, traveling around 15 cm in this gap of time. It is clear how this lobe moves downwards at

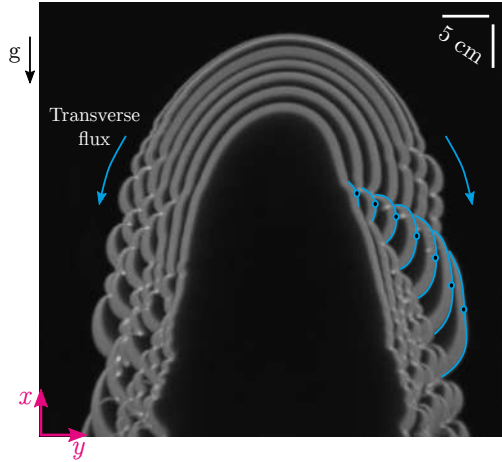


FIGURE 2.21 | Characteristic transverse flux ($U_{\text{vert}} = -2.2 \text{ m/s}$) of an upward-propagating $\phi = 0.8$ propane flame. The cyan arrows represent the vertical motion of the small-wavelength lobes towards the ignition end (bottom) of the chamber. The selected frames are taken with a time step of $\Delta t = 10 \text{ ms}$.

a high velocity ($U_{\text{vert}} = -2.2 \text{ m/s}$), being convected away from the center of the reactive front and making it smoother.

Propane and DME flames ($Le > 1$)

The aforementioned phenomena, which affect all the studied mixtures in this experimental setup, modify how the flames interact with the acoustic pressure waves present at the combustion chamber. We will first analyze heavy fuels, propane and DME blends, with a Lewis number larger than one.

Figure 2.22 shows the acoustic pressures obtained for different propane and DME mixtures, also comparing their values with flames of the same fuel propagating towards the opposite direction. Generally, both present the same behaviour when propagating upwards: flames of these fuels undergo very smooth primary acoustic oscillations when at lean conditions –even showing zero acoustic feedback close to the flammability limit of propane flames– and recover this behaviour for rich propane mixtures. In between these two primary thermoacoustic instability regions, the flames transit to the secondary acoustic regime and introduce a strong coupling with the pressure waves reaching up to 4 kPa, slightly lower than the pressure peaks found for flames that propagate downwards.

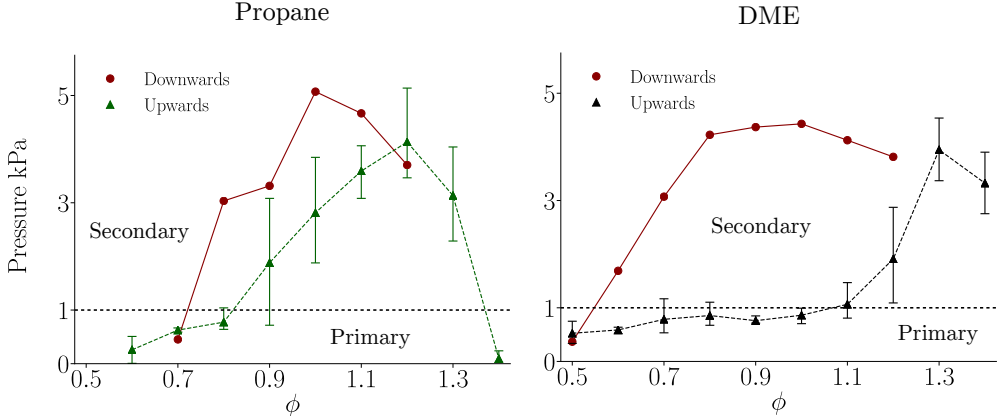


FIGURE 2.22 | Maximum acoustic pressures recorded for upward-propagating propane and DME flames with different equivalence ratio. The values obtained for flames that propagate to the opposite direction are added for comparison. The estimated error of the equivalence ratio is ± 0.05 .

Propane flames of an equivalence ratio $\phi < 0.85$ and $\phi > 1.35$ are depicted in Fig. 2.23 (a) and (e) respectively. At these conditions, the flames usually do not interact with acoustics at all and their dynamics and shape are mostly governed by the Rayleigh-Taylor instability, being the characteristic bubble shape clear for very lean and rich flames, as found also by Levy [48]. When considering very rich flames, it is also possible to observe the tip opening [18] at the cusps of the lobes that appear at the front during the propagation. Flames in between these two limits ($0.85 < \phi < 1.35$) suffer the secondary thermoacoustic instability. They also seem influenced by gravity –in a weaker manner– but are able to transit and vibrate strongly. Figure 2.23 (c) shows the characteristic shape of such a flame front, being very wrinkled once the strong vibrations begin and developing the well known finger-like lobes representative of the secondary thermoacoustic regime. Additionally, its overall outline ($\lambda \sim W$) keeps looking like a bubble, resembling flames that propagate with diverse boundary conditions as shown in Fig. 1.9, where they travel from a closed towards an open end (CO). When at these conditions, the pressure build-up at the ignition end pushes the flame forward and accelerates it. The combined effect of the buoyancy induced by the ignition system (Fig. 2.20) and the hot reaction products located below the front may promote a similar behaviour. For these reasons, the average velocities of all the flames are always higher when propagating upwards than downwards given the same mixture.

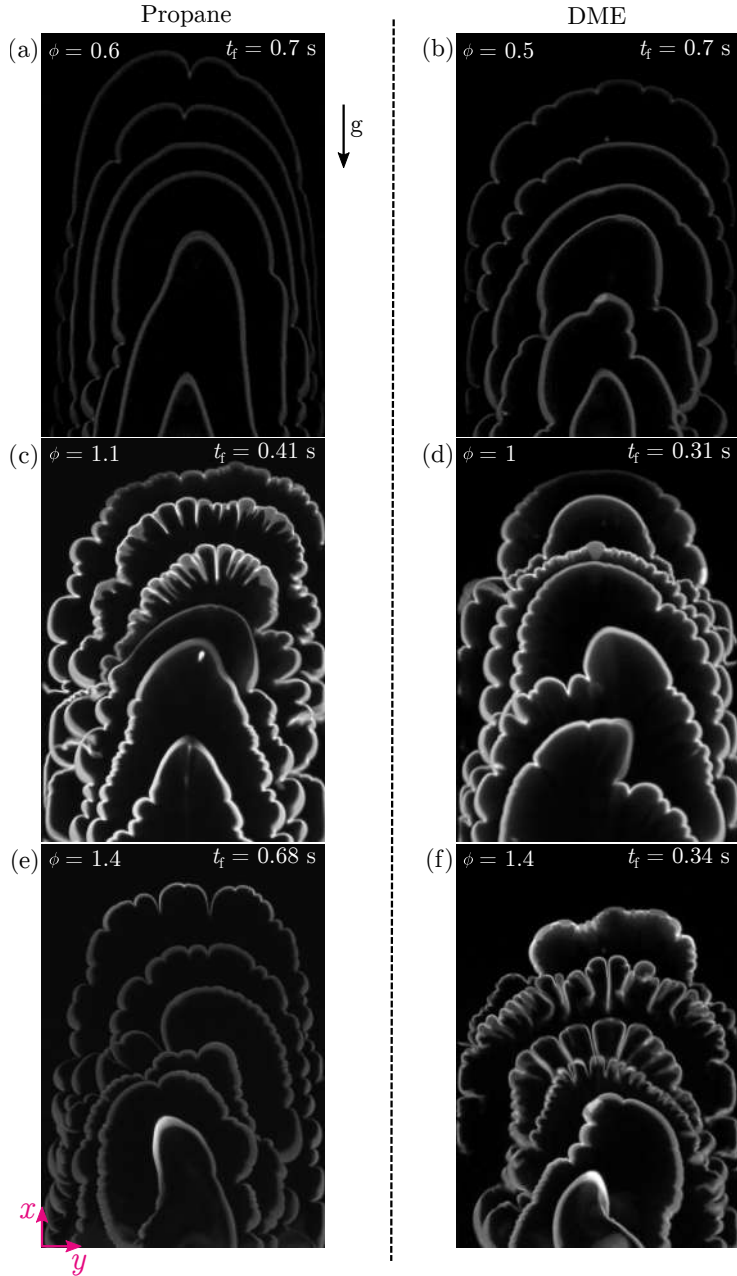


FIGURE 2.23 | Upward-propagating propane and DME flames characteristic of the different regions shown in Fig. 2.22.

When burning DME, the same general qualitative scene is found. Nevertheless, in all cases there is always acoustic coupling and flames only under the effect of the Rayleigh-Taylor instability are never reported in the range of equivalence ratio studied. For mixtures leaner than $\phi_c = 1.05$ approximately, the oscillatory flames propagate in the primary acoustic regime, reaching pressure amplitudes close to –but always below– 1 kPa, which is found to be the approximate threshold for the flames to fully transit to the secondary regime. A picture of the leanest of the flames studied ($\phi = 0.5$; $p_{max} \sim 500$ Pa) is shown in Fig. 2.23 (b). As for propane, the depicted front is also characterized by its overall bubble shape $\lambda \sim W$, but showing also some smaller wrinkles ($\lambda < W$) along its front, which may be related to the perennial coupling with acoustics. Furthermore, Fig. 2.23 (d) shows a stoichiometric flame, undergoing oscillations driven by pressure waves close to the transition threshold. Richer flames than the critical value (Fig. 2.23 (f)) do reach the required pressure peak ($p_{max} \sim 4$ kPa $>$ 1 kPa) and travel under the secondary regime, revealing once again the characteristic thermoacoustic fingers along its bubble-like front.

Finally, we must remark two still-open questions related to upward-propagating DME flames. First, the descendent trend found for rich flames ($\phi = 1.3 - \phi = 1.4$) may anticipate the potential recovery of flames fully driven by the Rayleigh-Taylor for richer flames. However, such mixtures are out of our range of study and should be revisited in the future. Second, the transition for DME flames takes place at much richer compositions ($\phi = 1.05$) compared to downward-propagating flames ($\phi = 0.55$). A somehow anomalous behaviour not reported for propane mixtures. One possible response could be the much faster propagation speed when the flames propagate upwards, reducing the residence time of the flame and therefore the feedback with the acoustic waves present at the vessel. Nevertheless, there is still no clear answer to explain this particular performance.

Methane flames ($Le \simeq 1$)

Methane flames show a surprising behaviour when propagating upwards. The regions found for the tested methane mixtures are shown in the pressure- ϕ diagram of Fig. 2.24 and compared to those found when traveling downwards.

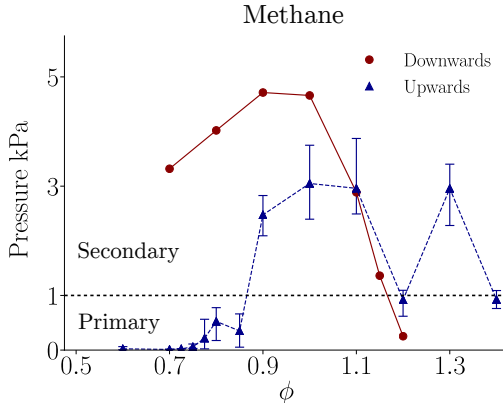


FIGURE 2.24 | Maximum acoustic pressures recorded for methane flames with different composition that propagate upwards. The values obtained for downward-propagating flames are included to compare both cases. The estimated error of the equivalence ratio is ± 0.05 .

First, there is a huge difference for lean blends. A $\phi = 0.7$ downward-propagating flame travels with strong vibrations which indicate a secondary thermoacoustic instability. On the contrary, when it propagates upwards, the feedback between the reactive front and the acoustic pressure waves almost disappears. To explain this difference, it is illustrative to compare lean flames ($\phi = 0.7$) that propagate downwards (Fig. 2.18 (a)) and upwards (Fig. 2.25 (a)). On the one hand, Fig. 2.18 (a) at $t = 240$ ms shows the downward-propagating front before being controlled by thermoacoustics (both primary and secondary). At this point, the front has already wrinkled due to the Darrieus-Landau instability, showing cells with wavelengths around $\lambda \sim 4$ cm. On the other hand, in upward-propagating flames Fig. 2.25 (a), gravity becomes relevant in slow flames ($Fr^2 < 1$). Shortly after ignition, they formed a smooth reactive front dominated by Rayleigh-Taylor instabilities with one lobe of a wavelength around $\lambda \sim 30$ cm, that never reaches the lateral walls of the chamber. Therefore, we can strengthen the hypothesis that, a wrinkled-enough flame seems more prone to interact with acoustics and to carry out the transition to the secondary regime.

When progressively increasing the amount of fuel in the mixture, the intensity of the pressure waves also does increase. For mixtures richer than $\phi = 0.8$ the primary acoustic instability is recorded, while for $\phi > 0.9$ and $\phi < 1.2$ the flames reach again strong acoustic pressure peaks, but always lower than those measured for downward-propagating fronts. The decrease on the maximum pressure can be related to the strong increment of the average propagation

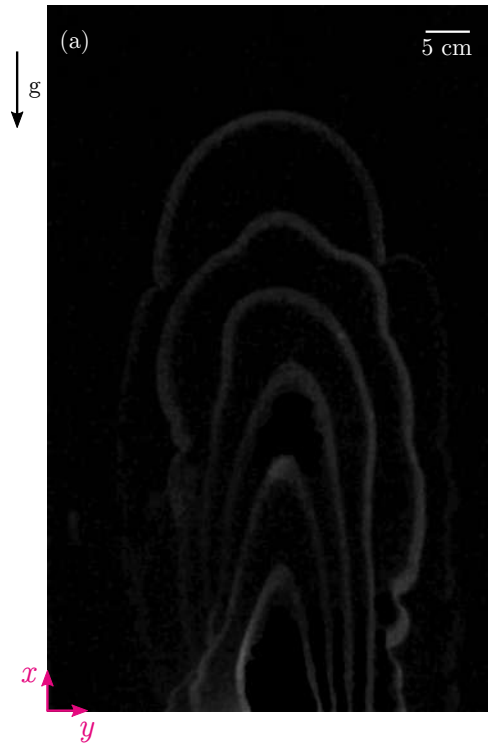
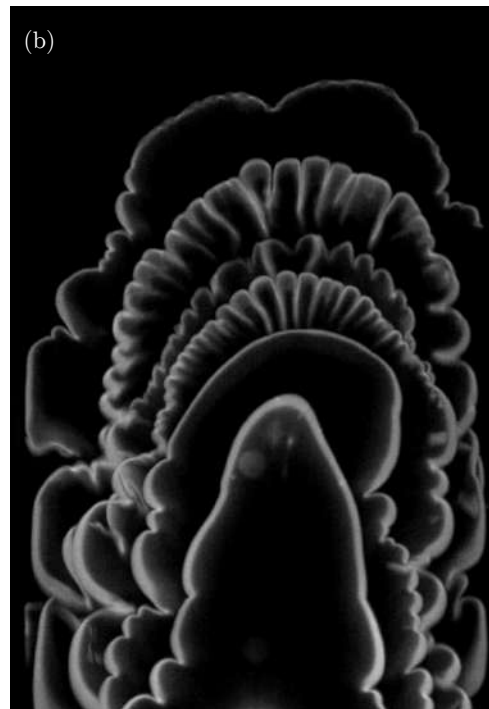
Methane; $\phi = 0.7$ Methane; $\phi = 1.1$ 

FIGURE 2.25 | (a) Lean methane flame that propagate upwards fully controlled by the Rayleigh-Taylor instability. The flame takes around $t_f = 0.7$ s to reach the top end. (b) Rich-enough upward-propagating methane flame undergoing violent vibrations at the secondary thermoacoustic regime. This flame requires of around $t_f = 0.45$ s to arrive to the opposite-to-ignition end.

speed, which reduces up to a 50% the total residence time of flames, thus decreasing the overall feedback effect. Furthermore, the flames are much less wrinkled in general, reinforcing the hypothesis that correlates flame wrinkling and thermoacoustics.

Finally, it is important to address the anomalous behaviour seen for methane flames richer than $\phi = 1.2$ shown in Fig. 2.24. We observe for this flames how there is a sudden decrease on the maximum pressure, recovering the primary acoustic regime as happened when propagating downwards. Once again the flame transits to the secondary regimes for slightly richer mixtures, finally recovering the smooth vibrations for $\phi = 1.4$ when gravity is strong enough ($Fr^2 < 1$). The abrupt recovery of the secondary acoustic oscillation around $\phi = 1.3$ can be related to the change in slope of the Markstein number for methane (Fig. 4.1 (b)), which modifies the

local response of the flame front to the curvature and strain produced by the acoustic pressure variations. Further insight on this matter is addressed in chapter 4.

References

- [1] E. Mallard, H. Le Chatelier, Sur les vitesses de propagation de l'inflammation dans les mélanges gazeux explosifs, *Comptes Rendus Hebdomadaires des Séances de l'Académie des Sciences* 93 (145–148) (1881).
- [2] R. Lord, The explanation of certain acoustical phenomena, *Roy. Inst. Proc.* 8 (536–542) (1878).
- [3] W. Mason, R. V. Wheeler, The propagation of flame in mixtures of methane and air. part i. horizontal propagation, *Journal of the Chemical Society, Transactions* 117 (36–47) (1920).
- [4] H. Coward, F. Hartwell, E. Georgeson, Studies in the mechanism of flame movement. part iv. the vibratory period, *Journal of the Chemical Society (Resumed)* (1482–1489) (1937).
- [5] G. H. Markstein, Instability phenomena in combustion waves, *Proceedings of the International Symposium on Combustion* 4 (44–59) (1953).
- [6] G. Searby, Acoustic instability in premixed flames, *Combustion Science and Technology* 81 (221–231) (1992).
- [7] S. H. Yoon, T. J. Noh, O. Fujita, Onset mechanism of primary acoustic instability in downward-propagating flames, *Combustion and Flame* 170 (1–11) (2016).
- [8] R. C. Aldredge, N. Killingsworth, Experimental evaluation of markstein-publisher influence on thermoacoustic instability, *Combustion and flame* 137 (178–197) (2004).
- [9] J. Yanez, M. Kuznetsov, J. Grune, Flame instability of lean hydrogen–air mixtures in a smooth open-ended vertical channel, *Combustion and Flame* 162 (2830–2839) (2015).
- [10] T. A. Connelly, D. C. Kyritsis, Experimental investigation of flame propagation in long, narrow, and open tubes, *Journal of Energy Engineering* 141 (C4014016) (2014).
- [11] J. Yang, F. Mossa, H. Huang, Q. Wang, R. Woolley, Y. Zhang, Oscillating flames in open tubes, *Proceedings of the Combustion Institute* 35 (2075–2082) (2015).
- [12] C. Almarcha, J. Quinard, B. Denet, E. Al-Sarraf, J. Laugier, E. Villermaux, Experimental two dimensional cellular flames, *Physics of Fluids* 27 (091110) (2015).

- [13] P. D. R. J. Gross, X. Pan, Flame propagation at low lewis publisher in narrow slots, Western States Section of the Combustion Institute (2014).
- [14] J. Sharif, M. Abid, P. Ronney, Premixed-gas flame propagation in hele-shaw cells, Spring Technical Meeting joint U.S.Sections,Combustion Iustitute, Washington D.C. (1999).
- [15] G. Searby, D. Rochwerger, A parametric acoustic instability in premixed flames, *Journal of Fluid Mechanics* 231 (529–543) (1991).
- [16] P. Clavin, P. Pelc , L. He, One-dimensional vibratory instability of planar flames propagating in tubes, *Journal of Fluid Mechanics* 216 (299–322) (1990).
- [17] C. Clanet, G. Searby, P. Clavin, Primary acoustic instability of flames propagating in tubes: cases of spray and premixed gas combustion, *Journal of Fluid Mechanics* 385 (157–197) (1999).
- [18] P. Clavin, G. Searby, Combustion waves and fronts in flows: flames, shocks, detonations, ablation fronts and explosion of stars (2016).
- [19] A. Petchenko, V. Bychkov, V. Akkerman, L.-E. Eriksson, Violent folding of a flame front in a flame-acoustic resonance, *Physical review letters* 97 (164501) (2006).
- [20] A. Petchenko, V. Bychkov, V. Akkerman, L.-E. Eriksson, Flame–sound interaction in tubes with nonslip walls, *Combustion and Flame* 149 (418–434) (2007).
- [21] V. N. Kurdyumov, M. Matalon, Effects of gas compressibility on the dynamics of premixed flames in long narrow adiabatic channels, *Combustion Theory and Modelling* 20 (1046–1067) (2016).
- [22] D. Fern  ndez-Galisteo, V. N. Kurdyumov, P. D. Ronney, Analysis of premixed flame propagation between two closely-spaced parallel plates, *Combustion and Flame* 190 (133–145) (2018).
- [23] G. Markstein, Project squid. the structure of flames burning in tubes. part 1. flame structure in slow-burning mixtures of hydrocarbons, air and nitrogen., Tech. rep., CORNELL AERONAUTICAL LAB INC BUFFALO NY (1950).

- [24] G. Markstein, Interaction of flow pulsations and flame propagation, *Journal of the Aeronautical Sciences* 18 (428–429) (1951).
- [25] G. Markstein, W. Squire, On the stability of a plane flame front in oscillating flow, *The Journal of Acoustical Society of America* 27 (416–424) (1955).
- [26] X. Wu, C. K. Law, Flame-acoustic resonance initiated by vortical disturbances, *Journal of fluid mechanics* 634 (321–357) (2009).
- [27] R. C. Assier, X. Wu, Linear and weakly nonlinear instability of a premixed curved flame under the influence of its spontaneous acoustic field, *Journal of Fluid Mechanics* 758 (180–220) (2014).
- [28] A. Lora-de-la Calle, Automatization of a flame propagation experimental setup using labview, *Trabajo fin de Grado* (2019).
- [29] D. Martinez-Ruiz, F. Veiga-Lopez, M. Sanchez-Sanz, Vessel confinement contributions to thermo-acoustic instabilities of premixed flames, *Bulletin of the American Physical Society* 63 (2018).
- [30] B. Radisson, J. Piketty-Moine, C. Almarcha, Coupling of vibro-acoustic waves with premixed flame, *Physical Review Fluids* 4 (121201) (2019).
- [31] J. Bechtold, M. Matalon, The dependence of the markstein length on stoichiometry, *Combustion and Flame* 127 (1906–1913) (2001).
- [32] J. De Vries, W. B. Lowry, Z. Serinyel, H. J. Curran, E. L. Petersen, Laminar flame speed measurements of dimethyl ether in air at pressures up to 10 atm, *Fuel* 90 (331–338) (2011).
- [33] G. Joulin, T. Mitani, Linear stability analysis of two-reactant flames, *Combustion and flame* 40 (235–246) (1981).
- [34] P. Garcia-Ybarra, C. Nicoli, P. Clavin, Soret and dilution effects on premixed flames, *Combustion Science and Technology* 42 (87–109) (1984).
- [35] C. K. Westbrook, F. L. Dryer, Simplified reaction mechanisms for the oxidation of hydrocarbon fuels in flames, *Combustion science and technology* 27 (31–43) (1981).

- [36] E. Fernández-Tarrazo, A. L. Sánchez, A. Liñán, F. A. Williams, A simple one-step chemistry model for partially premixed hydrocarbon combustion, *Combustion and Flame* 147 (32–38) (2006).
- [37] Y. B. Zeldovich, D. Frank-Kamenetskii, A theory of thermal flame propagation, *Zhurnal Fizicheskoi Khimii* 12(1) (100–105) (1938).
- [38] V. Kurdyumov, E. Fernandez-Tarrazo, Lewis publisher effect on the propagation of premixed laminar flames in narrow open ducts, *Combustion and Flame* 128 (382–394) (2002).
- [39] J. Daou, M. Matalon, Influence of conductive heat-losses on the propagation of premixed flames in channels, *Combustion and Flame* 128 (321–339) (2002).
- [40] M. Sánchez-Sanz, Premixed flame extinction in narrow channels with and without heat recirculation, *Combust. Flame* 159 (3158–3167) (2012).
- [41] S. Kang, S. Baek, H. Im, Effects of heat and momentum losses on the stability of premixed flames in a narrow channel, *Combustion Theory and Modelling* 10 (659–681) (2006).
- [42] D. T. Blackstock, Fundamentals of physical acoustics, no. 325, 2000 (2000).
- [43] Y. Shtemler, G. Sivashinsky, On upward propagating flames, *Combustion science and technology* 102 (81–93) (1994).
- [44] D. Fernández-Galisteo, V. N. Kurdyumov, Impact of the gravity field on stability of premixed flames propagating between two closely spaced parallel plates, *Proceedings of the Combustion Institute* 37 (1937–1943) (2019).
- [45] BOSCH, Bosch duraspeed specifications, 2017.
- [46] F. Veiga-López, D. Martínez-Ruiz, E. Fernández-Tarrazo, M. Sánchez-Sanz, Experimental analysis of oscillatory premixed flames in a hele-shaw cell propagating towards a closed end, *Combustion and Flame* 201 (1–11) (2019).
- [47] A. Zel'Dovich, A. Istratov, N. Kidin, V. Librovich, Flame propagation in tubes: hydrodynamics and stability, *Combustion science and technology* 24 (1–13) (1980).

- [48] A. Levy, An optical study of flammability limits, Proceedings of the Royal Society of London. Series A. Mathematical and Physical Sciences 283 (134–145) (1965).
- [49] N. Otsu, A threshold selection method from gray-level histograms, IEEE transactions on systems, man, and cybernetics 9 (62–66) (1979).
- [50] Numpy manual, <https://docs.scipy.org/doc/numpy/reference/routines.fft.html>, accessed: 2020-03-01.

2.A Image analysis and post-processing

Image analysis

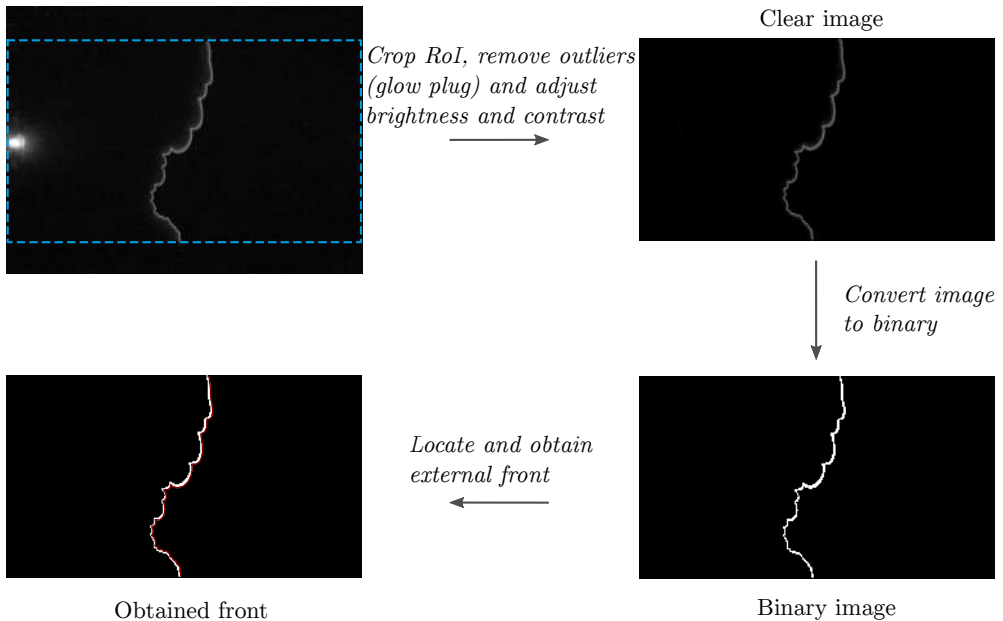


FIGURE 2.26 | Workflow followed for post-processing each frame of the experimental videos.

Most of the images and videos obtained at the Universidad Carlos III laboratory were analyzed following the steps summarized in the workflow shown in Fig. 2.26. For that purpose, we use Fiji or an in-house Python code which are used depending on the volume of the data. We first crop the original images/frames to just analyze the RoI (which is approximately the visible Hele-Shaw area) and save as much time as possible. Next, we delete any possible outliers that may appear during a test and do not add any important information, such as the bright glow plug or any other shiny points that may appear due to the combustion of any small solid particles present at the chamber. Then, the brightness and contrast of the images is modified –case dependet– to better distinguish the flame. Once the images/frames are clear enough, we convert it into binary. The *Otsu* method [49] is applied to calculate the luminosity threshold and used to categorize every pixel between black and white. From the binary images we extract the external continuous front of the propagating waves, which corresponds to the tip of the

Poiseuille-like flames, and perform the post-processing steps explained in the following section.

Post-processing

The obtained fronts delimit the boundary between the hot reaction products and the to-be-burned fresh reactants. Knowing the coordinates of every single point that conforms the front, we are able to calculate the burned volume fraction of burned gases, defined as $V_b/(W \times L \times h)$. As said before, the flame velocity is calculated considering a flat flame with the same burned volume as the wrinkled one obtained in our experiments, that is $U_L = (Wh)^{-1}dV_b/dt$. Characteristic measures were shown before in, for example, Fig. 2.4.

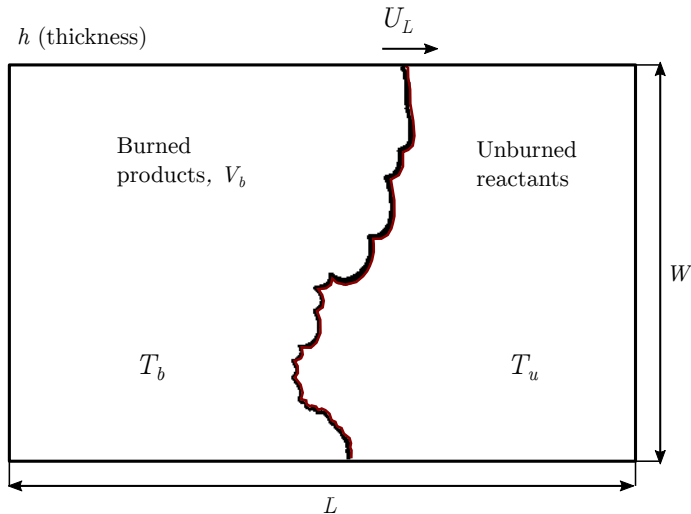


FIGURE 2.27 | Schematic of the domain used for the calculation of the burned volume of the flame.

We also performed a frequency analysis (Figs. 2.9 and 2.8) of the oscillatory signals (both velocity and the recorded acoustic pressure waves). The Fourier spectra of each signal was obtained using the FFT (Fast Fourier Transform) approach of *Numpy* in Python, thus obtaining directly the accumulated power at each frequency of the signals. Furthermore, the variation of the frequency peaks with time is obtained by dividing the complete signal in smaller signals whose center is scrolled from its start to its end. The reader may consult more detailed information of the algorithms at the *Numpy* manual [50].

CHAPTER 3

Thermoacoustic instabilities in buoyant lean hydrogen flames

Among the possible alternatives, hydrogen emerges as an important player in the unavoidable energy transition that is already taking place [1, 2]. Its high energy density, null CO₂-free emissions when used in combustion applications, abundance in nature and wide range of flammability [3] confer hydrogen upon interesting qualities to become of major importance in the generation of energy. Also, hydrogen can be used to storage the excess of energy from renewable sources when their peak of production exceeds the demand –just by using this excess of energy to produce it– and become the main actor in the transport and distribution of renewable energy between two distant places [4]. However, the massive utilization of hydrogen is dragged by the energy toll associated with its production and transport [5, 6], potential safety issues (see chapter 5 and 6; [7]) in fuel cells and flame instabilities when used as fuel in power-generation systems. Furthermore, the necessity of a particular infrastructure to promote and popularize its use is somehow challenging and dependent on political decisions [8]. Still, its use is expected to increase in the upcoming future, overcoming the above-mentioned technological and social inconveniences [9, 10].

Regarding combustion systems, lean hydrogen flames are inherently highly unstable. The main difference with the previous fuels is its characteristic high mass diffusivity, that yields Lewis numbers much lower than one ($Le \sim 0.3$) and promoting the onset of thermodiffusive instabilities [11]. Furthermore, it is also at these mixture conditions where thermoacoustics are found for hydrogen-air flames [12].

To further understand the stability of this promising alternative fuel, a variety of experimental conditions are described in this chapter to dig down on the behavior of lean premixed hydrogen flames propagating under the effect of gravity, related to the onset and damping of thermoacoustic instabilities. The composition of the mixture, the thickness of the channel and buoyancy are known to play decisive roles in hydrocarbon and ether gaseous flames (chapter 2). However, hydrogen-air mixtures may behave considerably different to classical fuels. To follow a similar procedure than in the previous chapter, we first analyze downward-propagating flames ($\alpha = -90^\circ$ chosen to be the base case due to the stabilizing nature of the RT instability) and then shift the vessel to analyze the influence of gravity when propagating towards the opposite direction $\alpha = 90^\circ$.

3.1 Experimental setup and procedure

The combustion chamber used for these experiments, sketched in Fig. 3.1, is conformed by two 10-mm-thick *Plexiglas* plates separated by a PVC sealing hollow frame, being the total volume enclosed by the cell $950 \times 200 \times (10 - 4) \text{ mm}^3$ ($L \times W \times h$). Once more, the gap height h can be modified by changing the frame to assess effects related to heat losses and viscous damping.

Hydrogen and air are mixed before entering the combustion chamber, controlling the fuel-to-air ratio with two precise EL-FLOW mass-flow controllers, which keep the error of the concentration of hydrogen within $\pm 1\%$. Prior to combustion, the mixture is fed via an injection port located at the ignition side of the chamber, keeping this end closed and opening the venting valve at the opposite side. The stratification problem introduced in the previous chapter is not seen here. As hydrogen is lighter than air, it would only appear when filling from below to perform an upward-propagating flame test. However, the only available section to abandon the vessel is a small valve and most of the mixture is kept inwards. To check the complete charge of the chamber and the homogeneity of the mixture, we measure the composition of the mixture at the outlet line using a gas analyzer RosemountTM CT5400 and compare it to that of the inlet. After a minute of exposure, the ignition end is fully reopened (no obstacles at the outflow end), the opposite-end valve is closed, and the mixture is ignited by a spark plug, to discharge a high amount of energy in a very local area and avoid the heating of the surrounding

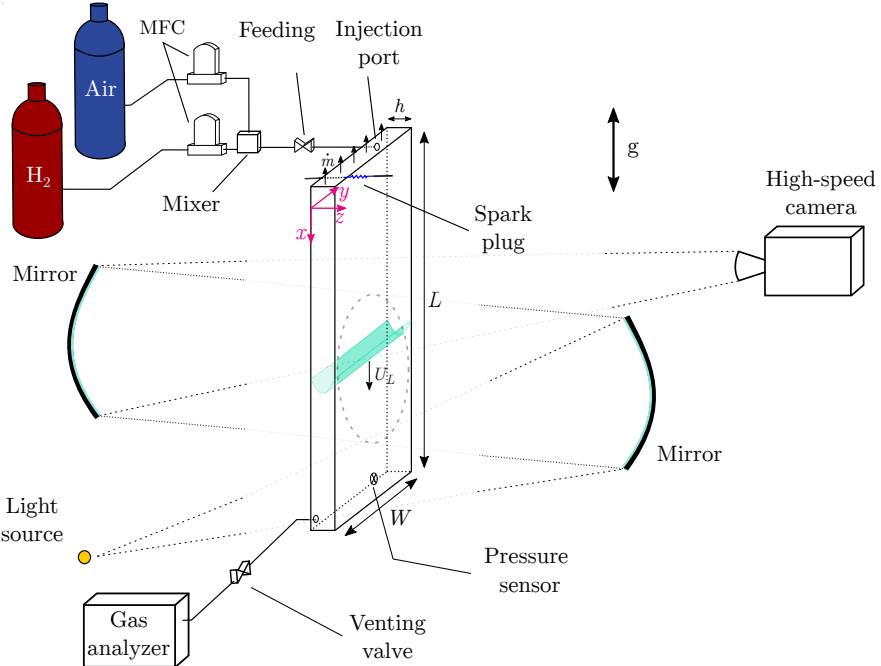


FIGURE 3.1 | Schematic of the experimental setup. High-speed images recorded using a Z-shape Schlieren system. The dimensions of the cell $L \times W \times h$ are included in the sketch. The black arrows at the ignition end of the chamber represent the totally unobstructed exit of the hot reaction products.

mixture and the consequent appearance of buoyant phenomena. The flames propagate towards a completely closed end in all the cases studied here, which produces a necessary acoustic reflection to trigger the phenomena under study.

A Z-shape Schlieren optical system with a LED light source, two 280-mm-diameter mirrors, a set of lenses and a high-speed camera (Photron FASTCAM SA 1.1) is used to capture images of the flame front propagation. Due to the limited size of the mirrors, only partial visualization of the setup was possible during each experiment. The chamber can be shifted vertically to displace the region under consideration, thus capturing the whole channel length in consecutive trials. Additionally, a pressure sensor (PCB M113B12) is located at $x \sim 900$ mm to measure the acoustic pressure oscillations, with an accuracy of $\pm 0.8\%$.

TABLE 3.1 | Properties of lean hydrogen-air mixtures calculated at ambient temperature and pressure.

%vol. H ₂	ϕ	T _b [K]	S _L [cm/s]	Le	δ_T [mm]	Fr ² × 10 ⁻³
6	0.15	784	2.9	0.32	0.83	9
6.5	0.17	823	3.6	0.33	0.67	13
9.5	0.25	1055	10	0.34	0.24	102
10	0.26	1093	11	0.34	0.22	123
11	0.29	1169	15	0.34	0.16	229
12	0.32	1244	19	0.35	0.13	368
13	0.36	1319	23	0.35	0.10	539
14	0.39	1393	28	0.36	0.09	799
15	0.42	1466	35	0.36	0.07	1249

The main properties of the analyzed hydrogen-air mixtures are shown in Table 3.1 and were calculated following the methodology introduced by Yañez and Kuznetsov [12]. Values not reported in [12] were calculated using Cantera and PREMIX (Chemkin II) codes.

3.2 Effect of the mixture composition for downward-propagating flames

The effect of the equivalence ratio ϕ is evaluated by keeping a constant 10-mm gap size h for downward-propagating flames ($\alpha = -90^\circ$). For mixtures with an equivalence ratio lower than a critical value, $\phi \leq \phi_c = 0.36$, the flame experiences strong oscillations due to the coupling with the acoustic waves present in the chamber. These oscillations can be compared to those found in chapter 2 [13] for rich (lean) enough propane and DME (methane) mixtures propagating in a similar geometry. We follow here the same criteria to those stated for carbon-based fuels, considering that a flame experiences secondary acoustic oscillations when simultaneously the over-pressure peak exceeds 1 kPa, the flame position shows a sudden slope change and there are important modifications in the overall outline of the front.

The left panel of Fig. 3.2 (a) shows the temporal evolution of the flame velocity U_L of an hydrogen-air flame with equivalence ratio $\phi = 0.26$. The instantaneous flame velocity U_L was calculated again as $U_L = (Wh)^{-1}dV_b/dt$, considering a flat flame with the same burned volume V_b . Note that, because of a limitation in the visualization region, a discontinuous signal was obtained from consecutive experiments. Figure 3.2 (b)-left represents the over-pressure within the combustion chamber, upholding the coupling between flame and acoustics that is

confirmed later by observing the matching between the Fourier spectra of both the pressure and velocity signals depicted in Fig. 3.2 (c)-left. In this case, the over-pressure rises up to 3 kPa producing associated maximum flame velocities of around 4 m/s.

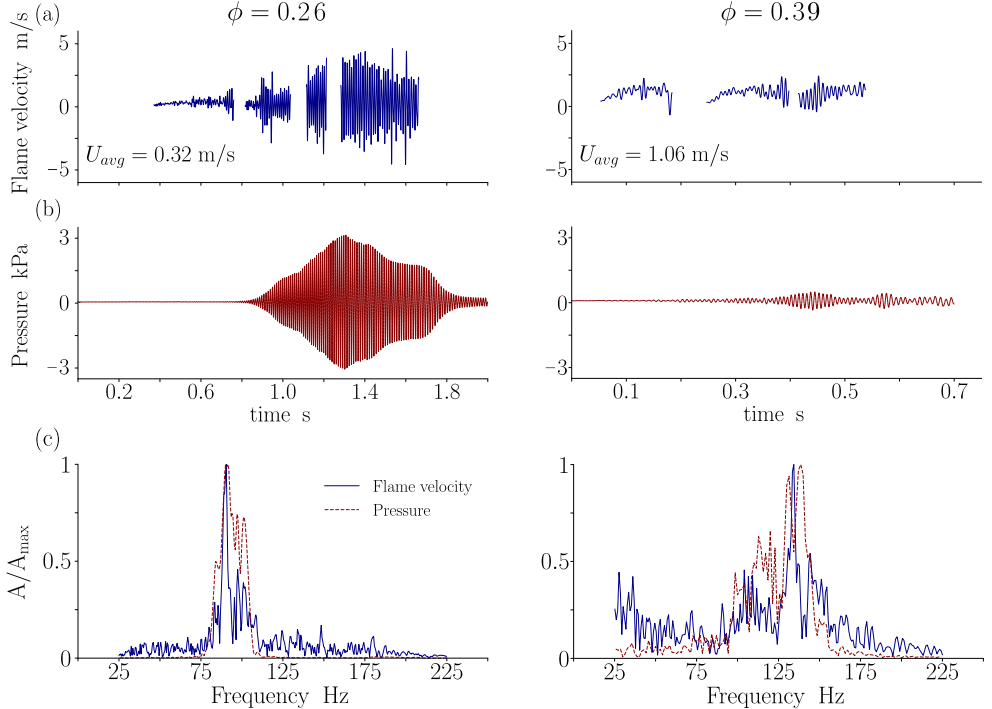


FIGURE 3.2 | (a) Evolution of the flame velocity with time, for leaner (left) and richer (right) conditions than $\phi_c = 0.36$. The error on the calculation of the velocity is around $\pm 2\%$. (b) Over-pressure signal at the interior of the chamber. (c) Fourier spectra of both signals normalized with the maximum amplitude. The maximum error for these calculations is $\pm 3 \text{ Hz}$

Figure 3.3 (a)-(f) shows characteristic snapshots of the transition to secondary acoustic instability for a mixture with equivalence ratio $\phi = 0.26$. Once ignited, Fig. 3.3 (a) shows how the flame soon ripples due to hydrodynamic and thermodiffusive instabilities. At this point, the characteristic wavelength of the cells is $\lambda_{\phi=0.26} \sim 6 \text{ mm}$. Further down (Fig. 3.3 (b)), some of the frequencies of the ignition noise ($f \approx 85 - 105 \text{ Hz}$ –mixture dependent–) are amplified by the presence of the reactive front, undergoing a feedback mechanism between each other. Here, the flame becomes nearly planar, propagating with an average velocity five times faster than the correspondent laminar burning velocity S_L experiencing small-amplitude

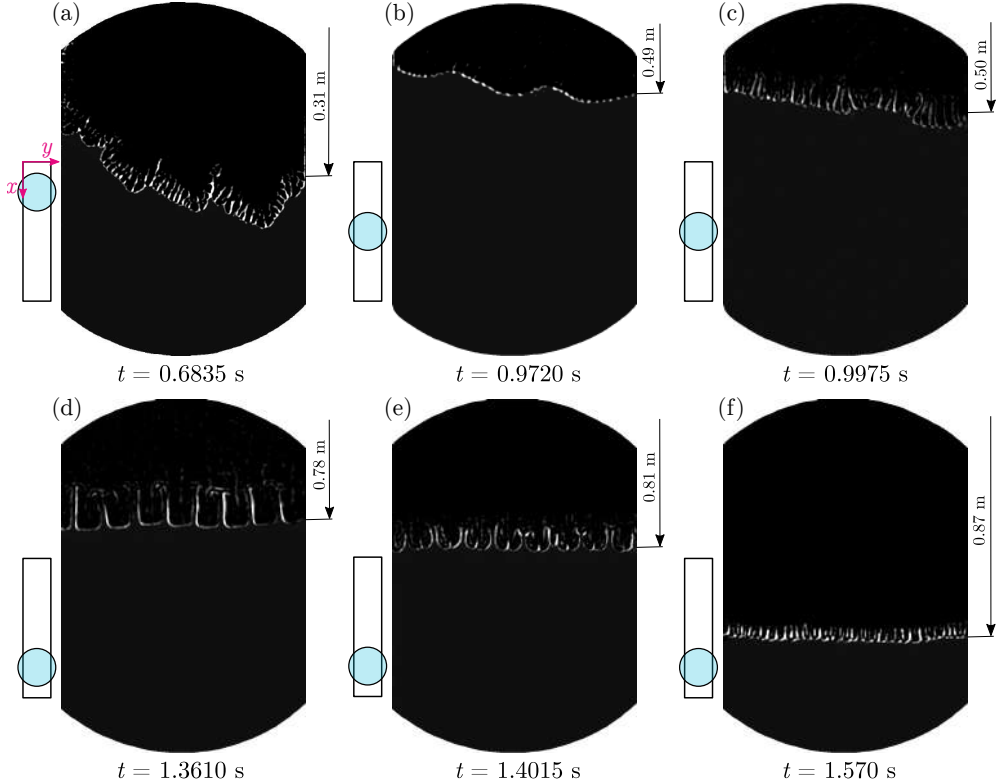


FIGURE 3.3 | Shadow images of a flame propagating downwards in the secondary acoustic oscillatory regime ($\phi = 0.26 < \phi_c$) at different times. The left-side schemes represent the region captured during each experiment, and the right-side arrows indicate the distances from the front mid-point to the open top end.

oscillation at the acoustic frequency. Shortly after, in Fig. 3.3 (c), the pressure waves are further magnified triggering the transition to the secondary regime that is identified by the formation of small wrinkles on the quasi-planar flame front with a characteristic wavelength $\lambda_{\phi=0.26} \sim 6.5$ mm. As it is illustrated in Fig. 3.3 (d-e), under the effect of such high-amplitude pressure waves, the reactive front evolves to form flame cells with a longer characteristic wavelength $\lambda_{\phi=0.26} \sim 25$ mm with funnels penetrating towards the region occupied by the hot products (d). The pressure-driven flame oscillates at the acoustic frequency with peak flow velocity around $|U_L| \sim 4$ m/s, one order of magnitude higher than S_L . During the next oscillation period (e), the flame tips at the mid-position of the flame cells evolve to form the long funnels, doubling the oscillation period at these particular points (mid-points of the cells and funnels). Nevertheless,

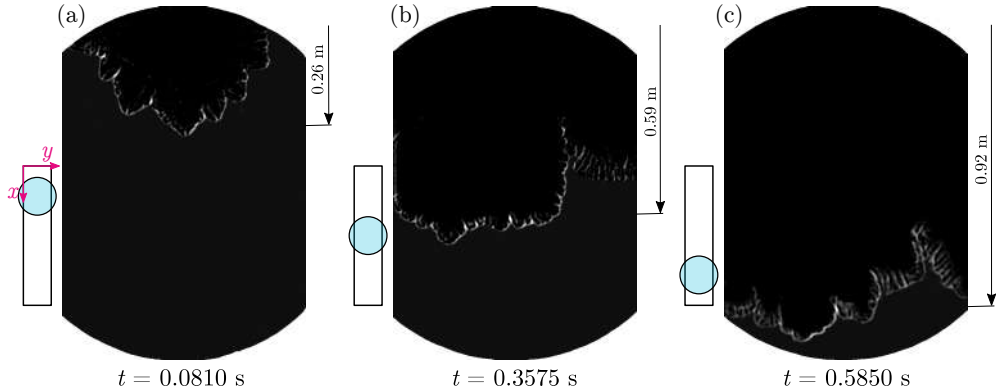


FIGURE 3.4 | Shadow images of a flame propagating downwards in the primary acoustic oscillatory regime ($\phi = 0.39 > \phi_c$) at different times.

the oscillation frequency of the average reaction front position $x_L = \int_0^t U_L dt$ matches the frequency imposed by the pressure waves, as stated by Markstein [14] and Searby [15]. Finally, in Fig. 3.3 (f), the amplitude of the movement is reduced as well as the size of the wrinkles during the final approach to the end of the chamber.

However, for richer H₂-air mixtures ($\phi > \phi_c = 0.36$), only primary acoustic oscillations are observed. The right panels of Fig. 3.2 (a)-(c) show the characteristic velocity observed in a flame with $\phi = 0.39$, the over-pressure within the chamber and the normalized Fourier spectra of the signals respectively. Furthermore, Fig. 3.4 (a)-(c) were taken from experiments of flames propagating downwards under the effect of the primary acoustic instability only. Right after ignition (a), the flame shows a similar petal-like shape to that of the previous case. At approximately the half of the combustion chamber (b), the front experiences small-amplitude ($|U_L| \approx 0.5$ m/s) oscillations with a frequency of $f \approx 135$ Hz. The flame front becomes mostly planar by the effect of this weak flame-wave interaction, propagating with a similar outline until it reaches the end wall of the combustion chamber (c).

Further enrichment of the mixture introduces different instability mechanisms to the problem which are out of the scope of this work (chapter 4, **Future work**). There, thermoacoustic processes begin to be less important, becoming even negligible.

3.3 Effect of the channel gap thickness h

The influence of the gap size h on the flames propagation is analyzed by changing the hollow frame thickness from 10 to 4 mm with a 2-mm step for different hydrogen-air mixtures. Figure 3.5 shows, (a) the variation of the maximum positive chamber pressure and (b) the peak frequency of the waves over equivalence ratio for different h . The shadowed areas of Fig. 3.5 (a) represent the primary thermoacoustic regions in the pressure- ϕ parametric space.

Modifying the channel thickness h leads to two main changes in the experiments. First, the surface-to-volume ratio increases for decreasing h . This amplifies the conduction heat losses to the surrounding solid walls from both the reaction region and the hot combustion products. Also, thinner channels lead to the increment of viscous dissipation of the acoustic waves. Remember that the acoustic dissipation rate due to viscosity in a channel can be estimated by means of $\sim \mu(w^2/h^2)$, with μ the viscosity of the mixture and w the induced velocity of the flow. For thin enough channels, the characteristic acoustic and viscous dissipation times are comparable, thus preventing the arising of acoustic instabilities by reduction of the channel over-pressure when decreasing h . Furthermore, the peak frequencies of the oscillations slightly reduce due to the diminished flame temperature, directly related to the speed of sound $c = \sqrt{\gamma_g \mathcal{R}T}$. Momentum dissipation affects the upper transition limits to the secondary acoustic oscillations, reproducing the same behaviour –but opposite– than DME, modifying the critical equivalence ratio from $\phi_c \approx 0.36$ ($h = 10$ mm) to $\phi_c \approx 0.32$ ($h = 4$ mm). Also, it should be noted from Fig. 3.5 (a) and (c) that for mixtures of $\phi \leq 0.25$, channels with $h \leq 8$ mm yield major attenuation of pressure waves recovering primary acoustic oscillations.

Figure 3.6 shows three characteristic images in the evolution of a near-limit flame $\phi = 0.25$ propagating in a 4-mm gap. As explained above for thicker channels or sufficiently rich mixtures, it first oscillates smoothly at the sound frequency without modifying its general outline (a), dominated by hydrodynamic and thermodiffusive instabilities. Later, characteristic quenched areas appear along the front as marked in (b). In fact, heat losses are found to be critical close to the lean flammability limit, being responsible for breaking the front into several parts. Further down the broken front keeps dividing along its propagation (c), zigzagging until it reaches the end of the combustion chamber. This discontinuity of the front leaves several open warm-gases corridors for the acoustic waves to traverse the chamber weakly interacting with the flame. The

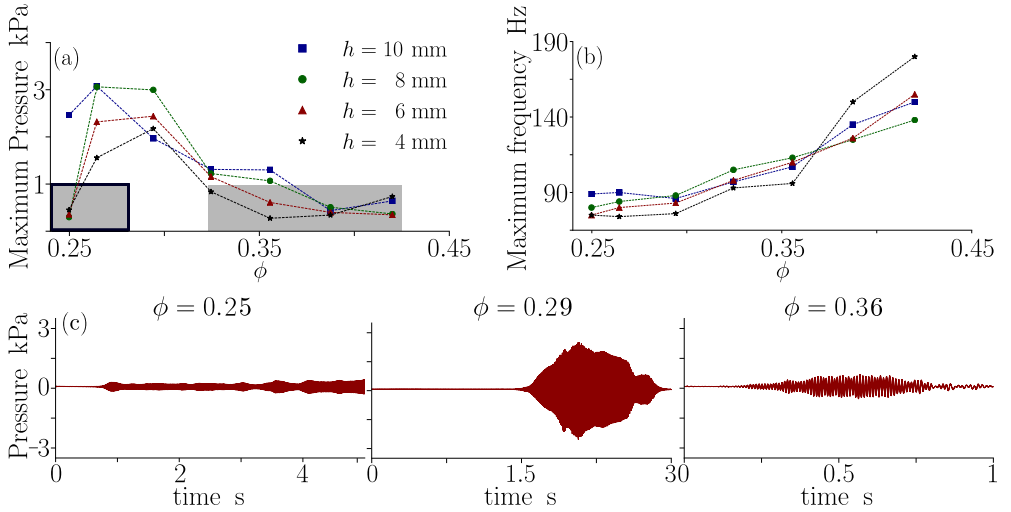


FIGURE 3.5 | (a) Variation with ϕ of the maximum acoustic pressure in the channel for varying width $h \pm 1\%$. Shadowed areas represent the regions of primary acoustic instability regime. (b) Effect of ϕ on the maximum oscillation frequency for different $h \pm 1\%$. (c) Over-pressure signals obtained in the interior of a $h = 6$ mm chamber for different ϕ .

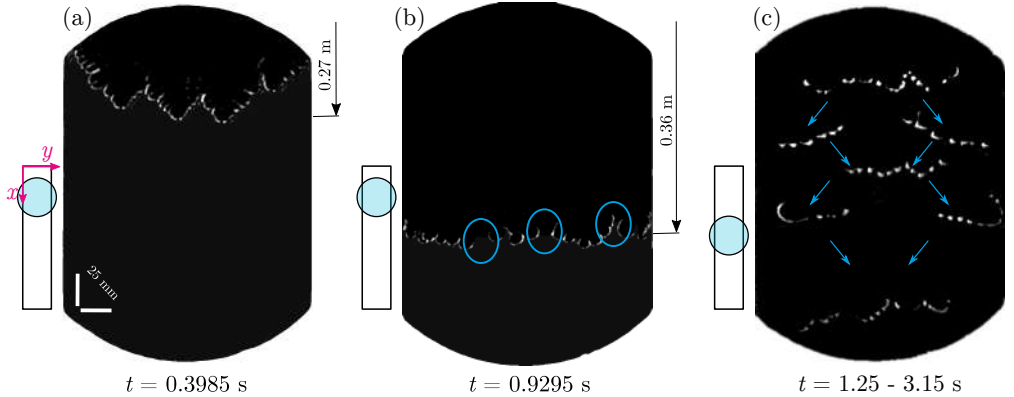


FIGURE 3.6 | (a)-(c) Post-processed shadow images of a flame propagating downwards in the attenuated primary acoustic oscillations regime for $\phi = 0.25$ and $h = 4$ mm. The cyan circles indicate the partially-quenched areas.

lower density jump across the front produces a softer reflection of the acoustic waves locally. The feedback interaction is not as strong as for a 10-mm channel, where no quenched areas were found for the same mixture. The waves do not exceed 1-kPa pressure peaks and the flames are not able to transit to the secondary acoustic oscillation regime.

Further reduction of the gap thickness unveils two unprecedented propagation regimes that claim for a separated and detailed study, which is given in chapter 5 [16] and 6 [7] of this dissertation. Again, acoustics are almost out of the equation and the discovered phenomena are controlled by other physical mechanisms.

3.4 Effect of buoyancy

Although being so special, hydrogen is also affected by the Rayleigh-Taylor instability, as well as the previous studied fuels. Again, we evaluate how strong its influence is by reversing the combustion chamber ($\alpha = 90^\circ$) and, therefore, the front is set to travel upwards. We do not modify the channel gap size, maintained constant at $h = 10$ mm, but we do vary the composition of the ignited mixture to modify the propagation velocity and the thickness of the flames. Note again that the Rayleigh-Taylor instability becomes stronger the weaker the flame.

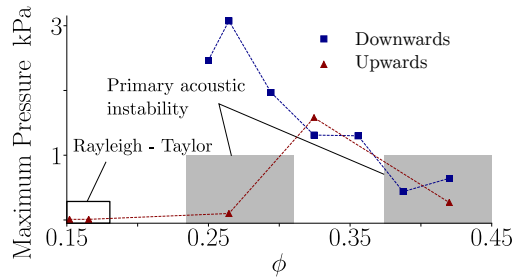


FIGURE 3.7 | Inner pressure within a $h = 10$ mm Hele-Shaw cell over equivalence ratio ϕ for upward- and downward-propagating flames.

The maximum over-pressure within the combustion chamber is plotted in Fig. 3.7 for both upwards and downwards propagating flames as a function of the equivalence ratio. The flammability limits for lean upward-propagating hydrogen-air flames are extended as a consequence of the gravity-induced flow and of the flame curvature, which enhance flame burning and allows the ignition of leaner mixtures than in the downward-propagating flames. Figure 3.8 shows representative frames (at $x \sim 0.7$ m from the open ignition end) of flames propagating upwards for the tested mixtures with the corresponding recorded acoustic signals.

From Fig. 3.7 we know that the effect of gravity is almost negligible for sufficiently fast flames ($\phi \geq 0.32$ and $Fr^2 \geq 0.37$) and the microphones placed inside the combustion chamber

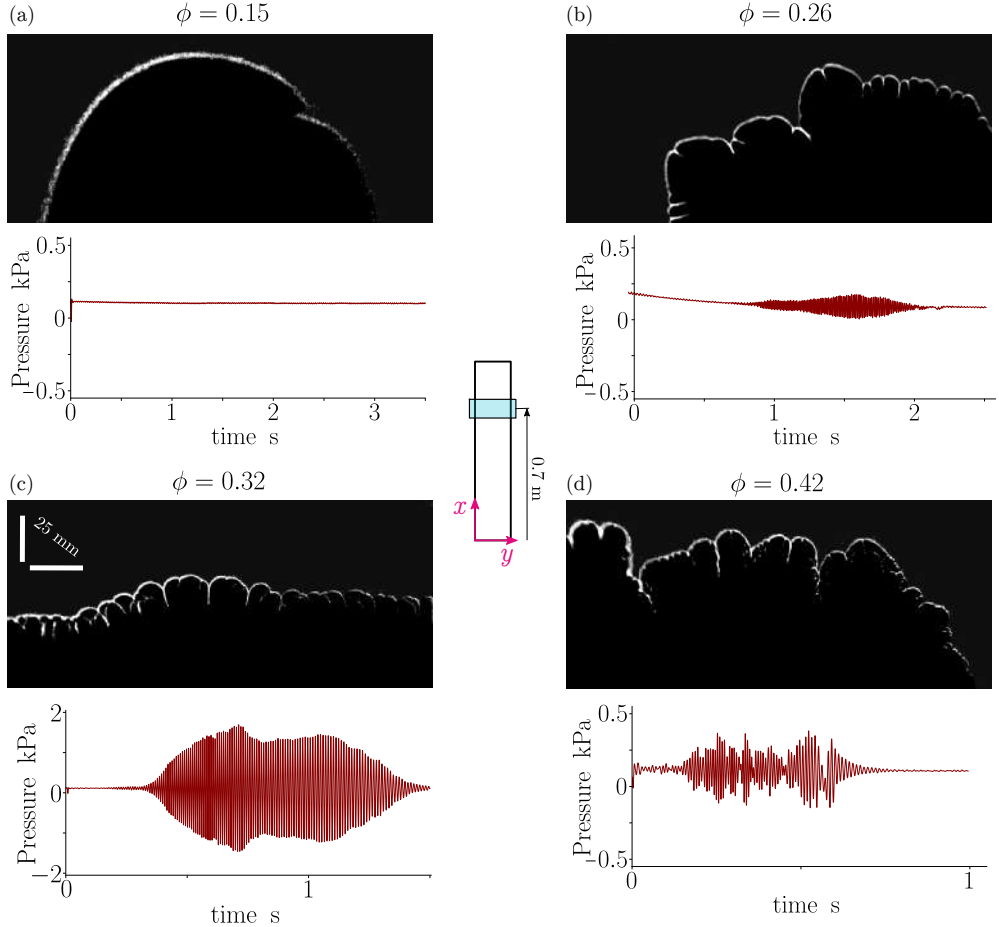


FIGURE 3.8 | Flame front shapes and recorded over-pressure at the combustion chamber for different hydrogen-air mixtures of upward-propagating flames. The range of acoustic pressure is not kept constant in subfigure c) to facilitate the reading of the figures.

only measured slight changes in the acoustic pressure. As an example, we include in Fig. 3.8 (d) the pressure changes measured for a flame with $\phi \geq 0.32$ that propagates in the primary acoustic instability regime. Fig. 3.8 (c) shows a flame leaner than $\phi_c = 0.36$, undergoing secondary oscillations as explained before for downward-propagating flames with no noticeable changes from gravity effects.

As for methane (chapter 2), a new transition from secondary to primary instabilities is identified for leaner mixtures $\phi = 0.26$ in Fig. 3.8 (b), where the flame front remains almost

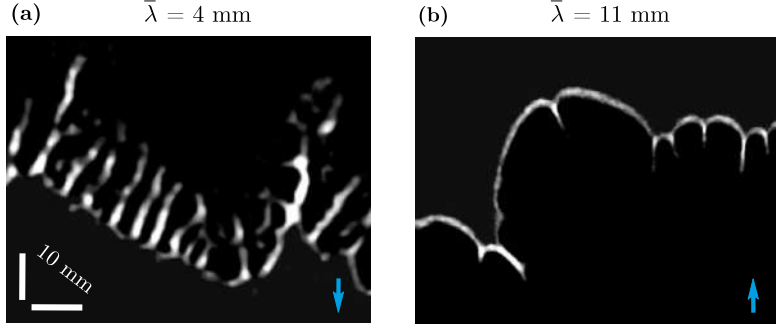


FIGURE 3.9 | Front detail of two $\phi = 0.26$ flames. The cyan arrows on the bottom corner of the images define the propagation direction. Additionally, the mean wavelength ($\bar{\lambda}$) of each flame front wrinkles is written on top of its correspondent picture.

unperturbed by acoustics during its whole propagation. Unlike downward-propagating flames, the change in the maximum acoustic pressures is reduced to a mere 100 Pa. It is clear that gravity ($Fr^2 \leq 0.12$) has an effect on the development of acoustically-driven flame vibrations, eliminating the strong oscillations and favouring the weak primary ones.

We show in Fig. 3.9 two detail pictures of a $\phi = 0.26$ flame moving towards opposite directions before the acoustics exerts any influence on the propagation of the flame. In Fig. 3.9 (a), the flame propagating downwards presents a wrinkled front with average wavelength $\bar{\lambda} = 4 \text{ mm}$ that emerge due to hydrodynamic and thermodiffusive instabilities. When moving upwards, gravity modifies the outline of the flame Fig. 3.9 (b) tripling the average wavelength number of the cells formed in the reactive front $\bar{\lambda} = 11 \text{ mm}$. This effect was introduced in chapter 2 (see Fig. 2.21), where despite the overall destabilizing effect for all wavenumbers, the tangential flow generated by the curved tip of the flame front leaves a smoother front.

From these observations and the results obtained in the previous chapter, we propose the flame shape, characterized by the average wrinkling of the front, as an additional parameter controlling the response of the flame to acoustics perturbations: as the reactive front becomes smoother, the flame becomes more stable regarding thermoacoustic instabilities. To further check this hypothesis, we tested very lean mixtures ($\phi = 0.15$) dominated by buoyancy as $Fr \rightarrow 0$ in Fig. 3.8 (a). Here, the front is very smooth and acquires the bubble shape characteristic delineated by Rayleigh-Taylor instability, as shown by Levy [17] for other fuels. The characteristic size of the bubble flame is of the order of magnitude of the channel width

$\bar{\lambda} \sim W \simeq 200$ mm, with all the smaller unstable cells convected by the induced tangential flow [18]. As shown in Fig. 3.8 (a), the pressure recorded within the chamber is constant, evidencing zero feedback between the bubble-like flame and the pressure waves. In slightly richer mixtures ($\phi = 0.17$) –not shown in the figure– a double-headed flame of similar characteristics is observed, again, with no flame-acoustic interaction.

References

- [1] P. E. Miranda, Science and engineering of hydrogen-based energy technologies: Hydrogen production and practical applications in energy generation (2018).
- [2] B. Zohuri, Hydrogen energy: Challenges and solutions for a cleaner future (2018).
- [3] I. Jain, Hydrogen the fuel for 21st century, International journal of hydrogen energy 34 (7368–7378) (2009).
- [4] D. Teichmann, W. Arlt, P. Wasserscheid, Liquid organic hydrogen carriers as an efficient vector for the transport and storage of renewable energy, International Journal of Hydrogen Energy 37 (18118–18132) (2012).
- [5] S. Niaz, T. Manzoor, A. H. Pandith, Hydrogen storage: Materials, methods and perspectives, Renewable and Sustainable Energy Reviews 50 (457–469) (2015).
- [6] A. M. Abdalla, S. Hossain, O. B. Nisfindy, A. T. Azad, M. Dawood, A. K. Azad, Hydrogen production, storage, transportation and key challenges with applications: a review, Energy conversion and management 165 (602–627) (2018).
- [7] F. Veiga-López, M. Kuznetsov, D. Martínez-Ruiz, E. Fernández-Tarrazo, J. Grune, M. Sánchez-Sanz, Unexpected propagation of ultra-lean hydrogen flames in narrow gaps, Physical Review Letters (2020).
- [8] I. R. E. Agency, Hydrogen from renewable power, Abu Dhabi, 2018.
- [9] I. R. E. Agency, Hydrogen: a renewable energy perspective, Abu Dhabi, 2019.
- [10] I. H. Council, Hydrogen scaling up, 2017.
- [11] P. Clavin, G. Searby, Combustion waves and fronts in flows: flames, shocks, detonations, ablation fronts and explosion of stars (2016).
- [12] J. Yanez, M. Kuznetsov, J. Grune, Flame instability of lean hydrogen–air mixtures in a smooth open-ended vertical channel, Combustion and Flame 162 (2830–2839) (2015).

- [13] F. Veiga-López, D. Martínez-Ruiz, E. Fernández-Tarrazo, M. Sánchez-Sanz, Experimental analysis of oscillatory premixed flames in a hele-shaw cell propagating towards a closed end, *Combustion and Flame* 201 (1–11) (2019).
- [14] G. H. Markstein, Instability phenomena in combustion waves, *Proceedings of the International Symposium on Combustion* 4 (44–59) (1953).
- [15] G. Searby, Acoustic instability in premixed flames, *Combustion Science and Technology* 81 (221–231) (1992).
- [16] D. Martínez-Ruiz, F. Veiga-López, D. Fernández-Galisteo, V. N. Kurdyumov, M. Sánchez-Sanz, The role of conductive heat losses on the formation of isolated flame cells in hele-shaw chambers, *Combustion and Flame* 209 (187–199) (2019).
- [17] A. Levy, An optical study of flammability limits, *Proceedings of the Royal Society of London. Series A. Mathematical and Physical Sciences* 283 (134–145) (1965).
- [18] A. Zel'Dovich, A. Istratov, N. Kidin, V. Librovich, Flame propagation in tubes: hydrodynamics and stability, *Combustion science and technology* 24 (1–13) (1980).

CHAPTER 4

Conclusions and future work

Discussion and conclusions

Thermoacoustic instabilities in narrow channels are studied experimentally for propane-, DME-, methane- and lean hydrogen-air premixed flames. In particular, we assess the effect of equivalence ratio, channel thickness and gravity on the transition between the two recurrently-found main regimes: from the primary to the secondary oscillatory instability.

During the primary acoustic oscillations, the flame remains mostly unperturbed by the pressure waves. It flattens and oscillates at a dominant frequency until reaching the end of the channel. When the regime changes, the front experiences violent oscillations related to the high acoustic pressure peaks (~ 5 kPa) within the chamber. Additionally, the outline of the flame changes, presenting a characteristic finger-like shape up to its arrival at the closed end of the chamber, where the waves are attenuated.

For horizontal non-buoyant conditions –all fuels but hydrogen–, the transition to the secondary acoustic instability appears in fuel-air blends richer than a critical value for propane ($\phi_c = 0.87$) and DME ($\phi_c = 0.55$) and in mixtures leaner than $\phi_c = 0.95$ for methane. Similar qualitative results are found for downward-propagating flames of carbon-based fuels, where the stabilizing effect of gravity does not strongly modify the onset of thermoacoustics. Knowing that, we can compare both hydrocarbon and lean buoyant hydrogen deflagrations, which transits to the secondary regime for mixtures leaner than $\phi_c = 0.36$, following the same trend marked before by methane flames.

The reverse influence of the equivalence ratio on the transition from the primary to the secondary instability observed in propane, DME, methane and lean hydrogen flames cannot be explained in terms of flame temperature T_b or burning velocity S_L . As can be easily checked in Fig. 1.6, these two parameters have a non-monotonic dependence on ϕ , with similar values of T_b and S_L in rich and lean flames that do not anticipate the differences observed in the experiments.

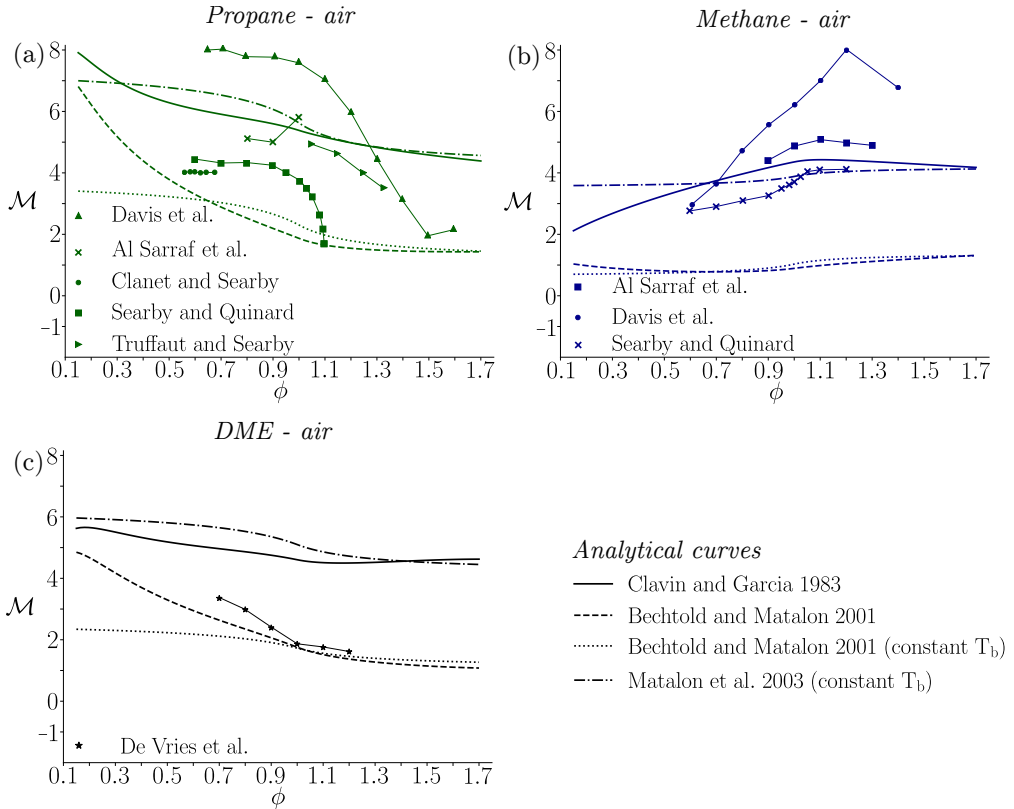


FIGURE 4.1 | Compilation of numerical (lines) and experimental (symbols) values of the Markstein number as a function of the equivalence ratio for propane, methane and DME. The experimental values were obtained from [1–6] and the theoretical models taken from [7–9].

Encouraged by the work of Aldredge and Killingsworth [10] with methane-air flames, we calculated in Table 2.1 the corresponding values of the effective Lewis number Le_{eff} and the values of the Markstein number M calculated numerically by Bechtold and Matalon [11] for methane and propane, and calculated in this work for DME from the measurements

of the Markstein length carried out by de Vries et al. [1]. Additionally, we included for lean hydrogen-air mixtures the Lewis –which equals Le_{eff} for such lean compositions– and Markstein numbers obtained from [12] in Table 3.1. Using these data, we see that the onset of the secondary instability is only observed in the experiments for \mathcal{M} below a critical value that depends on the mixture and the direction of propagation (see Table 2.1 and 3.1). This fact, together with the decrease of the Markstein number with ϕ –for the range of mixtures tested– towards rich (propane and DME) or lean (methane) mixtures (Fig. 4.1) appoints to \mathcal{M} as the possible controlling parameter of the empirical observations. Also, the same trend appears for hydrogen mixtures (Fig. 4.2), which reinforces the hypothesis.

On light of our experimental results, the Markstein number arises as the best candidate to characterize the thermoacoustic transition because of its decrease towards rich (propane and DME) and lean (methane and hydrogen) flames. Therefore, the onset of the pulsations is observed for Markstein numbers \mathcal{M} below a critical value \mathcal{M}_c , reinforcing the numerical results by Matalon and Metzener [13]. Moreover, the simulations carried out in [7, 14] concluded that short wavelength perturbations colonize the front when the Markstein number is lower, as we found for the carbon-based flames tested here (Figs. 2.5 and 3.9). Furthermore, the novel lateral view recordings reported by us depict the three-dimensional structure of several propane flames (Figs. 2.6 and 2.7). During the propagation under the effect of the primary acoustic instability, the shape of the flame is parabolic and remains that way during the small-amplitude oscillations. On the other hand, when $\mathcal{M} < \mathcal{M}_c$, just before the transition to the secondary instability, the shape of the flame transverse to the direction of propagation (z direction) abandons the parabolic profile that adopted after the ignition to become much flatter. Immediately after that, the reaction region forms small-size bulges that grow to form the finger-like cell structure that characterizes the secondary instability. Therefore, our empirical observations and their numerical findings appoint the front shape and its malleability to an external perturbation (\mathcal{M}) as the possible parameter triggering the transition between the different instability modes identified in this part of the dissertation.

However, it is still not well understood how the flame structure affects the self-induced transition between regimes. Markstein [16] proposed that local changes of the instantaneous burning velocity and temperature can be directly related to the local curvature of the flame front. That is done by the afterwards-named Markstein number, $\mathcal{M} = \mathcal{L}/\delta_T$, a

Hydrogen - air

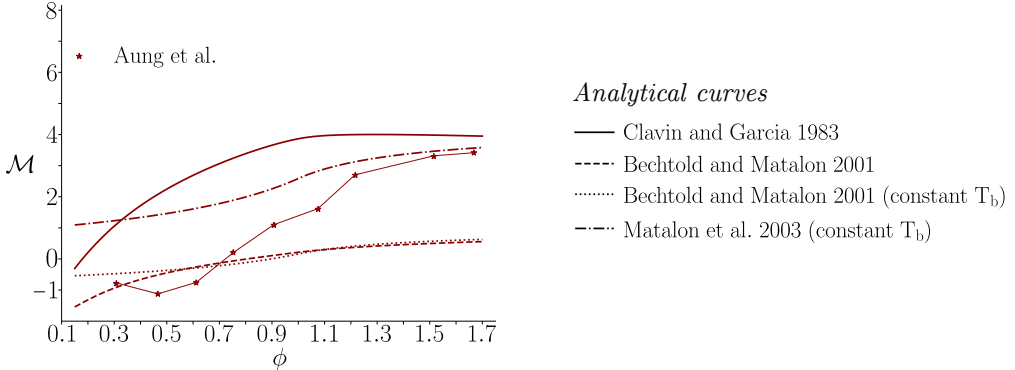


FIGURE 4.2 | Compilation of numerical (lines) and experimental (symbols) values of the Markstein number as a function of the equivalence ratio for hydrogen. The experimental values were obtained from [15] and the theoretical models taken from [7–9].

semi-phenomenological parameter defined as the ratio between the Markstein length \mathcal{L} and the flame thickness, used as the proportionality factor between the speed deviations from the laminar burning velocity S_L and the comprised effects of curvature, strain and flame surface given by \mathcal{K} , yielding

$$S_f = S_L + \mathcal{L}\mathcal{K}. \quad (4.1)$$

Several researchers followed his idea [7–9, 17–22], further developing the theoretical definition of such a concept through linear perturbation analysis in the large activation energy limit. In this limit, the dimensionless activation energy, or Zel'dovich number, is assumed to be very large $\beta \rightarrow \infty$, reducing the reaction region to a thin surface that can be treated as a discontinuity (chapter 1). In addition, the assumption of nearly-equidiffusional mixtures $\beta(Le - 1) = O(1)$ is required to ensure deviations of the flame temperature from the adiabatic flame temperature T_b of order β^{-1} and validate the thin-layer approach. This double limit yields an explicit theoretical expression for the Markstein number

$$\mathcal{M} = \frac{\mathcal{L}}{\delta_T} = \frac{1}{\gamma} \ln \frac{1}{1-\gamma} + \frac{\beta(Le_{eff} - 1)}{2} \left(\frac{1-\gamma}{\gamma} \right) \int_0^{\gamma/1-\gamma} \frac{\ln(1+x)}{x} dx, \quad (4.2)$$

where $\gamma = (\rho_u - \rho_b)/\rho_b$ is the gas expansion parameter. This mixture-dependent magnitude

proved itself very valuable in the study of general stability of flame fronts, leading to a better understanding of Darrieus-Landau and Rayleigh-Taylor instabilities.

Besides these successful studies, the strain-curvature effect described by the Markstein number was also explored in dynamical problems such as the flame-acoustic wave response. In particular, the theoretical models aiming to explain the flame-acoustic coupling followed the parametric instability analysis proposed by Markstein himself [10, 23–25]. These studies of the flame response required the integration of Mathieu’s equation to depict the resulting stability diagrams (Fig. 2.1) [25, 26] in terms of the pressure amplitudes and wavenumbers k of the perturbation that are unstable. The magnitude and frequency of the imposed acoustic pressure, the Froude number and the Markstein number were identified on Mathieu’s equation as the parameters prescribing the response of the flame to a given perturbation [25].

With this new information at hand, it seems interesting to stop, breathe and briefly analyze physically how the Markstein number influences the flame shape and its interaction with the acoustic pressure waves. Consider a wave of a determined amplitude and frequency that travels along the main direction (x) of propagation. When reaching the flame, part of this wave goes across and ignores it but the rest interacts with it, gets reflected and, depending on the nature of the front and the burned fuel, imbued –or not– with extra energy provided by the chemical reaction. How does this transfer of energy occur? Two main phenomena are of importance here: pressure and acceleration coupling. Pressure coupling is related to the sensitivity of the chemical reaction to changes in pressure and therefore its burning rate can be increased or decreased depending on the sign of the acoustic pressure variations imposed by the wave. Acceleration coupling is more complex. The dynamic velocity field imposed by the oscillatory sign of the acoustic pressure waves accelerates also the region close to the reaction front, stretching the flow at its surroundings and thus changing its local shape (surface and curvature). Additionally, the acoustic-driven flow modifies the local temperature and reactants availability. The ability of the fuel to fight against this forced unbalance is measured in terms of the effective Lewis number, which is also included in Clavin’s formulation for the Markstien number (Eq. 4.2). Therefore, the local response of the flame, related to its propagation speed, to the said shape and diffusive effects is controlled by the always-present semi-phenomenological Markstein number.

Going back to the theoretical approach, the next step was to relate the forcing-pressure

(parametric) instability, to the self-excited acoustic perturbation [27, 28]. As it was recently reported there, unstable self-induced pressure oscillations were closely related to the parametric instability regimes and the phenomena described above. However, the interactions between the flame-induced acoustic pressure and the reactive front were discussed to be far more unstable than flames propagating under an imposed pressure field, outcome that recommends caution in the interpretation of the experimental results based on predictions obtained through Mathieu's equation only.

For these reasons, the Markstein number variation for different mixtures or equivalence ratios yield modified stability criteria in the theoretical approach, making certain amplitudes and frequencies of the acoustic perturbations sufficient to sustain a strong coupling with the flame. This fact reinforces the hypothesis introduced by Aldredge and Killingsworth [10]. From our results, we conclude that it should be low enough for the flame to interact with acoustic in a strong way, giving extra energy to flow, and so being able to build up the acoustic pressure and transit to the violent secondary regime. Additionally, as stated before, the numerical calculations carried out by [7, 14] made clear that perturbations of shorter wavelengths are predominant in the front as the Markstein number decreases. This conclusion matches with the classical explanation (see 5.1 in [29]) and with our experimental observations, which show that the transition to the secondary oscillatory regime is favored in wrinkled reaction fronts of greater wavenumber (lower Lewis number).

The dependency of the Markstein number on the equivalence ratio predicted theoretically has been qualitatively confirmed using numerical calculations and experimental measurements for methane, propane, DME and even hydrogen. The alarming dispersion between the experimental results provided by different authors, shown in Fig. 4.1 and 4.2, does not enable a quantitative validation of the theoretical analysis. Furthermore, it is of critical importance to understand that the classical definition of the Markstein number mentioned above in Eq. 4.2 assumes nearly-equidiffusive mixtures ($Le \sim 1$) and large activation energy, what constitutes two primary restrictions on the application of this expression to lean hydrogen flames where diffusive-thermal instabilities and wide reaction regions are found, as was early discussed by Clavin and Williams [20] amongst others. Therefore, the validity of Mathieu's equation and the consequent stability diagrams for flame-acoustic instabilities theoretically rely on flame-sheet model perturbations and a proper definition of M , yet to be clarified for highly-diffusive

species with Le significantly below unity, and should not be used to interpret the experimental observations of lean hydrogen flames ($Le \sim 0.3$). For the reasons stated above, an extension of the classical stability analysis to mixtures with Lewis number significantly below unity is clearly required to include the effect of non-negligible reaction layer thickness and theoretically validate the experimental observations regarding the transition between the primary and secondary thermoacoustic oscillations presented here for hydrogen mixtures.

Additionally, the effect of the channel thickness h , related to the energy losses of the system, is also studied for stoichiometric DME non-buoyant and lean hydrogen downward-propagating flames. Three main modifications are found when propagating along narrower channels. First, the maximum acoustic pressure reduces for thinner channels as the viscous and heat losses become more important. Second, the transition from the primary to secondary regimes appears at leaner (richer) hydrogen (DME) flames. A strong decrease on $h < 4$ mm completely eliminates any oscillatory instability at the reaction zone and unveils strange propagating regimes for hydrogen-air mixtures (chapters 5 [30] and 6 [31]). And third, the primary acoustic oscillations are recovered for channels whose thickness is $h \leq 8$ mm for hydrogen flames close to the flammability limit ($\phi = 0.25$), behavior not reported for gaseous ether flames. It is related to the increase of energy losses (heat loss and viscous damping) to the surrounding solid walls, which provoke local extinguished areas and break these weak flames, thus reducing the acoustic coupling.

Finally, the influence of gravity was tested by studying flames that propagate upwards. Two groups of fuels are again reported given their qualitative behaviour: heavy (propane with $Le \sim 1.8$ and DME with $Le \sim 1.75$) and light (methane with $Le \sim 1$ and lean H₂ with $Le \sim 0.3$) fuels. Heavy fuels show similar trends to non-buoyant and downward propagating flames, but always reducing the maximum acoustic pressures within the chamber, translating the critical equivalence ratio towards richer mixtures. They only show a strong influence of the Rayleigh-Taylor instability when close to the upper and lower flammability limits. Regarding light fuels, for sufficiently lean and slow flames $\phi \leq 0.26$ for hydrogen and $\phi \leq 0.8$ for methane, gravity becomes critical in relation with thermoacoustics instabilities. It is at this point when the Rayleigh-Taylor instability turns out to be relevant in the description of upward-propagating flames reducing the wrinkling of the reactive front and almost eliminating the flame-acoustics coupling. For these lean mixtures, Rayleigh-Taylor dominates the flow and the flame develops

a characteristic smooth bubble shape. For such flames, thermoacoustic instability is absent. To sum up, lean downward-propagating flames of methane and hydrogen develop a wrinkled reaction front with smaller flame cells and they present a greater sensibility to acoustic feedback that rises the acoustic pressure up to 3 kPa and 5 kPa respectively. Much less acoustic feedback is found in flames propagating upwards, with bigger average cell size and less flame wrinkling, which reinforces the aforementioned hypothesis. Furthermore, rich-enough methane flames are again controlled by gravity and show zero feedback with the acoustic waves at the chamber. In between, the flame oscillates strongly as for downward-propagating flames but getting lower pressure peaks. At this region, we found a singular point around $\phi \sim 1.3$ where the secondary acoustic oscillations are recovered. The Markstein number becomes again the main actor because some studies (Fig. 4.1 (b)) defend that, for sufficiently rich compositions, its trend is no longer monotonous and could also explain the said singularity.

Future work*

The results presented in this dissertation regarding thermoacoustics contribute to better understand the phenomena involved in the onset of these instabilities. However, a considerable amount of future work needs to be done regarding this subject. We show here some ideas to be developed as well as preliminary results of surprising phenomena that appeared (in addition to those showed before) during this thesis.

Numerical and analytical studies

All the work performed here is of an experimental basis. One of the logical next steps would be to simulate the problem proposed here. Considering that all the parameters involved can be easily isolated with a numerical analysis, it would be interesting to further understand the onset of thermoacoustic instabilities and confirm the hypothesis for the main controlling parameter.

*Most of the preliminary work reported in this section was done with the inestimable help of my Bachelor students: Carlos Vivanco Silva, Alicia González Gala, Alexis Jesús Lora de la Calle, Omar Otero Santos and Oscar Luis Muñoz.

Regarding analytical studies, we still need to keep working on self-excited thermoacoustics, following the research line opened by Wu and Law [27, 28]. Furthermore, the validity of the Markstein number should be revisited and extended using less restrictive assumptions (*e.g.*, $Le \neq 1$, finite β).

Experiments

A considerable amount of experiments are still to be done. We were able to open some of the potential research lines of the future with regard experimental thermoacoustics, providing preliminary results on the following items:

- Nitrogen dilution.

The influence of diluting $\phi = 0.8$ and $\phi = 1.1$ propane-air flames with different amounts of pure nitrogen was checked [32] (Fig. 4.3). The dilution was performed by adding a second mixer to the injection line, where the inert species was added to the mixture. The presence of nitrogen has a non negligible effect on the flames. It reduces the adiabatic temperature and the laminar propagation speed of the flames by around a 15% for the maximum dilution considered here ($Y_{N_2} = 0.22$). However, it does not modify the diffusive properties, keeping the Lewis number almost constant.

The results depicted in Fig. 4.3 show a variation on the flame dynamics, more specifically on the strength of the flame-acoustics coupling. The maximum velocities recorded decrease by a 50% or more, producing also a reduction of the length of the characteristics fingers of the secondary acoustic instability. Additionally, the oscillation frequency is lower, which can be directly related to the decrease of the flame temperature. However, the analyzed flames kept vibrating in the thermoacoustic instability regime of the non-diluted flame with the same equivalence ratio. Due to this reduction of the oscillatory velocities, one would expect the transition threshold ($\phi_c = 0.87 \pm 0.05$ without dilution) to be slightly modified, avoiding the onset of secondary instabilities (or even eluding the appearance of acoustic-related phenomena) for determined mixtures.

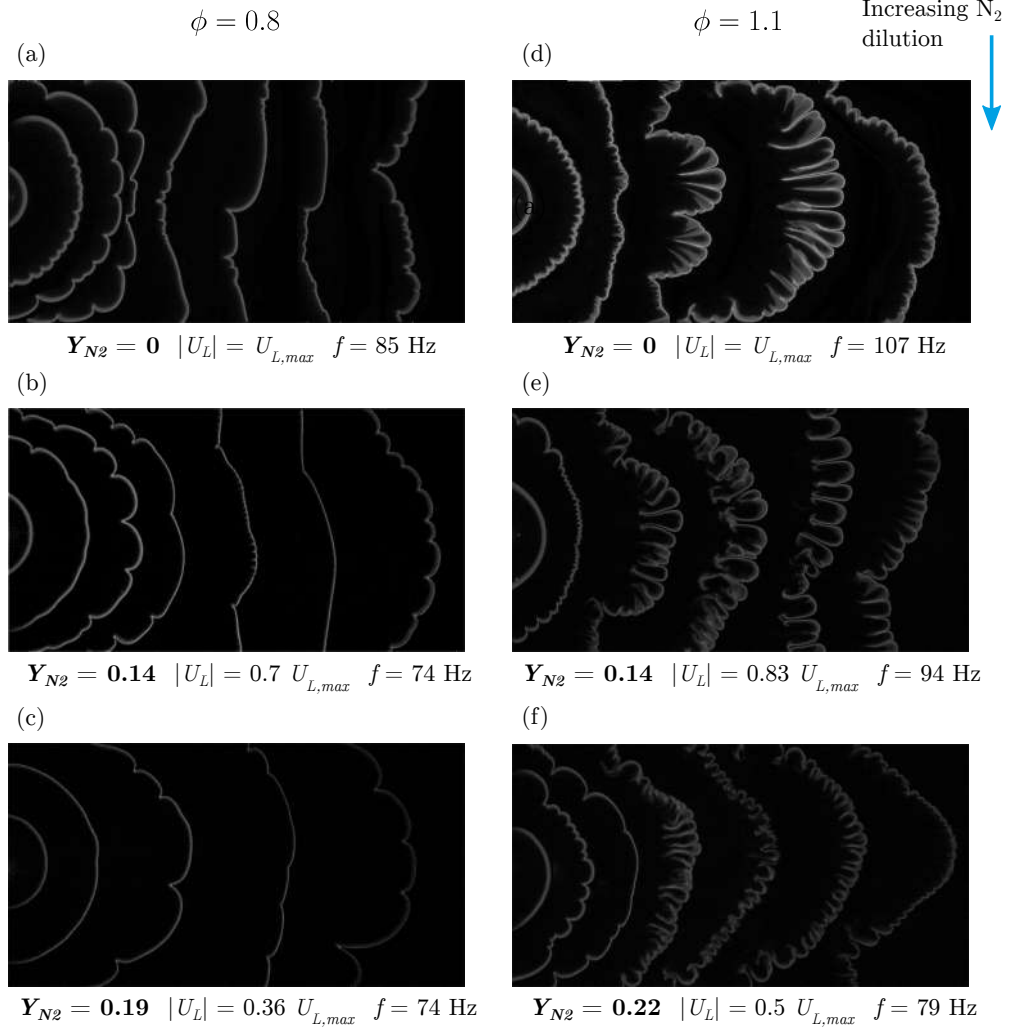


FIGURE 4.3 | Effect of nitrogen dilution on the appearance and strength of acoustic-related oscillations of lean and rich propane flames.

- Adding helium to the burned mixtures.

Stoichiometric methane flames were diluted with small amounts of helium, up to $Y_{He} = 0.052$ [33]. Adding helium, on the contrary to nitrogen, does significantly modify the diffusive properties of the mixture, moving from $Le = 1$ without dilution up to $Le = 1.65$ for the highest dilution. Furthermore, it also reduces the adiabatic

flame temperatures of the affected blends by a 14% approximately. Please note that the modifications of the combustion chamber introduced in chapter 3 and [34] were already introduced, modifying the quantitative results when compared to those given in chapter 2 for horizontal flames [35, 36].

Surprising flame behaviours were observed as shown in Fig. 4.4, considering the tiny amounts of dilutant used. (a) depicts a non-diluted and non-buoyant stoichiometric methane flame –the equivalence ratio is constant hereafter– propagating in a $h = 10$ mm channel, showing strong secondary acoustic oscillation with $p_{max} = 8$ kPa. When only a 3% in mass of He is present in the mixture (b), the oscillation is much weaker ($p_{max} = 2.5$ kPa) and the frequency also decreases. Further dilution ((c), 4%) does not allow the flame to transition to the secondary acoustic instability regime, becoming nearly planar and oscillating smoothly until the flame reaches the closed end of the channel. When at around 5% of helium in mass –(d) and (e)–, the oscillatory motion vanishes and the almost unwrinkled flame begins to quench from the lateral tips of the front to the center. Adding more helium inhibits the flame to even ignite.

This unexpected major influence of helium on the flame propagation claims to be analyzed in detail. It introduces himself as a potential inhibitor of thermoacoustic instabilities for practical applications.

- How does the structure stiffness modify thermoacoustics?

We found a very important influence of the interaction between the fluid and the holding structure on the appearance of thermoacoustic instabilities [37, 38], also reported in [39]. Again, consider the structural modifications introduced to the experimental rig, impeding a direct quantitative comparison with the results reported in chapter 2.

Given a constant stoichiometric propane-air mixture, the top cover of the Hele-Shaw combustion chamber was replaced. We use for this experiments metacrilate (PMMA) plates and progressively reduce its thickness h_w from 25 to 5 mm. The stiffness of the changing component of the structure is

$$D = \frac{E_Y h_w^3}{12(1 - \nu_P^2)}, \quad (4.3)$$

with $E_Y = 3.3$ GPa the Young modulus and $\nu_P = 0.45$ the Poisson coefficient of the

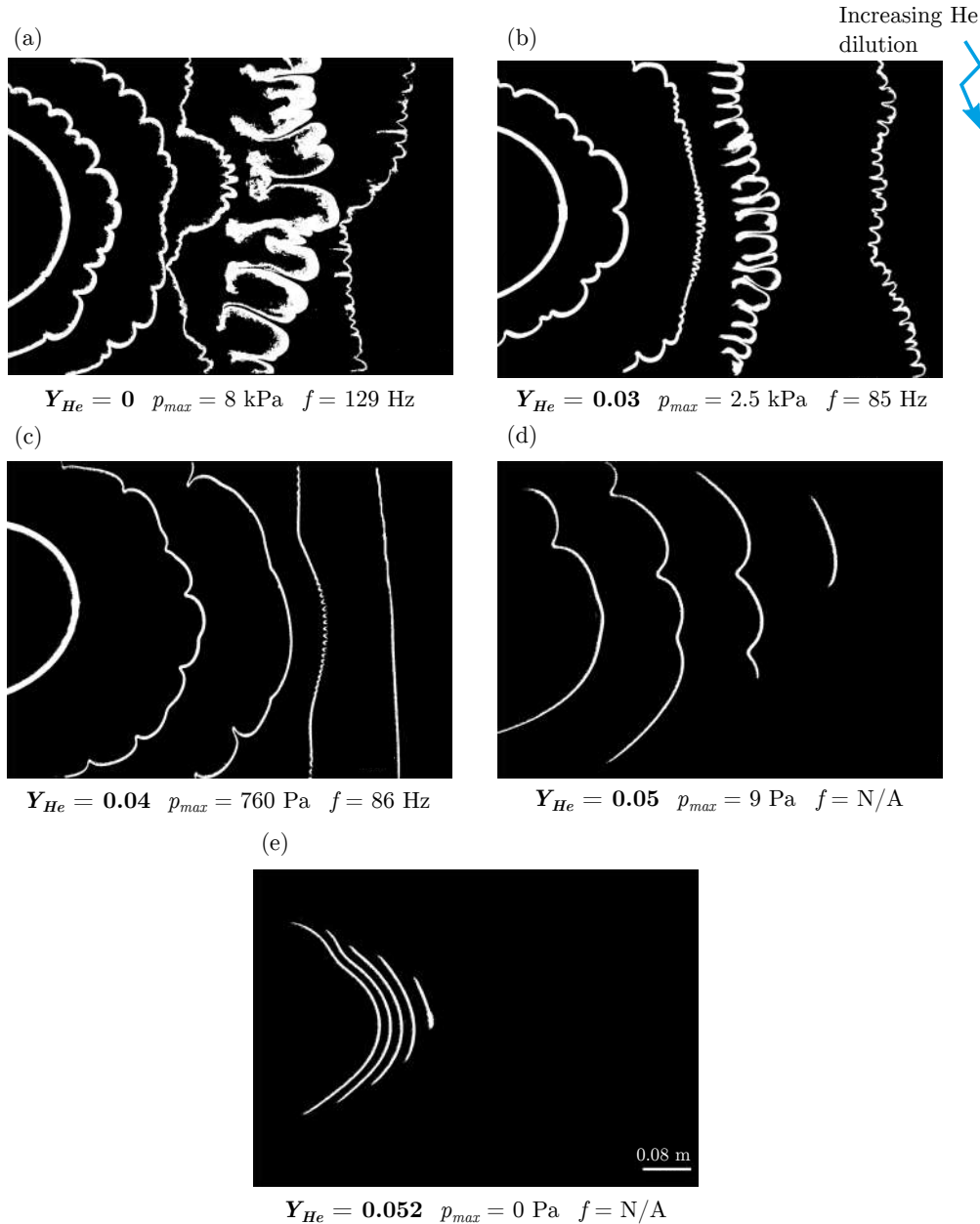


FIGURE 4.4 | Effect of helium dilution on the propagation of stoichiometric methane flames. Binary images are shown here for clarity.

PMMA [40].

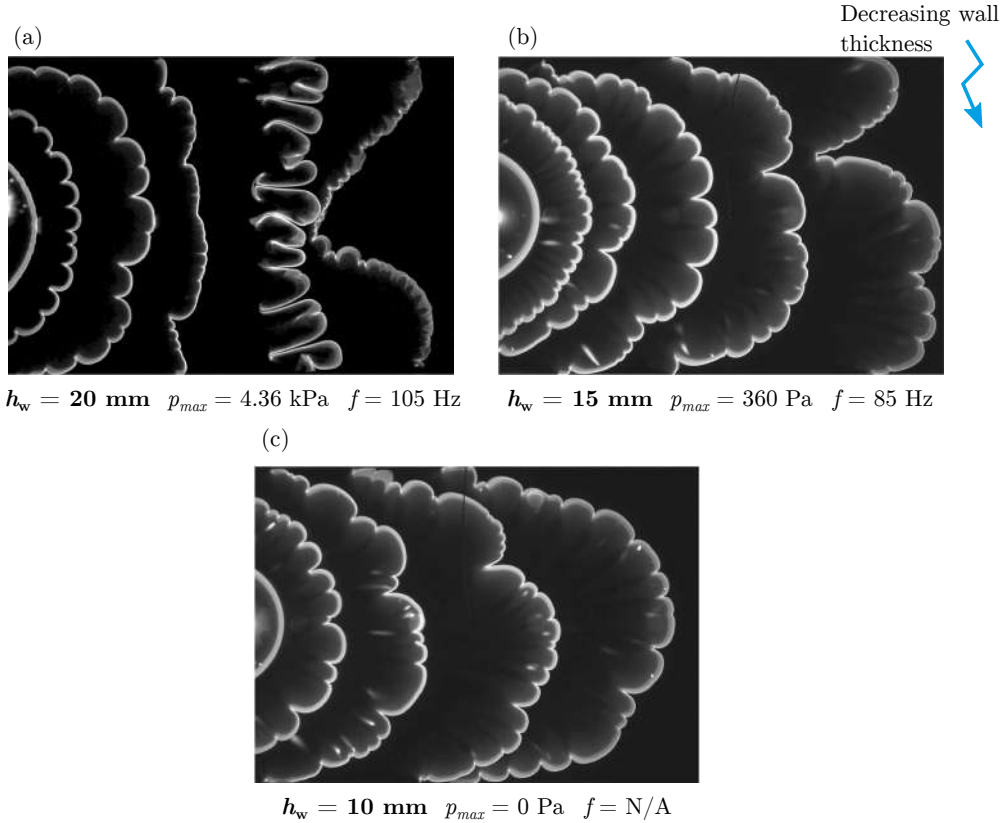


FIGURE 4.5 | Influence of the structure stiffness on the onset of thermoacoustic instabilities.

Figure 4.5 shows three representative propagating flame-fronts in different combustion chambers. The base case (a), built with a top cover of thickness $h_w = 20 \text{ mm}$, shows a flame propagating under the secondary thermoacoustic regime, undergoing acoustic pressures of amplitude $p_{max} = 4.36 \text{ kPa}$ and frequencies $f = 105 \text{ Hz}$. When the thickness of the top cover is reduced to $h_w = 15 \text{ mm}$, (b), the flame stays in the primary regime, suffering smooth oscillations of around 360 Pa and frequencies of 90 Hz. The behaviour is similar to that of a leaner flame traveling in a combustion chamber with a thicker, thus stiffer, top plate. Further reduction of the cover thickness (c) avoids the appearance of any feedback between the reaction front and the acoustic waves, being these completely damped.

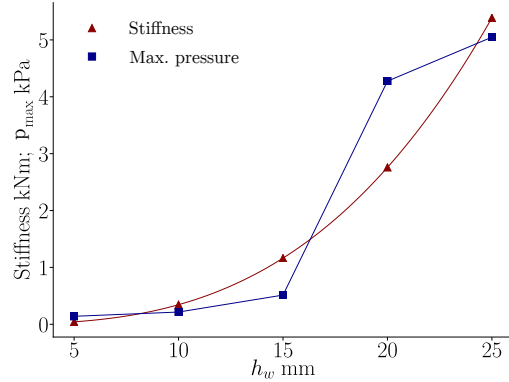


FIGURE 4.6 | Stiffness of the top cover with different thickness and acoustic pressure amplitude obtained with a stoichiometric propane flame.

We found a direct relation between the structure stiffness and the onset of thermoacoustics (Fig. 4.6), being able to even totally avoid them. Our first hypothesis is that the top cover acts as a damper when it becomes elastic enough and soothe the pressure waves that can appear at the combustion chamber, preventing their interaction with the flame. Additional extensive work is required to comprehend this finding, which can be interesting due to its direct practical application and high capacity to control the vibrating and dangerous instability.

- Hydrogen oscillatory regime not related to acoustics.

Downward-propagating hydrogen flames under the effect of thermoacoustic instabilities were only found for very lean flames. To find the limits, we extended the mixture composition of the studied flames up to $\phi \sim 3.4$ and reduced the channel thickness from 10 to 1 mm. The resulting stability map is shown in Fig. 4.7. Most of the regions were previously known, as those for very rich flames (only DL instability) or thin channels (DL and TD are found), or will be analyzed in the second part of this dissertation (chapters 5 and 6 [30, 31]). However, the highlighted region in dark red marks out the $h - \phi$ area where the flames propagate with an unexplained and particular behaviour.

The stoichiometric flame shown in Fig. 4.8 (a) travels along a 8-mm channel and oscillates provoking strong inner pressures of 6.5 kPa (twice those found for acoustics). The influence of acoustics is mostly discarded as it is not the second acoustic mode of the

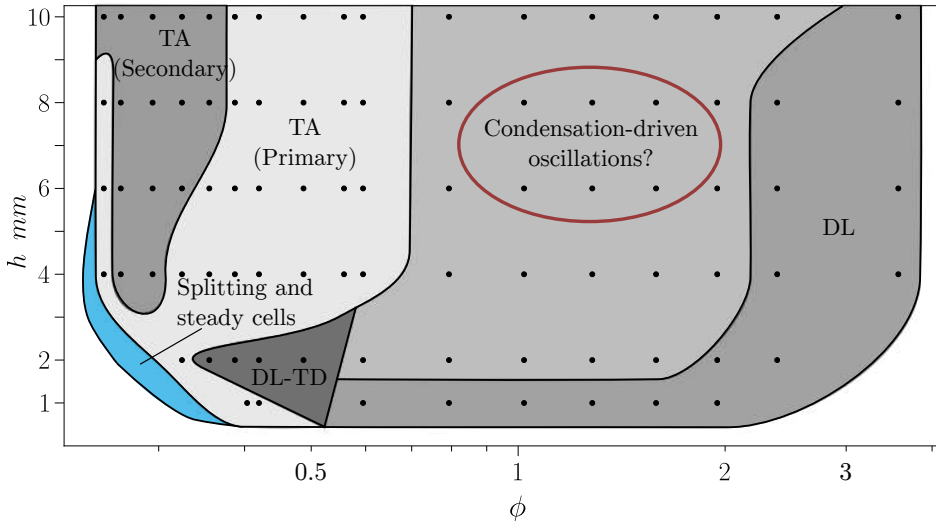


FIGURE 4.7 | Preliminary stability map of hydrogen-air flames propagating downwards in narrow channels. The red circle defines the unknown region to be studied and the cyan region covers the stability area to be analyzed in the second part of this dissertation.

chamber, presenting not a precise peak but a wide band of frequencies when vibrating. Furthermore, the flame shape is very smooth with just some cells probably related to the DL instability, showing no characteristic lobes of thermoacoustics (Fig. 4.8 (b)). One interesting feature recurrently found is the presence of a discontinuous path left by the flames, which could be related to condensation cycles. However, the reason behind this oscillatory regime is still not clear and requires additional work to be understood.

On top of the aforementioned problems, there are other parameters which also need to be assessed, regions to be determined, as well as modifications and improvements of the experimental setups used during this thesis. The main ideas and variations are enlisted here:

- The experimental setup used for the combustion of hydrocarbon-air mixtures can be improved to obtain additional data helpful to solve the thermoacoustics problem. For the sake of conciseness, we give here only a few examples. It would be interesting to measure the outflow velocity, the mixture composition, the temperature of the gases, etc. Also, the ignition system should be updated, ideally obtaining an in-line ignition or

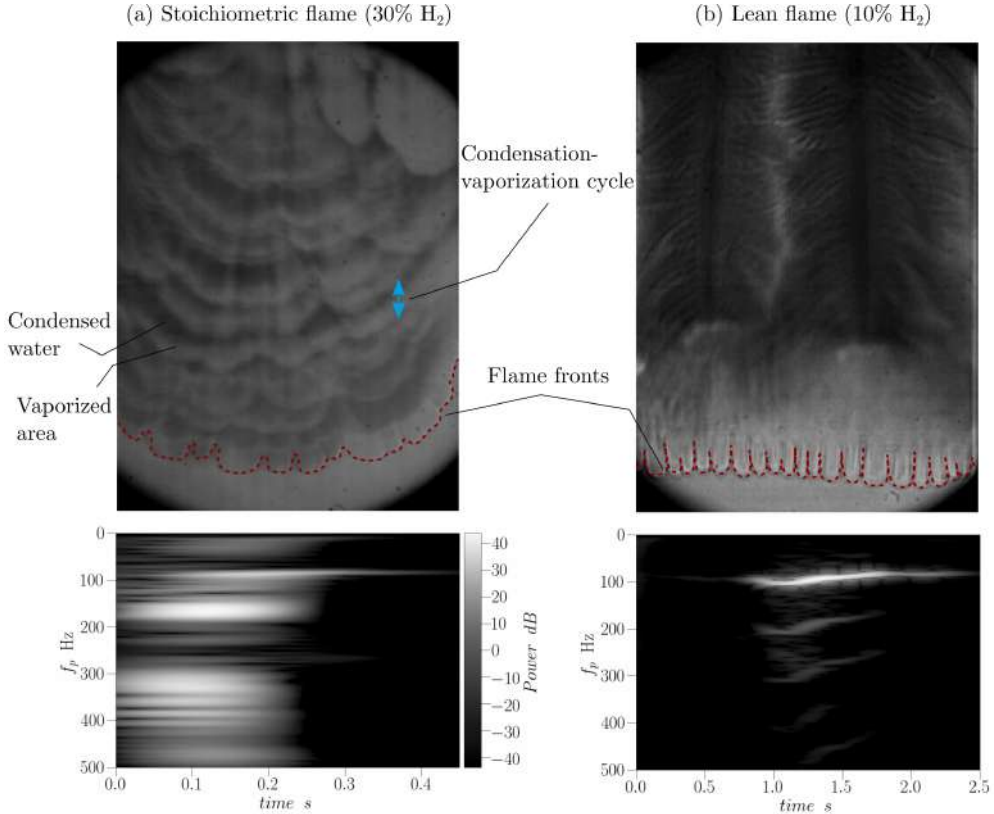


FIGURE 4.8 | (a) Stoichiometric and (b) lean hydrogen flames propagating in a $h = 8$ mm channel. The cyan arrow indicates one possible condensation-vaporization cycle that always appear in the new region. Additionally, the spectrograms at the bottom of the figure represent the dominant frequency of the recorded pressure waves within the chamber.

activating the reaction via a spark plug. The latter problem becomes critical for vertical propagation test.

- The effect of buoyancy was only assessed for thick channels. We can modify h to check if it has an interesting effect on the propagation of the flames.
- Study in a more detailed way upward-propagating hydrogen flames for different channels gaps.
- Analyze non-buoyant hydrogen-air blends, which requires major modifications of the experimental rig at KIT (*i.e.*, vertical Schlieren system).

- Improve the visualization of the hydrogen flames by modifying the optics or using OH filters to capture the OH* emissions of the invisible –to the naked eye– flame-front.

References

- [1] J. De Vries, W. B. Lowry, Z. Serinyel, H. J. Curran, E. L. Petersen, Laminar flame speed measurements of dimethyl ether in air at pressures up to 10 atm, *Fuel* 90 (331–338) (2011).
- [2] S. Davis, J. Quinard, G. Searby, Markstein publishers in counterflow, methane-and propane-air flames: a computational study, *Combustion and Flame* 130 (123–136) (2002).
- [3] E. Al Sarraf, C. Almarcha, J. Quinard, B. Radisson, B. Denet, P. Garcia-Ybarra, Darrieus–Landau instability and Markstein publishers of premixed flames in a Hele-Shaw cell, *Proceedings of the Combustion Institute* 37 (1783–1789) (2019).
- [4] G. Searby, J. Quinard, Direct and indirect measurements of markstein publishers of premixed flames, *Combustion and Flame* 82 (298–311) (1990).
- [5] J.-M. Truffaut, G. Searby, Experimental study of the darrieus-landau instability on an inverted-'v'flame, and measurement of the markstein publisher, *Combustion science and technology* 149 (35–52) (1999).
- [6] C. Clanet, G. Searby, First experimental study of the darrieus-landau instability, *Physical review letters* 80 (3867) (1998).
- [7] J. Bechtold, M. Matalon, The dependence of the markstein length on stoichiometry, *Combustion and flame* 127 (1906–1913) (2001).
- [8] P. Clavin, P. Garcia, The influence of the temperature dependence of diffusivities on the dynamics, *Journal de Mécanique Théorique et Appliquée* 2 (245–263) (1983).
- [9] M. Matalon, C. Cui, J. Bechtold, Hydrodynamic theory of premixed flames: effects of stoichiometry, variable transport coefficients and arbitrary reaction orders, *Journal of fluid mechanics* 487 (179–210) (2003).
- [10] R. C. Aldredge, N. Killingsworth, Experimental evaluation of markstein-publisher influence on thermoacoustic instability, *Combustion and flame* 137 (178–197) (2004).
- [11] J. Bechtold, M. Matalon, The dependence of the markstein length on stoichiometry, *Combustion and Flame* 127 (1906–1913) (2001).

- [12] J. Yanez, M. Kuznetsov, J. Grune, Flame instability of lean hydrogen–air mixtures in a smooth open-ended vertical channel, *Combustion and Flame* 162 (2830–2839) (2015).
- [13] M. Matalon, P. Metzner, The propagation of premixed flames in closed tubes, *Journal of Fluid Mechanics* 336 (331–350) (1997).
- [14] A. Patyal, M. Matalon, Nonlinear development of hydrodynamically-unstable flames in three-dimensional laminar flows, *Combustion and Flame* 195 (128–139) (2018).
- [15] K. Aung, M. Hassan, G. Faeth, Markstein publishers and unstretched laminar burning velocities of hydrogen-air flames, *Proceedings of the 33rd Aerospace Sciences Meeting and Exhibit* (374) (1995).
- [16] G. H. Markstein, Experimental and theoretical studies of flame-front stability, *Journal of the Aeronautical Sciences* 18 (199–209) (1951).
- [17] W. Eckhaus, Theory of flame-front stability, *Journal of Fluid Mechanics* 10 (80–100) (1961).
- [18] G. Markstein, Non-steady flame propagation, AGARDograph, Pergamon, New York 75 (1964).
- [19] P. Clavin, G. Joulin, Premixed flames in large scale and high intensity turbulent flow, *Journal de Physique Lettres* 44 (1–12) (1983).
- [20] P. Clavin, F. Williams, Effects of molecular diffusion and of thermal expansion on the structure and dynamics of premixed flames in turbulent flows of large scale and low intensity, *Journal of fluid mechanics* 116 (251–282) (1982).
- [21] P. Pelce, P. Clavin, Influence of hydrodynamics and diffusion upon the stability limits of laminar premixed flames, *Journal of Fluid Mechanics* 124 (219–237) (1982).
- [22] M. Matalon, B. J. Matkowsky, Flames as gasdynamic discontinuities, *Journal of Fluid Mechanics* 124 (239–259) (1982).
- [23] G. H. Markstein, Instability phenomena in combustion waves, *Proceedings of the International Symposium on Combustion* 4 (44–59) (1953).

- [24] G. Markstein, W. Squire, On the stability of a plane flame front in oscillating flow, *The Journal of the Acoustical Society of America* 27 (416–424) (1955).
- [25] G. Searby, D. Rochwerger, A parametric acoustic instability in premixed flames, *Journal of Fluid Mechanics* 231 (529–543) (1991).
- [26] J. Yáñez, M. Kuznetsov, R. Redlinger, The acoustic-parametric instability for hydrogen-air mixtures, *Combustion and Flame* 160 (2009–2016) (2013).
- [27] X. Wu, C. K. Law, Flame-acoustic resonance initiated by vortical disturbances, *Journal of fluid mechanics* 634 (321–357) (2009).
- [28] R. C. Assier, X. Wu, Linear and weakly nonlinear instability of a premixed curved flame under the influence of its spontaneous acoustic field, *Journal of Fluid Mechanics* 758 (180–220) (2014).
- [29] P. Clavin, Dynamic behavior of premixed flame fronts in laminar and turbulent flows, *Progress in energy and combustion science* 11 (1–59) (1985).
- [30] D. Martínez-Ruiz, F. Veiga-López, D. Fernández-Galisteo, V. N. Kurdyumov, M. Sánchez-Sanz, The role of conductive heat losses on the formation of isolated flame cells in hele-shaw chambers, *Combustion and Flame* 209 (187–199) (2019).
- [31] F. Veiga-López, M. Kuznetsov, D. Martínez-Ruiz, E. Fernández-Tarrazo, J. Grune, M. Sánchez-Sanz, Unexpected propagation of ultra-lean hydrogen flames in narrow gaps, *Physical Review Letters* (2020).
- [32] A. Gonzalez-Gala, Experimental study of the effect of the dilution of the propane with nitrogen in a hele-shaw cell, *Trabajo fin de Grado* (2019).
- [33] O. Otero-Santos, Estudio experimental de llamas de premezcla de metano con dilución de helio en una celda hele-shaw, *Trabajo fin de Grado* (2019).
- [34] A. Lora-de-la Calle, Automatization of a flame propagation experimental setup using labview, *Trabajo fin de Grado* (2019).
- [35] F. Veiga-López, D. Martínez-Ruiz, E. Fernández-Tarrazo, M. Sánchez-Sanz, Experimental analysis of oscillatory premixed flames in a hele-shaw cell propagating towards a closed end, *Combustion and Flame* 201 (1–11) (2019).

- [36] D. Martínez-Ruiz, F. Veiga-López, M. Sánchez-Sanz, Premixed-flame oscillations in narrow channels, *Physical Review Fluids* 4 (100503) (2019).
- [37] D. Martinez-Ruiz, F. Veiga-Lopez, M. Sanchez-Sanz, Vessel confinement contributions to thermo-acoustic instabilities of premixed flames, *Bulletin of the American Physical Society* 63 (2018).
- [38] O. Luis-Munoz, Analisis experimental de llamas de premezcla en una celda hele-shaw, Trabajo fin de Grado (2019).
- [39] B. Radisson, J. Piketty-Moine, C. Almarcha, Coupling of vibro-acoustic waves with premixed flame, *Physical Review Fluids* 4 (121201) (2019).
- [40] C. A. Harper, E. M. Petrie, *Plastics materials and processes: a concise encyclopedia*, John Wiley & Sons, 2003 (2003).

Part II

Near-limit combustion of hydrogen

"En todas las cosas de la naturaleza hay algo maravilloso"

– Aristóteles

Opening remarks

The previous part of the thesis analyzed how the combination of different parameters may trigger thermoacoustic instabilities in narrow channels. As we experimentally showed in Part I, one of the interesting conclusions is that acoustic-flame interactions are less important, and eventually disappear, when the relative importance of heat losses grows (see Fig. 4.7) either because the flames propagate in sufficiently narrow channels or because the fuel concentration is closed to the lower flammability limit. Taking advantage of this, we eliminate the acoustic out of the problem in the second part of the thesis and focus on flames governed by other phenomena, such as heat losses or fuel diffusivity. From a theoretical point of view, this limit can be achieved by reducing to zero the channel thickness as will be shown below in chapter 5. Experimentally, this assumption implies a strong increment of the relative importance of heat losses that can be induced by reducing the gap distance between the solid walls, reaching thicknesses down to 1 mm, or reducing the heat released by the flame. These two alternatives were tested in chapter 6 using hydrogen as fuel.

The theoretical-numerical analysis carried out in chapter 5 takes advantage of the limit of very narrow channels to simplify the formulation of the problem down to a quasi-2D approach which also includes the influence of heat losses to its surroundings. These simulations predicted two unreported propagation mechanisms for ultra-lean hydrogen flames. According to the calculations, for sufficiently large heat losses, the flame quenched locally and the remaining reactive front split into several flame cells that propagated in almost straight lines or divided continuously following a fractal-like path.

The experiments carried out in chapter 6, burning hydrogen in HS cells with thicknesses of the order of millimeters, provided empirical evidence of the existence of the two

propagation mechanisms predicted numerically in chapter 5. The combination of numerical and experimental techniques highlighted heat losses and fuel mass difussivity as the physical mechanisms explaining the flame behaviour. Finally, in chapter 7 we collect all the conclusions and propose new research lines regarding the combustion of hydrogen at such extreme conditions.

CHAPTER 5

Numerical analysis of the propagation of highly-diffusive flames in a quasi-2D non-adiabatic geometry

Hydrogen is one of the preferred alternative fuel options to produce energy, as presented in chapter 1 and 3, either in fuel cells or in combustion systems. In comparison to conventional hydrocarbons, some of the main concerns of power generation technologies based on hydrogen are the potential safety issues associated to its use [1–3]. The small size of the H₂ molecule brings along a higher permeation of the fuel through solid walls, especially in non-metallic containers [4], that significantly increases the risk of undesired leaks [5]. Additionally, its high reactivity, with a lean-flammability limit around %H₂ = 4 at Earth’s gravity [3, 6], and ignition energy as low as 0.02 mJ, ten times lower than conventional hydrocarbons [7, 8], makes hydrogen more prone to undesired deflagrations and explosions when leaks take place in reduced spaces without ventilation [9]. Furthermore, the dim visible emissions and weak heat radiated from lean hydrogen flames make their detection extremely difficult [10]. The potential use of hydrogen in technological applications [11] and its inherent scientific interest [12, 13] has attracted the attention of different research groups during decades, with theoretical, experimental and computational studies that cover the whole range of fuel concentrations. Nevertheless, in this chapter we dig into the unexplored effect of heat losses in ultra lean hydrogen mixtures in which the high diffusivity of hydrogen plays a fundamental role to extend the flammability limit of isolated comet-like flames within which the temperature is barely above the cross over temperature.

Safety-related issues, such as fuel leakage, undesired ignition or explosion accidents, have motivated new fundamental studies. Besides the most destructive events, such as detonations and material combustion, one of the main challenges when using hydrogen is to detect and control very lean and slow-burning flames that can deliver undesired hot spots into flammable regions. These reactive kernels can travel in favor or against gravity under different circumstances. The description of this variety of new regimes in confined lean-burning processes is imperative to design updated prevention strategies, in particular for hydrogen-based systems.

Unconfined studies from Droznov and Zel'dovich in 1943 [14] and Zel'dovich in 1944 [15], predicted in their theories the existence of isolated non-propagating flame balls in a quiescent atmosphere, which were confirmed later by Ronney in microgravity experiments [16]. Following the suggestions made by Zel'dovich, Buckmaster et al. [17–19] demonstrated that flame balls can be stabilized when radiation heat losses offset the excess of heat accumulated close to the reaction area. Later, Grcar [20] found a stable solution in a non-buoyant numerical study in which the flames travel at constant velocity adopting hemispherical shapes and in the absence of radiative losses. Recently, under standard gravity conditions, Zhou et al. [21] found experimentally a combustion regime characterized by the combustion of hydrogen forming an array of unstable flame balls.

5.1 Quasi-2D considerations

The analytical solutions proposed by [17–19] are valid for spherical flame balls. However, it is not possible to obtain a physically-acceptable mathematical solution for a steady two-dimensional circular flame. To prove this point, first consider a planar quiescent reactive-diffusive system in which the fuel is consumed in a circular flame front to release an amount of heat Q . The corresponding conservation equations for energy and deficient species Y_{def} written in radial cylindrical coordinates yield

$$\frac{1}{r} \frac{d}{dr} \left(r k_g \frac{dT}{dr} \right) + Q\Omega - \hat{b} = 0, \quad \frac{1}{r} \frac{d}{dr} \left(r\rho D_i \frac{dY_{def}}{dr} \right) - \Omega = 0, \quad (5.1)$$

being T the gas temperature, ρ the gas density, k_g the thermal conductivity, D_i the species diffusivity, Ω the reaction rate and \hat{b} a generic heat-loss function. Given that the flame surface is at $r = r_f$, the system of equations (5.1) must be integrated with boundary conditions $T - T_b = Y = 0$ at $r = r_f$ and $T - T_u = Y - 1 = 0$ at $r \rightarrow \infty$, with T_u and T_b the temperature of the unburned and burnt gases respectively. Out of the thin flame surface $r \rightarrow \infty$, the reaction vanishes $\Omega = 0$ and both equations can be easily integrated. Once the heat-loss function $\hat{b} > 0$ is known, we can easily integrate the first equation in (5.1) to obtain a temperature profile that decays smoothly towards T_u . However, regardless of \hat{b} , the mass fraction profile is always of the form $Y = C_1 \ln r + C_2$, with C_1 and C_2 representing the integration constants whose value cannot be chosen to simultaneously satisfy the boundary conditions both at $r \rightarrow \infty$ and $r = r_f$.

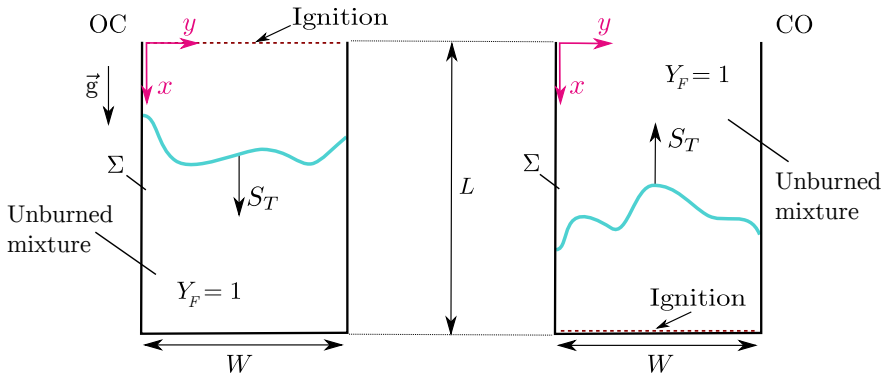


FIGURE 5.1 | Sketch of the Hele-Shaw chamber of dimensions $L \times W$ in the open-closed OC (left) and closed-open CO (right) configurations, where \vec{g} is the general gravity acceleration vector and S_T the overall flame propagation velocity.

In spite of this analytical discussion and encouraged by the results of Grcar [20], we use a quasi-2D methodology to simulate a narrow channel geometry (*i.e.* HS cell) and explore the practicability of stable comet and circle-like traveling flames in low-Lewis number reactive mixtures, such as lean hydrogen-air blends. We predict non-static kernels numerically using a quasi-2D computational domain, sketched in Fig. 5.1 for two different configurations: flames propagating from an open towards a closed end and *vice versa*.

In the limit where the separation between plates is asymptotically small compared to any other length scale of the problem (*i.e.* $h \ll W; L; \delta_T$, hence, we recall that $a = h/\delta_T$ is a small parameter in this case), the dynamics of the flame can be studied using a quasi-2D

formulation that preserves the physics of the process and keeps the computational cost within limits [22]. In the limit of very narrow channels $a \ll 1$, the transverse gradients in z direction of pressure, temperature and mass fraction can be neglected in the first approximation, with the viscous-dominated velocity adopting a Poiseuille parabolic profile that relates to x and y pressure gradients by means of Darcy-like expressions (Eq. 5.23). The contribution of acoustic pressure changes naturally disappears from both the state and energy equations in the double limit $a \ll 1$ and $M/a \ll 1$ imposed in this chapter.

Initially, the volume between the plates $\Sigma = V_{tot}$ is filled with unburned reactants, which are progressively consumed after ignition (at time $t = 0$). The side walls of the chamber are always kept closed. Depending on the studied boundary conditions, the ignition or the opposite-to-ignition end is configured as a venting section. Partial confinement is responsible for the first order dynamics of the flame, but conductive heat losses have been found to be critical in the flame morphology. We show here how non-adiabatic plates favor the transition from a continuous front to a set of isolated flame cells. The dynamics of these flame cells are explored here in terms of the different parameters involved in the problem.

The chapter is structured as follows: in section 5.2 and 5.3 we summarize the results obtained for non-buoyant and buoyant flames with the numerical method and quasi-2D formulation explained in Appendix 5.A. The discussion includes the effect of heat losses in several HS configurations with and without the effect of gravity. Details and further discussion regarding the shape of circular and comet-like flames stabilized by wall heat losses are shown in section 5.4.

5.2 Heat-loss effect in non-buoyant flames

This section explores the effects of increasing conductive heat losses at the channel walls on the propagation of highly diffusive fuel flames and the transition from a continuous front into a set of isolated circle or comet-like flames. The dimensionless heat-loss parameter is defined as,

$$b = \frac{2hk_w}{a^2 h_w k_u}, \quad (5.2)$$

with h and h_w the respective thickness of the channel and the walls, k_w and k_u the thermal conductivity of the solid walls and the mixture at room temperature respectively. In order to isolate other physical contributions, we first consider premixed flames not affected by gravity

($\alpha = 0$ and, therefore, $G = g \sin(\alpha) \delta_T a^2 / S_L^2$). Different ignition locations are proposed, at the open or closed ends, to respectively account for the pressure effect of confined fresh or burnt gases on the stabilization of the circle and comet-like flame regimes. It can be directly observed that the flame front is rapidly wrinkled in all cases due to Darrieus-Landau (density change through the front) and thermodiffusive (low-Lewis number) instabilities. An equidiffusional case ($Le = 1$) is also considered to verify that the isolated weak cells are exclusive to highly-diffusive mixtures.

5.2.1 Open-closed (OC) propagation

Premixed flames advancing towards a closed end produce a confinement effect on the fresh reactants that progressively rises the pressure ahead of the flame front. Here, the temperature profile is initialized using a sinusoidal perturbation at $x_0 = 0.01L$ (Eq. 5.31) that is naturally amplified during the initial time steps. The results for increasing values of b are shown in Fig. 5.2. Coloured isocontours show the non-dimensional temperature distribution $\theta = (T - T_u) / (T_b - T_u)$ and the arrows represent the flow field at the last dimensionless time instant $t' = t / (\delta_T / S_L)$ shown in each case (*i.e.* $t' = 4.5$ for $b = 0$, $t' = 5.0$ for $b = 0.5$, $t' = 5.0$ for $b = 0.75$ and $t' = 6.5$ for $b = 1$). Likewise, light solid lines represent the reaction rate isocontours Ω' (Eq. 5.15) for intermediate times to generate a visual representation of the evolution of the flame front. From now on, all the dimensional variables in this chapter, if applicable, are written without their superscript ' for clarity. Please, refer to Appendix 5.A for further information regarding the definition of the variables.

In the absence of heat losses ($b = 0$), the flame acquires the classical cellular structure induced by the thermodiffusive instabilities with an overall flame front that propagates along the chamber. Well-defined cells grow together in amplitude and divide the front by extinction of the receding troughs, as observed previously in [23]. At those points, fresh reactants crossing the flame towards the high-temperature region of the domain can be found, generating localized tails of lower temperature. In addition, the cellular instability generates a rapid loss of the y -axis symmetry that unbalances the pressure build-up in the confined region. Transverse pressure gradients provoke a lateral motion of the fresh mixture and generate a preferential venting corridor on one side of the chamber that makes possible the leakage of unburned reactants through the open end out of the computational domain. Additionally, the higher the heat-loss

parameter the lower the maximum temperatures reached in the domain, thus reducing the mean propagation velocity. Thus the size of the venting channel becomes bigger with b , as the flame becomes weaker and more easily blown backwards by the self induced over-pressure.

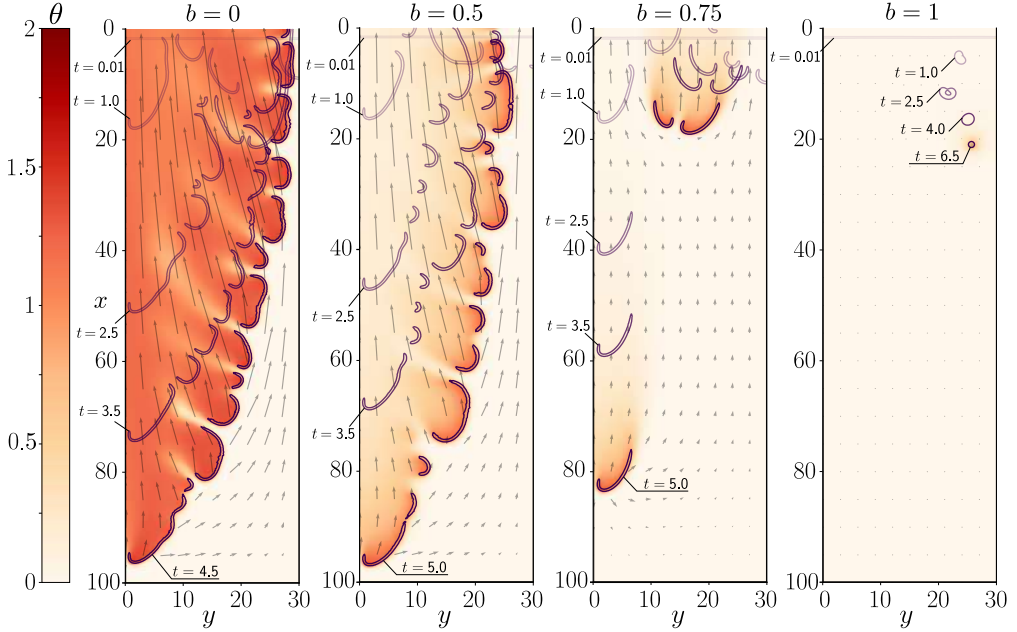


FIGURE 5.2 | Flame front evolution in non-buoyant OC propagation at different times for increasing values of the heat-loss parameter b . The color map represents the non-dimensional temperature profile. The arrow field shows the flow direction and intensity, both at the last instant depicted in each panel.

The cellular character of the flame is promoted by the division of the front at the extinguished cusps when the heat losses parameter is higher. For $b = 0.5$ in Fig. 5.2 we can observe an increase of the number of cells separated from each other by cold reactants. Further increase of the heat losses ($b = 0.75$), induces the formation of elongated comet-like flame structures, somehow similar to the propagating hemispherical flames found by Grcar [20] in his adiabatic 2D calculations and by Kagan et al. [24] in their non-adiabatic 3D simulations. Here, the fronts are stabilized by the combined effects of the surrounding convective flow, high diffusion of unburned species behind the flame tails and conductive heat losses to the walls. As shown later in Fig. 5.4, only half of the fuel is burned before the flame reaches the end of the domain. Finally, a case with $b = 1$ fails to propagate, reaching short distances from the ignition end of

$20\delta_T$ in times as long as $t \simeq 6.5$. Due to the larger value of b , the flame is extinguished before reaching the end of the domain leaving almost 90% of the fuel unburned.

5.2.2 Closed-open (CO) propagation

Premixed flames ignited at the closed end, $x_0 = 0.99L$, produce a stabilizing over-pressure behind the flame front. It can be noted that the burned gases trapped between the flame and the end wall act as a volume source, pushing the reaction region towards the venting end and shortening the burning time. The CO propagation cases in absence of gravity are shown in the panels of Fig. 5.3. Again, the colored isocontours of temperature are shown from left to right at the last time ($t = 1.0$ for $b = 0$, $t = 1.0$ for $b = 0.5$, $t = 2.63$ for $b = 1$, and $t = 6.98$ for $b = 1.25$) including dim reaction rate isocontours in previous time steps to illustrate the evolution of the flame in each case.

The adiabatic case ($b = 0$) shows a high degree of symmetry in the y direction during its whole propagation, in contrast with the analogous OC configuration. Moreover, the absence of heat losses yields an important temperature accumulation produced by the burned gases and the pressure build-up at the closed end. For this reason, more extreme flow velocities are induced in comparison to the OC case, while preserving the cell characteristic size. Allowing heat losses through the walls ($b = 0.5$) the flame breaks by means of enhanced local extinction, reducing the characteristic cell size and promoting disorder of the front. For $b = 1$, the unstable fragmented flame front evolves to produce isolated flame cells. These circle-like structures arise after traversing half of the domain and interact between them. Later, a stable and symmetrical two-headed cell is developed, which travels steadily towards the end of the chamber. These kind of coupled cells arise naturally for other values of $b \sim O(1)$. Furthermore, isolated circle-like flames are found for $b = 1.25$. These tiny flame cells produce moderate increases of temperature and very low reaction rates. Therefore, small variations are found in the flow field during their propagation. They exhibit a steady behavior remaining active for large periods of time. Finally, these circle-like flames are extinguished when heat losses are large enough to overcome the heat released by the reaction. In conclusion, isolated cells are more easily restrained and extinguished when acting against the build up of pressure in fresh gases (OC). As expected, a more stable behavior is found for propagation towards an open end where the endurance of weak kernels benefits from piston-like effects (CO).

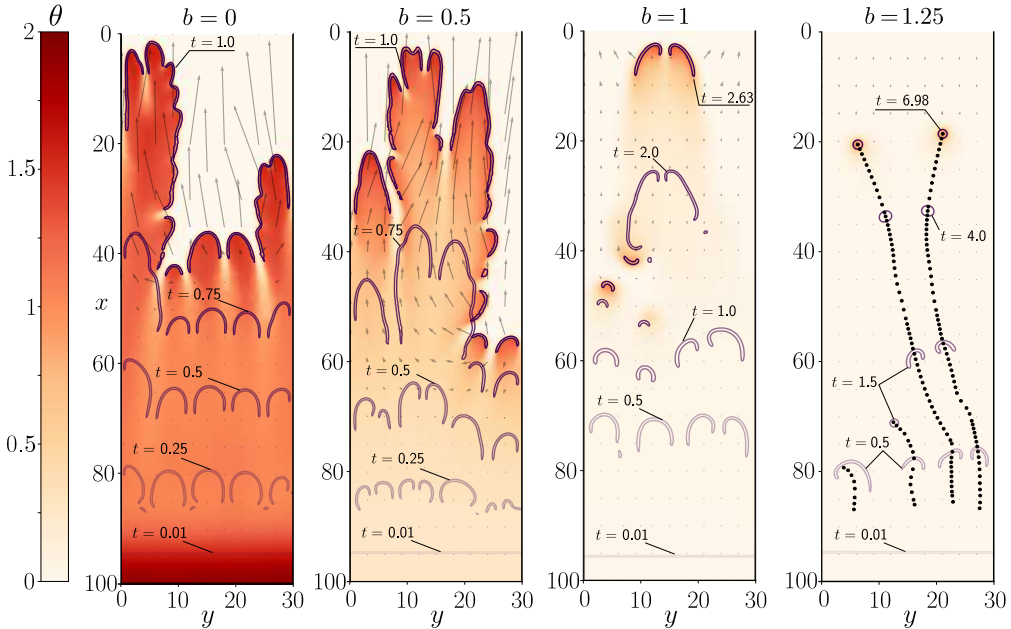


FIGURE 5.3 | Temperature profiles for flame-front propagation in CO configuration at different times, for increasing values of the heat-loss parameter b and $G = 0$.

5.2.3 Flame velocity and burning times

The qualitative differences shown above between OC and CO cases appear due to the imposed boundary conditions and can be characterized with a detailed quantitative post-processing of the numerical data. Major variations are obtained first in the burning time, defined as the period employed by the flame to propagate along the chamber. It depends on the induced base flow that drags out or pushes forward the front. The burning time can be used together with the associated chamber length to represent an average flame velocity in a fixed reference frame. However, the evolution with time of the dimensionless region occupied by the unburned gases $V_u = \int_{\Gamma} d\sigma / (LW)$, with Γ defined as the region in which the mass fraction satisfies the condition $Y = Y_{def}/Y_F > 0.95$, is represented in Fig. 5.4 (a) for OC and Fig. 5.4 (b) for CO under different values of b . A monotonic behavior is kept for the depletion of unburned reactants for both cases, increasing the burning time as the flame is slowed-down with greater heat losses. The time of complete depletion is significantly shorter for any value

of b in the CO case than in the OC case. This is due to the effect of the over-pressure that is produced by the confined products. In addition, the expanding flow exiting the chamber produces an exhaust of pure mixture out of the computational domain. Furthermore, the overall propagation rate S_T relative to the planar flame velocity S_L [25] is calculated as

$$\frac{S_T}{S_L} = \frac{1}{LW} \int_0^W \int_0^L \Omega \, dx \, dy. \quad (5.3)$$

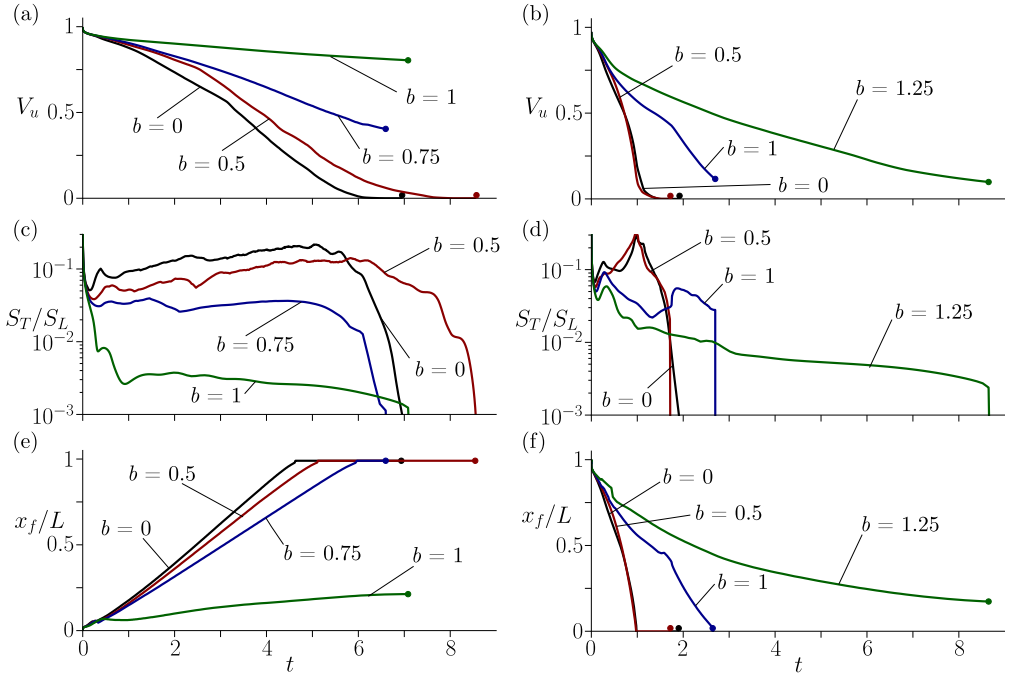


FIGURE 5.4 | Unburned volume V_u (a-b), flame velocity S_T/S_L (c-d), and the most advanced position of the flame front x_f/L (e-f) with $G = 0$ and different values of the heat-loss coefficient b in the open-closed (left plots) and closed-open (right plots) configurations. The solid dots indicate $S_T = 0$.

The evolution with time of the propagation rate is plotted in Fig. 5.4 (c) for the OC propagation. Note that a plateau of nearly constant reaction rate and steady propagation is always reached. Nevertheless, for small values of b , this plateau is followed by a sharp decrease to zero once the flame front has consumed the available volume of reactants V_u . For greater values of the heat-loss parameter, this sudden decrease arises as the reaction reaches the end of the chamber ($b = 0.75$ at $t \approx 6.5$) or extinguishes ($b = 1$ at $t \approx 7$), leaving a nearly-entire

domain of unburned reactants behind. In the CO case shown in Fig. 5.4 (d), an accelerated propagation takes place thanks to the progressive increase of pressure and temperatures in the gas products located between the flame and the wall. The flame velocity peaks at the point where the amount of unburned reactants is almost depleted reaching the end of the chamber, and then it progressively diminishes while consuming the available mixture left. For sufficiently large heat losses, the flame extinguishes completely at a finite distance from the ignition point in which the integral of the reaction rate becomes zero ($b = 1.25$).

Finally, the x location of the most advanced position of the flame x_f is evaluated at each time instant by direct measurement of the flow variables. This particular value is used to detect the arrival of the front at the end of the chamber. Note that, for OC propagation in Fig. 5.4 (e), ignition is located at the open end in $x \approx 0$, and reaches the end of the chamber at $x_f/L = 1$. There, the most advanced point of the flame arrives before the full consumption of the reactants has taken place. This effect is also present although less noticeable for the CO configuration Fig. 5.4 (f) with ignition at $x \approx L$.

5.2.4 The role of the thermodiffusive instability

The Lewis number considered in our computations is significantly below unity ($Le = 0.3$), as representative of fuels such as hydrogen. Therefore, thermodiffusive instabilities are likely to heavily affect the development of the flame morphology illustrated in Figs. 5.2 and 5.3. To check to what extent this instability intervenes in the formation of circle or comet-like flames, we plot in Fig. 5.5 the reaction isocontours in OC configuration with $\alpha = 0$ and $Le = 1$.

When the Lewis number is chosen to be around one, the flame becomes stable regarding thermodiffusive instabilities and the front can only be destabilized by the density jump across the reactive front. Now only the perturbations with long wavelength $\lambda \sim O(W)$ grow in time, reducing the curvature of the flame, which takes a mushroom-like shape and heat losses soon offset heat production reducing rapidly the flame temperature and propagation velocity. As expected, the flame shape is left unperturbed until heat losses are intense enough to induce complete extinction of the flame with $b \approx 0.025$. Analogous results where the thermodiffusive cellular behavior is also hindered are found for $Le > 1$, but they are not included here. However, in low-Lewis number flames, small wavelength perturbations $\lambda \sim O(\delta_T)$ are unstable and produce small cells with a characteristic size of the order of the flame thickness δ_T . These

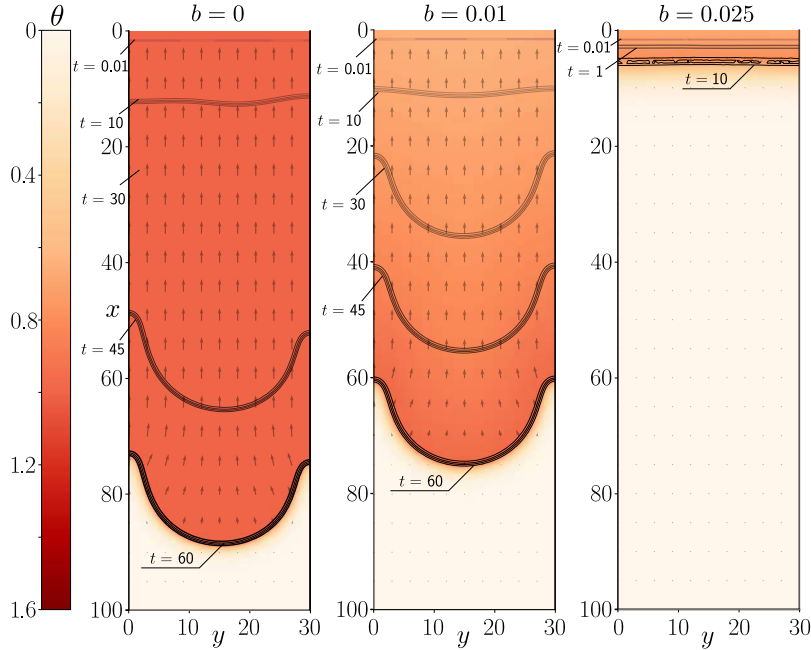


FIGURE 5.5 | Reaction front evolution in gravity-less OC configuration with $Le = 1$ for increasing values of the heat-loss parameter b . Burning times are $t = 67.5$ for $b = 0$ and $t = 78.6$ for $b = 0.01$. Flame extinction is found for $b > 0.01$.

cells present a large curvature which balances heat production and heat losses. This effect helps reaching higher temperatures that keep an active reaction, even when heat losses are relatively large. Under these conditions, the flame approaches to extinction at values of the heat loss parameter $b \simeq O(1)$, much larger than those found for $Le \gtrsim 1$, $b \simeq O(10^{-2})$.

5.3 Effect of the heat losses in buoyant flames

Although it has been shown that conductive heat losses play a key role in the appearance of the circle and comet-like flames in lean highly-diffusive mixtures, the transmission of burning kernels can be enhanced or subdued by means of other mechanisms, such as gravity. In the absence of buoyant convection, heat losses break the reaction front into one or two-headed isolated flame cells that remind the process of flame fragmentation observed in spherical flames [24, 26]. We study now the effect of gravity on the propagation of flames affected by heat losses.

5.3.1 Upward-propagating flames

We shall first consider the light hot combustion products to be located under the cold mixture, which favors the development of the Rayleigh-Taylor instability. In the first approximation, the flame propagation velocity equals the rising velocity of a bubble with equivalent temperature in adiabatic tubes and channels [27]. Nevertheless, the flow in the hot gas behind the flame is far more complex than the cold gas behind an ascending bubble [28], where a recirculating region behind the front could trigger an unstable behavior of the hot fluid. Heat losses and gravity effects were considered by [29] in a HS cell using infinitely-fast chemistry to conclude that the effect of the Darrieus-Landau instability is reduced due to the attenuation of the density change across the reaction front provided by heat losses. However, the influence of the Lewis number was not considered by the authors.

Note that, using the reference system defined in Fig. 5.1, $G < 0$ in the OC configuration and $G > 0$ in the CO configuration represent flames propagating against gravity. Figs. 5.6 and 5.7 show strong differences between the dynamics of flames propagating in the OC and CO cases.

Open-closed (OC) propagation

In this case, the propagation and the structure of the flame do not change significantly for moderate values of the heat loss parameter ($b = 0.5$ or 1). However, the overall propagation rate S_T is evidently affected by heat losses; see the evolution with time of S_T/S_L together with both the unburned volume V_u and the most advanced position of the flame x_f in Fig. 5.7 (a,c and e). Local flame quenching is induced at the flame troughs as the heat loss parameter increases above $b > 0.75$. Then, the flame breaks into several circle-like flame cells separated from each other that travel towards the closed end of the chamber. For $b > 1$, the flame dynamics are modified and the cells formed shortly after ignition become unstable. The surviving one-headed cells grow to reach a maximum size before dividing into two smaller cells. These two interact and either extinguish or grow before splitting again. The dynamics of the new-born cells is erratic with continuous changes of direction and velocity due to the interplay between buoyancy and upstream over-pressure. The evolution is shown in Fig. 5.6 (a) for $b = 1.75$, where the path followed by the flame cells is marked with a solid gray line that becomes thicker as the instantaneous velocity of the flame increases. During the final stage ($t = 10$), the maximum

temperature computed is $\theta_{max} = 1.15$. Gravity induces a preferential propagation upwards with several branches that arise at splitting events, which form a tree-like structure.

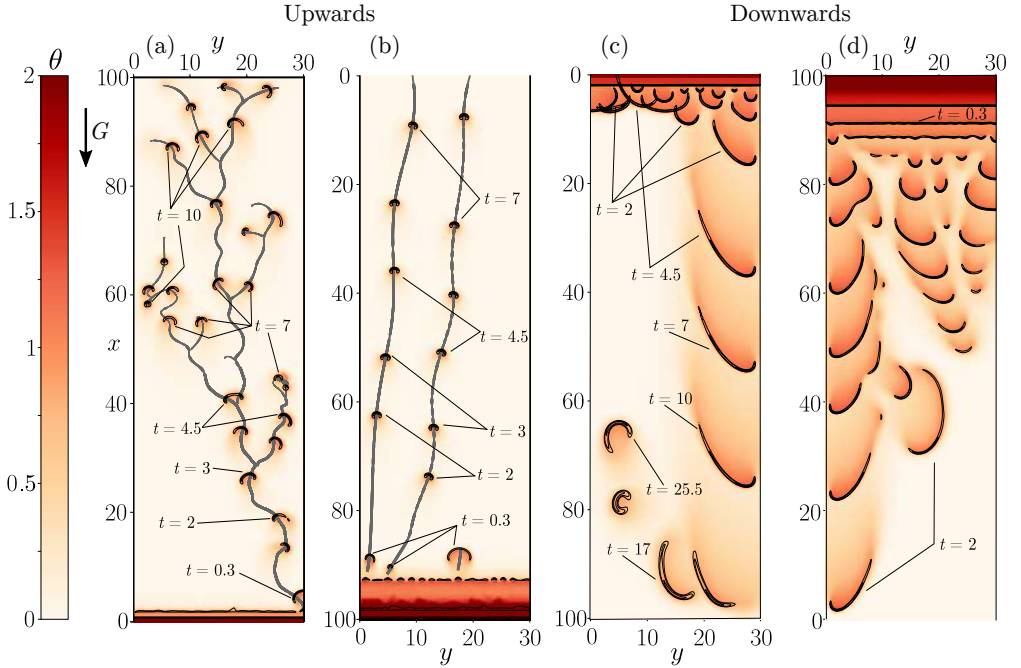


FIGURE 5.6 | Temperature θ (colored isocontours) and reaction rate Ω (black contours) of flame cells propagating upwards (a) {OC, $G = -10$, $b = 1.75$ }, (b) {CO, $G = 10$, $b = 2$ }, and downwards (c) {OC, $G = 10$, $b = 0.3$ }, (d) {CO, $G = -10$, $b = 0.5$ }. The thick lines in (a) and (b) indicate the trajectories followed by the flame cells.

The propagation rate shown in Fig. 5.7 (c) changes suddenly after every cell splitting episode. The comet-like flame grows in size cyclically, reducing the maximum temperature of the region and the propagation rate. Minimum values of S_T are reached just before the flame splits into two smaller cells. Then, curvature causes a new temperature increase and larger values of S_T , which reaches a local maximum when the cell size is minimum. The small values of S_T explain the long burning times observed in Fig. 5.7. For moderately large values of the heat losses parameter ($b < 2$), the flame cells only disappear when they reach the end of the chamber leaving, eventually, some amount of fuel unburned. Total flame extinction occurs abruptly close to the ignition region for values of the heat loss parameter $b \gtrsim 2$.

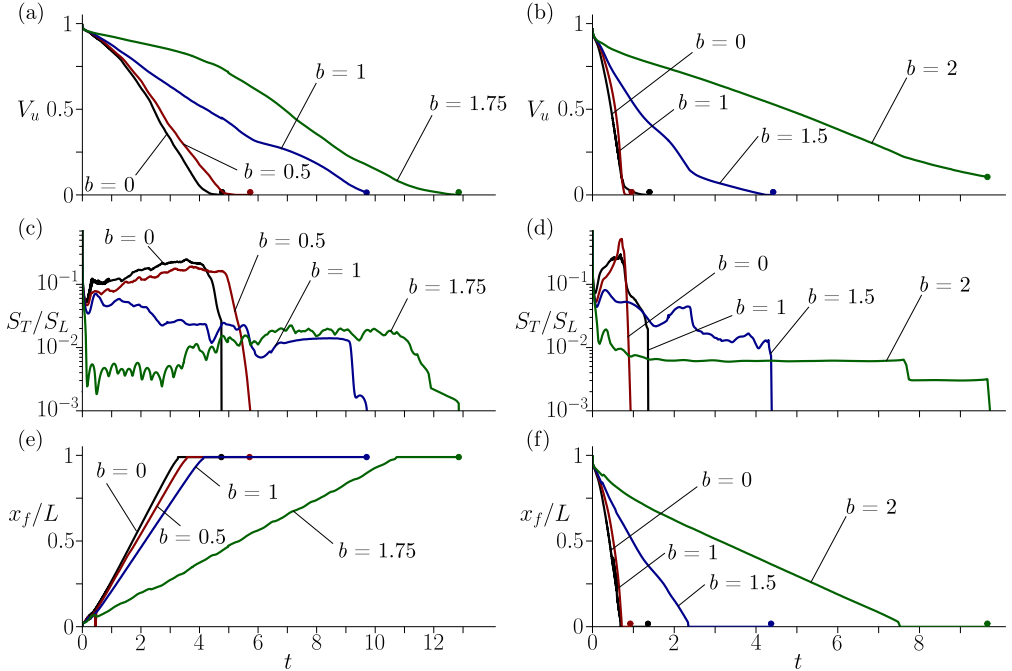


FIGURE 5.7 | (a-b) burned area V_f , (c-d) flame velocity S_T/S_L and (d-e) the most advanced position of the flame front x_f/L for upward propagating flames with different values of the heat losses coefficient b , in OC (left plots $G = -10$) and CO (right plots $G = 10$) configurations.

Closed-open (CO) propagation

The evolution of V_u , S_T and x_f with time is plotted in Fig. 5.7 (b,d and f) for different values of b . The effect of the heat losses is similar to that described above for $G = 0$, with isolated one or two-headed flame cells formed only for $b > 1$ and propagating unsteadily towards the end of the chamber with burning times much shorter than in the OC case. Little or even no effect, besides the deceleration of the reaction rate, is observed for smaller values of the heat-loss parameter $b < 1$. Even though eventual flame cell splitting is observed for $b = 1.5$, the isolated flame cells are much more stable than those computed in the OC configuration, given that buoyancy and over-pressure effects are complementary here.

A representative example of the stable cell propagation is plotted in Fig. 5.6 (b) for $b = 2$ and $G = 10$. Once the circle-like flames are formed, they steadily burn small amounts of fuel keeping a constant size, with maximum temperatures as big as $\theta_{max} = 1.1$ at $t = 7.54$. The

paths are represented as in the previous case, that is, the thickness of the line represents the instantaneous velocity of the flame, showing that it remains almost constant during the whole propagation. In unconfined near-limit mixtures, flames adopt almost spherical shapes [30] and constitute an ensemble of isolated flame balls. Here, the two circle-like flames that appear after the fragmentation of the reactive front move as a whole, keeping the distance between them.

The burning velocity remains small showing a value around $S_T/S_L \approx 6 \times 10^{-3}$. Finally, one of the flames exits the domain and the overall burning velocity is suddenly divided by a factor of two $S_T/S_L \approx 3 \times 10^{-3}$ at $t \approx 7.58$, proving that the two flame circles have a similar propagation speed. As in the unconfined case described by [12], both flame cells move independently to each other with equal traveling velocities $|d\vec{x}_{cg}/dt| \approx 10$, where \vec{x}_{cg} is the instantaneous location of the geometric center of the reaction front, a curve defined as where $Y = 0.1$. The stable behavior is explained as both intervening mechanisms, over-pressure and buoyancy, act in the same direction pushing further the extinction event caused by greater heat losses.

5.3.2 Downward-propagating flames

Flame propagation against buoyancy effects in a HS cell was explored mainly in the study of flame instabilities [22, 31–33]. However, none of the authors considered the effect of conductive heat losses in their studies. Here, $G > 0$ in the OC configuration Fig. 5.6 (c) and $G < 0$ in the CO configuration Fig. 5.6 (d) represent flames propagating in the same direction than gravity.

The effect of heat losses is similar to that described above in horizontal and upwards propagating flames. Sufficiently intense heat losses will break the flame front leaving just a single comet-like flame in both the OC and CO configuration, as is shown in Fig. 5.6 (c-d). For flames propagating downwards we find total extinction before one fourth of the chamber length for $b = 0.4$ and $b = 0.6$ in the OC and CO configurations, respectively, in contrast with $b = 1.8$ and $b = 2.05$ computed for upward propagating flames. Larger values of b are required for production of circle-like flames. However, buoyancy effects succeed in pulling the flame away from the fresh reactants under weak-burning conditions and enable extinction events. The curves for V_u , S_T and x_f are qualitatively very similar to those shown in Fig. 5.4 and are not shown here for the sake of conciseness.

5.4 One or two-headed cell flames

Canonical reactive problems have been relentlessly pursued in experiments and proposed as object of study for their simplified theoretical treatment and large potential to increase the understanding of the physical processes involved. The most representative cases being the theorized premixed flame balls in a quiescent atmosphere with spherical solution by Zel'dovich [15] and isolated droplet burning [34, 35]. These spherical configurations have been reproduced and studied in non-propagating micro-gravity conditions, stabilized by radiation [36–38], and therefore were important to provide useful information about the mechanisms that control the reaction. However, conductive losses at the plates in the integrated transverse direction, facilitate the appearance of new quasi-2D canonical shapes that propagate in a fresh mixture environment. Details of the flow field for a steadily-propagating flame cell in absence of buoyancy and including conductive heat losses are shown in Fig. 5.8 over a moving reference frame. The latter is placed at the center of the propagating cell $\vec{x}' = \vec{x} - \vec{x}_{cg}$.

First, a two-headed stable configuration is depicted in Fig. 5.8 (a) with black lines denoting the contour levels of reaction rate plotted over the colored filled contours of temperature. The flow-field velocity is referred to a frame moving with the flame $\vec{U} - d\vec{x}_{cg}/dt$ and represented by a vector field on top of the mass fraction distribution in Fig. 5.8 (b). This flame shape arises after a reacting cell splits to create a symmetrically coupled front in the CO case $b = 1$ shown above in Fig. 5.3 at $t = 2.63$. This specific configuration propagates in a steady-state manner, stabilized via convection and heat conduction, and particularly showing local extinction, or absence of total merging, in the origin of the moving frame.

Further increase of b generates a simpler circular flame. More precisely, the steady-state propagation of one cellular flame as obtained in the rightmost panel of Fig. 5.3, with $b = 1.25$ and CO configuration, is shown at $t = 6.98$ in Fig. 5.8(c) with the respective temperature and reaction rate profiles. The highly-diffusive species considered here ($Le = 0.3$) plays a major part in the development of the circular shape. As can be seen in Fig. 5.8 (d), the contour lines of unburned mixture close around the burning cell while the flow field runs parallel to the x axis. This suggests that diffusive transport acts preferentially in the transverse direction and the diffusion of fresh species fills up the trail of depleted reactants behind the burning front. Consequently, the cell advancing motion is slow enough to enable species diffusion at distances

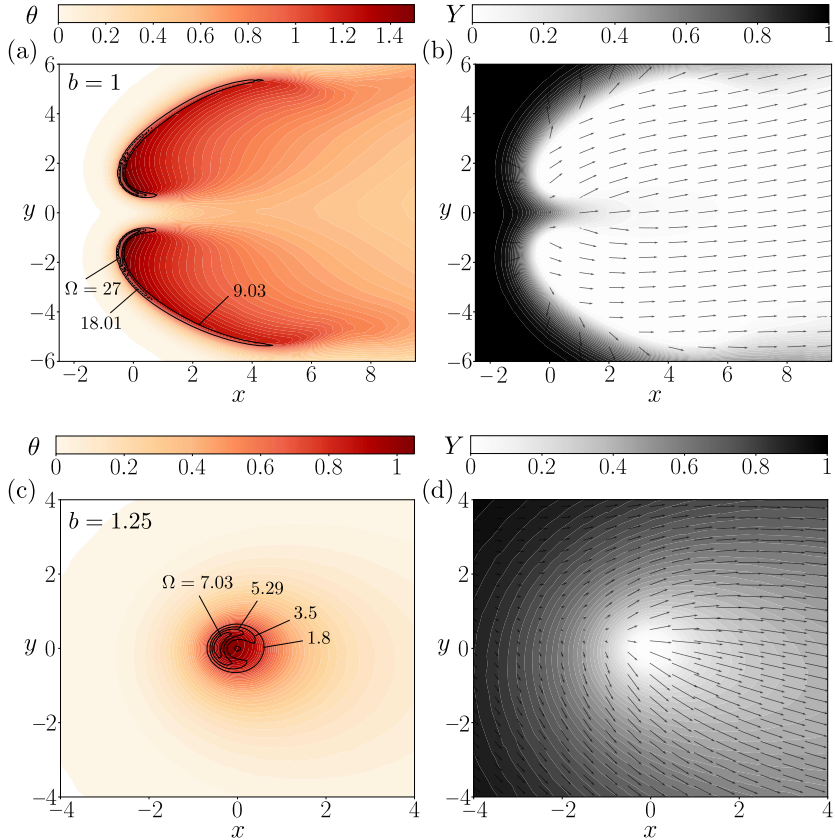


FIGURE 5.8 | Detail of two-headed (a-b) and semicircular (c-d) flames in moving local axes. Temperature contours and superimposed reaction-rate levels (a-c) and mass-fraction distribution with relative flow field velocity \vec{v} (b-d), are pictured for non-buoyant CO propagation with heat-loss parameter $b = 1$ at time $t = 2.63$ (top) and $b = 1.25$ at $t = 6.98$ (bottom).

of the order of the flame radius r_f during the local residence time $t_r \sim r_f/\dot{x}_f$ and produce a closed circular burning front. $\dot{x}_f \sim \dot{x}_{cg} \sim 10S_L$ is extracted from Fig. 5.4 (f), where the flame reaches around 80% of the chamber length in $t \sim 8$. In turn, the time of species diffusion is given by $t_{diff} \sim r_f^2/D_i \sim Le(r_f^2/D_T)$. Therefore, flame circles appear for comparable diffusive and residence times $t_r \sim t_{diff}$, which implies that $r_f \sim (10Le)^{-1}(D_T/S_L) \sim \delta_T/(10Le)$. This is the case of the computations shown in Fig. 5.8 (c) with $Le = 0.3$ and $r_f \sim \delta_T$. However, larger velocities of the cell \dot{x}_f , as the case depicted in Fig 5.8 (a), reduce the action of diffusion behind the flame $t_r \ll t_{diff}$, preventing the generation of circular flames.

Furthermore, the relative flow produced by directional fuel consumption produces stabilization by means of heat convection [20]. Nevertheless, heat losses through the plates are essential to the evolution of continuous fronts into these structures, and are responsible for a net reduction of temperature and burning rate, which consequently diminish the relative convection to provide diffusion-reaction equilibrium and steady propagation. This combination of particular diffusive-thermal conditions enables, in a slowly-reacting front, the nearly-circular distribution of isolated reaction.

References

- [1] I. Staffell, D. Scamman, A. V. Abad, P. Balcombe, P. E. Dodds, P. Ekins, N. Shah, K. R. Ward, The role of hydrogen and fuel cells in the global energy system, *Energy & Environmental Science* 12 (463–491) (2019).
- [2] B. Salvi, K. Subramanian, Sustainable development of road transportation sector using hydrogen energy system, *Renewable and Sustainable Energy Reviews* 51 (1132 - 1155) (2015). doi:<https://doi.org/10.1016/j.rser.2015.07.030>.
- [3] A. L. Sánchez, F. A. Williams, Recent advances in understanding of flammability characteristics of hydrogen, *Progress in Energy and Combustion Science* 41 (1–55) (2014).
- [4] A. Friedrich, J. Grune, T. Jordan, N. Kotchourko, M. Kuznetsov, K. Sempert, G. Stern, Safety of hydrogen as an energy carrier (2009).
- [5] V. P. Utgikar, T. Thiesen, Safety of compressed hydrogen fuel tanks: Leakage from stationary vehicles, *Technology in Society* 27 (315–320) (2005).
- [6] H. F. Coward, F. Brinsley, The dilution-limits of inflammability of gaseous mixtures, *Journal of the Chemical Society, Transactions* 105 (1859–1885) (1914).
- [7] R. Ono, M. Nifuku, S. Fujiwara, S. Horiguchi, T. Oda, Minimum ignition energy of hydrogen air mixture: Effects of humidity and spark duration, *Journal of Electrostatics* 65 (87 - 93) (2007). doi:<https://doi.org/10.1016/j.elstat.2006.07.004>.
- [8] W. Zhang, X. Gou, Z. Chen, Effects of water vapor dilution on the minimum ignition energy of methane, n-butane and n-decane at normal and reduced pressures, *Fuel* 187 (111–116) (2017).
- [9] D. A. Crowl, Y. Jo, The hazards and risks of hydrogen, *Journal of Loss Prevention in the Process Industries* 20 (158–164) (2007).
- [10] R. W. Schefer, W. D. Kulatilaka, B. D. Patterson, T. B. Settersten, Visible emission of hydrogen flames, *Combustion and flame* 156 (1234–1241) (2009).
- [11] L. Schlapbach, Technology: Hydrogen-fuelled vehicles, *Nature* 460 (809) (2009).

- [12] F. A. Williams, J. F. Grcar, A hypothetical burning-velocity formula for very lean hydrogen–air mixtures, *Proceedings of the Combustion Institute* 32 (1351–1357) (2009).
- [13] J. Yanez, M. Kuznetsov, J. Grune, Flame instability of lean hydrogen–air mixtures in a smooth open-ended vertical channel, *Combustion and Flame* 162 (2830–2839) (2015).
- [14] N. Drozdov, Y. B. Zel'dovich, Diffusion phenomena at the limit of flame propagation: An experimental study of the inhibition of explosive mixtures of carbon monoxide, *Zhurnal fizicheskoi khimii* 17 (134–144) (1943).
- [15] Y. B. Zeldovich, Theory of combustion and gas detonation (1944).
- [16] P. D. Ronney, M.-S. Wu, H. G. Pearlman, K. J. Weiland, Experimental study of flame balls in space: Preliminary results from sts-83, *AIAA journal* 36 (1361–1368) (1998).
- [17] J. Buckmaster, G. Joulin, P. Ronney, The structure and stability of nonadiabatic flame balls, *Combustion and Flame* 79 (381–392) (1990).
- [18] J. Buckmaster, G. Joulin, P. Ronney, The structure and stability of nonadiabatic flame balls: II. effects of far-field losses, *Combustion and Flame* 84 (411–422) (1991).
- [19] J. Buckmaster, M. Smooke, V. Giovangigli, Analytical and numerical modeling of flame-balls in hydrogen-air mixtures, *Combustion and Flame* 94 (113–124) (1993).
- [20] J. F. Grcar, A new type of steady and stable, laminar, premixed flame in ultra-lean, hydrogen–air combustion, *Proceedings of the Combustion Institute* 32 (1011–1018) (2009).
- [21] Z. Zhou, Y. Shoshin, F. E. Hernández-Pérez, J. A. van Oijen, L. P. de Goey, Formation and stabilization of multiple ball-like flames at earth gravity, *Combustion and Flame* 192 (35 - 43) (2018).
- [22] D. Fernández-Galisteo, V. N. Kurdyumov, P. D. Ronney, Analysis of premixed flame propagation between two closely-spaced parallel plates, *Combustion and Flame* 190 (133–145) (2018).
- [23] J. Yuan, Y. Ju, C. K. Law, Coupled hydrodynamic and diffusional-thermal instabilities in flame propagation at subunity Lewis publishers, *Physics of fluids* 17 (074106) (2005).

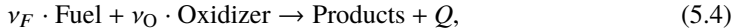
- [24] L. Kagan, S. Minaev, G. Sivashinsky, On self-drifting flame balls, *Mathematics and Computers in Simulation* 65 (511–520) (2004).
- [25] J. Daou, M. Matalon, Influence of conductive heat-losses on the propagation of premixed flames in channels, *Combustion and Flame* 128 (321–339) (2002).
- [26] L. Kagan, G. Sivashinsky, Self-fragmentation of nonadiabatic cellular flames, *Combustion and flame* 108 (220–226) (1997).
- [27] Y. Shtemler, G. Sivashinsky, On upward propagating flames, *Combustion science and technology* 102 (81–93) (1994).
- [28] F. Higuera, Numerical simulation of the upward propagation of a flame in a vertical tube filled with a very lean mixture, *Combustion and Flame* 158 (885–892) (2011).
- [29] G. Joulin, G. Sivashinsky, Influence of momentum and heat losses on the large-scale stability of quasi-2D premixed flames, *Combustion Science and Technology* 98 (11–23) (1994).
- [30] Y. Shoshin, J. Van Oijen, A. Sepman, L. De Goey, Experimental and computational study of the transition to the flame ball regime at normal gravity, *Proceedings of the Combustion Institute* 33 (1211–1218) (2011).
- [31] C. Almarcha, J. Quinard, B. Denet, E. Al-Sarraf, J. Laugier, E. Villermaux, Experimental two dimensional cellular flames, *Physics of Fluids* 27 (091110) (2015).
- [32] E. Al Sarraf, C. Almarcha, J. Quinard, B. Radisson, B. Denet, Quantitative analysis of flame instabilities in a Hele-Shaw burner, *Flow, Turbulence and Combustion* 101 (851–868) (2018).
- [33] E. Al Sarraf, C. Almarcha, J. Quinard, B. Radisson, B. Denet, P. Garcia-Ybarra, Darrieus–Landau instability and Markstein publishers of premixed flames in a Hele-Shaw cell, *Proceedings of the Combustion Institute* 37 (1783–1789) (2019).
- [34] G. Godslove, Burning of fuel droplets, *Symposium (International) on Combustion* 4 (818–830) (1953).

- [35] D. Spalding, The combustion of liquid fuels, *Symposium (International) on Combustion* 4 (847–864) (1953).
- [36] P. D. Ronney, Understanding combustion processes through microgravity research, *Proceedings of the Combustion Institute* 27 (2485–2506) (1998).
- [37] D. L. Dietrich, J. B. Haggard Jr, F. L. Dryer, V. Nayagam, B. D. Shaw, F. A. Williams, Droplet combustion experiments in spacelab, *Symposium (International) on Combustion* 26 (1201–1207) (1996).
- [38] E. Fernández-Tarrazo, A. L. Sánchez, A. Liñán, F. Williams, The structure of lean hydrogen-air flame balls, *Proceedings of the Combustion Institute* 33 (1203–1210) (2011).
- [39] D. Martínez-Ruiz, F. Veiga-López, D. Fernández-Galisteo, V. N. Kurdyumov, M. Sánchez-Sanz, The role of conductive heat losses on the formation of isolated flame cells in hele-shaw chambers, *Combustion and Flame* 209 (187–199) (2019).
- [40] D. Fernández-Galisteo, C. Jiménez, M. Sánchez-Sanz, V. N. Kurdyumov, Effects of stoichiometry on premixed flames propagating in narrow channels: symmetry-breaking bifurcations, *Combustion Theory and Modelling* 21 (1050–1065) (2017).
- [41] V. N. Kurdyumov, M. Matalon, Flame acceleration in long narrow open channels, *Proceedings of the Combustion Institute* 34 (865–872) (2013).
- [42] D. Boffi, F. Brezzi, M. Fortin, et al., Mixed finite element methods and applications, Vol. 44, Springer, 2013 (2013).
- [43] Y. Notay, AGMG software and documentation, <http://homenumber.ulb.ac.be/~{}ynotay/AGMG>.

5.A Mathematical formulation*

This appendix addresses the mathematical formulation used to calculate numerically the results presented above. Note that the nomenclature of this appendix is somehow special and different from the rest of the dissertation and not included in the nomenclature list.

The problem addressed here first considers a fresh homogeneous mixture of reactants of density ρ_u and temperature T_u . These gases are confined between two parallel plates of dimensions $L \times W$ separated a distance h apart. Upon ignition, the overall propagation rate of the flame front S_T is determined by the kinetics of the reaction and the induced flame wrinkling. A simplified one-step irreversible scheme is proposed to model the chemical reaction,



where Q is the heat produced by the reaction and ν_i are the stoichiometric coefficients. In the limit of very lean flames studied here, the chemical reaction rate can be written in the Arrhenius form

$$\Omega = \mathcal{B}(\rho)^2 \frac{Y_{def}}{\mathbb{M}_F} \exp\left(-\frac{E}{\mathcal{R}T}\right), \quad (5.5)$$

where E is the global activation energy required to trigger the reaction, \mathcal{R} is the universal gas constant, \mathcal{B} is the frequency factor, Y_{def} is the mass fraction of the deficient reactant and \mathbb{M}_F its molecular mass.

Scales and governing equations

Changes in the fluid properties along the coordinates (x, y) are produced across distances of the order of the flame thickness $\delta_T = D_{T_u}/S_L$, with D_{T_u} the thermal diffusivity of the fresh gas mixture and S_L the burning velocity of the planar adiabatic flame. Therefore, we scale the problem using δ_T as the characteristic length to define the non-dimensional coordinates $x' = x/\delta_T$ and $y' = y/\delta_T$, with the transverse coordinate $z' = z/h$ scaled with the gap size h . S_L is used to define the dimensionless gas velocity variables $u'_x = u_x/S_L$ and $u'_y = u_y/S_L$. The appropriate scale of the transverse velocity $u'_z = u_z/(aS_L)$ is determined

*This appendix was not developed by the main author, Fernando Veiga López, but is included in this dissertation from [39] for completeness.

by an order-of-magnitude analysis of the continuity equation, with $a = h/\delta_T$. Using the aforementioned magnitudes, the dimensionless time is defined as $t' = t/(\delta_T/S_L)$.

The state variables satisfy the ideal gas equation $p = \rho\mathcal{R}T$, with \mathcal{R} the gas constant of the mixture. Therefore, pressure is scaled with the initial value $\rho_u\mathcal{R}T_u$. It must be noted that, thermodynamic pressure $P(t)$ is differentiated from the hydrodynamic variation $p - P(t)$. Thus, the ideal gas equation in its dimensionless form reads

$$\rho'(1 + q'\theta) = P'(t) + \gamma_g \left(\frac{M}{a} \right)^2 p', \quad (5.6)$$

where the dimensionless variables are $P'(t) = P(t)/(\rho_u\mathcal{R}T_u)$ the thermodynamic pressure, $p' = [p - P(t)]/[\rho_u S_L^2/a^2]$ the hydrodynamic pressure variation, $\rho' = \rho/\rho_u$ the mixture density and $\theta = (T - T_u)/(T_b - T_u)$ the temperature. Moreover, $q = (T_b - T_u)/T_u$ is the dimensionless heat of reaction, with the adiabatic temperature of the flame written as

$$T_b = T_u + \frac{Y_F Q}{c_p \nu_F \bar{M}_F} = T_u(1 + q), \quad (5.7)$$

and ν_F the stoichiometric coefficient of the limiting reactant. From now on, the primed dimensionless variables will be written without its superscript in complex equations for the sake of clarity. Using the dimensionless variables defined above, the continuity and momentum equations can be written as,

$$\frac{\partial \rho}{\partial t} + \frac{\partial(\rho u_x)}{\partial x} + \frac{\partial(\rho u_y)}{\partial y} + \frac{\partial(\rho u_z)}{\partial z} = 0, \quad (5.8)$$

$$\begin{aligned} \rho \left[\frac{\partial u_x}{\partial t} + u_x \frac{\partial u_x}{\partial x} + u_y \frac{\partial u_x}{\partial y} + u_z \frac{\partial u_x}{\partial z} \right] &= \\ &= -\frac{1}{a^2} \frac{\partial p}{\partial x} + Pr \left[\frac{\partial \tau_{xx}}{\partial x} + \frac{\partial \tau_{xy}}{\partial y} + \frac{1}{a} \frac{\partial \tau_{xz}}{\partial z} \right] \pm \frac{\rho G}{a^2}, \end{aligned} \quad (5.9)$$

$$\rho \left[\frac{\partial u_y}{\partial t} + u_x \frac{\partial u_y}{\partial x} + u_y \frac{\partial u_y}{\partial y} + u_z \frac{\partial u_y}{\partial z} \right] = -\frac{1}{a^2} \frac{\partial p}{\partial y} + Pr \left[\frac{\partial \tau_{yx}}{\partial x} + \frac{\partial \tau_{yy}}{\partial y} + \frac{1}{a} \frac{\partial \tau_{yz}}{\partial z} \right], \quad (5.10)$$

$$\rho \left[\frac{\partial u_z}{\partial t} + u_x \frac{\partial u_z}{\partial x} + u_y \frac{\partial u_z}{\partial y} + u_z \frac{\partial u_z}{\partial z} \right] = -\frac{1}{a^4} \frac{\partial p}{\partial z} + \frac{Pr}{a} \left[\frac{\partial \tau_{zx}}{\partial x} + \frac{\partial \tau_{zy}}{\partial y} + \frac{1}{a} \frac{\partial \tau_{zz}}{\partial z} \right], \quad (5.11)$$

where the Prandtl number is $Pr = \mu_u / (\rho_u D_{T_u})$ and $G = g \sin(\alpha) \delta_T a^2 / S_L^2$ is the gravity term included in the longitudinal direction to act against or in favor of the global flame propagation. α represents the angle formed by the gravity vector and the normal to the HS cell \vec{e}_z . The viscous terms introduced in the previous equations are

$$\begin{aligned} \tau_{xx} &= \mu \left(2 \frac{\partial u_x}{\partial x} - \frac{2}{3} \nabla \cdot \bar{u} \right), & \tau_{xy} = \tau_{yx} &= \mu \left(\frac{\partial u_x}{\partial y} + \frac{\partial u_y}{\partial x} \right), \\ \tau_{yy} &= \mu \left(2 \frac{\partial u_y}{\partial y} - \frac{2}{3} \nabla \cdot \bar{u} \right), & \tau_{yz} = \tau_{zy} &= \mu \left(\frac{1}{a} \frac{\partial u_y}{\partial z} + a \frac{\partial u_z}{\partial y} \right), \\ \tau_{zz} &= \mu \left(2 \frac{\partial u_z}{\partial z} - \frac{2}{3} \nabla \cdot \bar{u} \right), & \tau_{zx} = \tau_{xz} &= \mu \left(\frac{1}{a} \frac{\partial u_x}{\partial z} + a \frac{\partial u_z}{\partial x} \right), \end{aligned}$$

being $\mu' = \mu / \mu_u$ the viscous coefficient. The conservation equation for the mass fraction of the deficient species $Y' = Y_{def} / Y_F$ yields

$$\begin{aligned} \rho \left[\frac{\partial Y}{\partial t} + u_x \frac{\partial Y}{\partial x} + u_y \frac{\partial Y}{\partial y} + u_z \frac{\partial Y}{\partial z} \right] &= \\ &= \frac{1}{Le} \left[\frac{\partial}{\partial x} \left(\rho D \frac{\partial Y}{\partial x} \right) + \frac{\partial}{\partial y} \left(\rho D \frac{\partial Y}{\partial y} \right) + \frac{1}{a^2} \frac{\partial}{\partial z} \left(\rho D \frac{\partial Y}{\partial z} \right) \right] - \Omega, \quad (5.12) \end{aligned}$$

with $D' = D / D_u$ the species mass diffusivity coefficient, $Le = D_{T_u} / D_u$ the Lewis number, and $\Omega' = (\Omega \nu \mathbb{M} D_{T_u}) / (\rho_u S_L^2 Y_u)$ the dimensionless reaction rate. The energy equation in terms of θ reads

$$\begin{aligned} \rho \left[\frac{\partial \theta}{\partial t} + u_x \frac{\partial \theta}{\partial x} + u_y \frac{\partial \theta}{\partial y} + u_z \frac{\partial \theta}{\partial z} \right] &= \frac{\gamma_g - 1}{q} \left[\frac{1}{\gamma_g} \frac{\partial P}{\partial t} + \right. \\ &\quad \left. + \left(\frac{M}{a} \right)^2 \left(\Phi_v Pr + \frac{\partial p}{\partial t} + u_x \frac{\partial p}{\partial x} + u_y \frac{\partial p}{\partial y} + u_z \frac{\partial p}{\partial z} \right) \right] + \frac{\partial}{\partial x} \left(\rho D_T \frac{\partial \theta}{\partial x} \right) + \\ &\quad + \frac{\partial}{\partial y} \left(\rho D_T \frac{\partial \theta}{\partial y} \right) + \frac{1}{a^2} \frac{\partial}{\partial z} \left(\rho D_T \frac{\partial \theta}{\partial z} \right) + \Omega, \quad (5.13) \end{aligned}$$

where $D'_T = D_T / D_{T_u}$ is the nondimensional thermal diffusivity, $\gamma_g = c_p / c_v$ is the adiabatic

index and Φ_v is the viscous dissipation,

$$\begin{aligned}\Phi_v = a^2 \mu & \left\{ 2 \left[\left(\frac{\partial u_x}{\partial x} \right)^2 + \left(\frac{\partial u_y}{\partial y} \right)^2 + \left(\frac{\partial u_z}{\partial z} \right)^2 \right] + \left[\frac{\partial u_y}{\partial x} + \frac{\partial u_x}{\partial y} \right]^2 + \right. \\ & \left. + \left[\frac{1}{a} \frac{\partial u_y}{\partial z} + a \frac{\partial u_z}{\partial y} \right]^2 + \left[a \frac{\partial u_z}{\partial x} + \frac{1}{a} \frac{\partial u_x}{\partial z} \right]^2 - \frac{2}{3} \left[\frac{\partial u_x}{\partial x} + \frac{\partial u_y}{\partial y} + \frac{\partial u_z}{\partial z} \right]^2 \right\}. \quad (5.14)\end{aligned}$$

Likewise, the dimensionless diffusive transport coefficients follow a power law with temperature in the form $\mu = \rho D_T = \rho D = (1 + q\theta)^\sigma$. Finally, the dimensionless reaction rate Ω' is given by

$$\Omega' = \rho^2 \beta^2 (1 + q)^{2-\sigma} \frac{Y}{2s_L^2 Le} \exp \left(\frac{\beta(\theta - 1)}{1 + \frac{q}{q+1}(\theta - 1)} \right), \quad (5.15)$$

with the Zel'dovich number defined as $\beta = E(T_b - T_u)/(\mathcal{R}T_b^2)$. The factor $s_L = (S_L)/(S_L)_{asp} = 1.05$ is the eigenvalue of the planar adiabatic problem [40], where the propagation velocity S_L for finite β is compared with the propagation velocity for infinitely-large activation energy $(S_L)_{asp}$.

To include the effect of conductive heat losses on the propagation of the flame, the heat equation must be solved in the solid plates that form the channel. Considering that the temperature on the external surface of the plates is kept at a constant temperature T_u and that the plates thickness is h_w , the temperature in the solid walls $\theta_w = (T_w - T_u)/(T_b - T_u)$ can be obtained by integrating the non-dimensional heat equation

$$-\frac{\rho_w c_w}{\rho_u c_p} \frac{\partial \theta_w}{\partial t} + \frac{\partial}{\partial x} \left(\frac{k_w}{k_u} \frac{\partial \theta_w}{\partial x} \right) + \frac{\partial}{\partial y} \left(\frac{k_w}{k_u} \frac{\partial \theta_w}{\partial y} \right) + \frac{1}{a^2} \frac{\partial}{\partial z} \left(\frac{k_w}{k_u} \frac{\partial \theta_w}{\partial z} \right) = 0, \quad (5.16)$$

where ρ_w , k_w and c_w are the density, the thermal conductivity and the heat capacity of the solid plates, respectively, and k_u is the thermal conductivity of the fresh gas mixture. For convenience, we only define here the boundary conditions in the z direction required to solve the system of equations (5.8)-(5.16), where

$$u_x = u_y = u_z = \frac{\partial Y}{\partial z} = 0, \quad \theta_w = \theta, \quad \frac{\partial \theta}{\partial z} = a^2 \frac{b}{2\mu} \frac{h_w}{h} \frac{\partial \theta_w}{\partial z} \quad (5.17)$$

along the inner surface of the solid plates $z = 0$ and $z = 1$ and $\theta_w = 0$ on the outer surface of

the solid plates $z = -h_w/h$ and $z = 1 + h_w/h$. The order-unity heat-loss parameter

$$b = \frac{2}{a^2} \frac{h}{h_w} \frac{k_w}{k_u} \geq 0, \quad (5.18)$$

naturally arises to quantify the rate of heat flux across the walls. In addition, symmetry is imposed at the midplane of the channel $z = 1/2$,

$$v = \frac{\partial u}{\partial z} = \frac{\partial Y}{\partial z} = \frac{\partial \theta}{\partial z} = 0. \quad (5.19)$$

Quasi-2D limit in semi-confined geometries

The three-dimensional problem presented before can be simplified in the limit of low-Mach propagation ($M/a \ll 1$) and very narrow channels $a = h/\delta_T \ll 1$ to a much simpler quasi-2D problem. The characteristic Reynolds number $Re = \rho_u S_L h / \mu_u = a/Pr \ll 1$ is small. In the cases studied here, hydrodynamic pressure variations $p'(x, y, z; t) \sim \rho_u S_L^2 / (h/\delta_T)^2$ are much smaller than the thermodynamic pressure $P'(t) \sim \rho_u R_g T_u$, yielding $p'/P' \sim (M/a)^2 \ll 1$ and neglecting $\partial P/\partial t$ in (5.13). The simplified equation of state takes its quasi-isobaric form

$$\rho(1 + q\theta) = 1, \quad (5.20)$$

with the combustion chamber open to the atmosphere at one end. In this narrow-channel limit, the flow field variables $\Psi = \{\theta_w, \theta, Y, p\}$, are accordingly expanded as [41]

$$\Psi = \Psi_0 + a^2 \Psi_1 + O(a^4) \dots \quad (5.21)$$

Introducing this perturbed expansion in (5.12), (5.13) and (5.16), we obtain to leading order

$$\frac{\partial}{\partial z} \left(\rho_0 D_T \frac{\partial \theta_0}{\partial z} \right) = \frac{\partial}{\partial z} \left(\rho_0 D \frac{\partial Y_0}{\partial z} \right) = \frac{\partial}{\partial z} \left(\frac{k_w}{k_u} \frac{\partial \theta_{w0}}{\partial z} \right) = 0 \quad (5.22)$$

which yields, after imposing the boundary conditions (5.17) and (5.19), constant profiles of species and gas temperature in the transverse coordinate $\theta_0 = \theta_0(x, y; t)$, $Y_0 = Y_0(x, y; t)$ and a linear profile for the upper $\theta_{w0} = \theta_0[1 + (1 - z)h/h_w]$ and lower $\theta_{w0} = \theta_0(1 + zh/h_w)$ wall temperatures.

In turn, the momentum equation in the z direction simplifies to $\partial p_0 / \partial z = 0$ to give $p_0 = p_0(x, y; t)$. The separation between the plates is small enough to make the viscous terms dominant in (5.9) and (5.10) with the velocity profiles instantly developing as a Poiseuille flow $u_{0x} = 6z(1 - z)U_x$ and $u_{0y} = 6z(1 - z)U_y$, with

$$U_x = -\frac{1}{12\mu Pr} \left(\frac{\partial p_0}{\partial x} \pm \rho_0 G \right) \quad \text{and} \quad U_y = -\frac{1}{12\mu Pr} \frac{\partial p_0}{\partial y} \quad (5.23)$$

obtained after imposing the non-slip boundary conditions (5.17). The equations to account for the first-order corrections ($\sim O(a^2)$) of temperature θ_1 , mass fraction Y_1 and pressure p_1 can be obtained by introducing the expanded variables (5.21) in the continuity (5.8), species (5.12) and energy (5.13) equations. An average contribution of the transverse variations is therefore included by integrating the resulting expressions in the z direction and imposing the wall-boundary conditions at the plates

$$\text{at } z = 1, \quad Y_1 = 0, \quad \frac{\partial \theta_1}{\partial z} = -\frac{b}{2\mu} \theta_0, \quad (5.24)$$

$$\text{at } z = 0, \quad Y_1 = 0, \quad \frac{\partial \theta_1}{\partial z} = \frac{b}{2\mu} \theta_0. \quad (5.25)$$

As a result, the equations for the first-order terms θ_0, Y_0, p_0 , constant in z , yield

$$\frac{\partial \rho_0}{\partial t} + \frac{\partial}{\partial x} (\rho_0 U_x) + \frac{\partial}{\partial y} (\rho_0 U_y) = 0, \quad (5.26)$$

$$\rho_0 \frac{\partial \theta_0}{\partial t} + \rho_0 U_x \frac{\partial \theta_0}{\partial x} + \rho_0 U_y \frac{\partial \theta_0}{\partial y} = \nabla \cdot (\rho_0 D_T \nabla \theta_0) + \Omega - b\theta_0, \quad (5.27)$$

$$\rho_0 \frac{\partial Y_0}{\partial t} + \rho_0 U_x \frac{\partial Y_0}{\partial x} + \rho_0 U_y \frac{\partial Y_0}{\partial y} = \frac{1}{Le} \nabla \cdot (\rho_0 D \nabla Y_0) - \Omega, \quad (5.28)$$

where the operator ∇ is defined only in the (x, y) plane. Finally, combining Eqs. (5.20), (5.26), (5.27), and making use of the Poiseuille description (5.23), we can develop an expression

Parameter	Symbol	Value
Gravity parameter	$G = g \sin(\alpha) \delta_T a^2 / S_L^2$	$-10 < G < 10$
Heat of reaction	$q = (T_b - T_u)/T_u$	5
Heat capacity ratio	$\gamma_g = c_p/c_v$	1.4
Heat losses	$b = 2(h/h_w)(k_w/k_u)/a^2$	$0 < b < 2.5$
HS chamber width	W	30
HS chamber length	L	100
Ignition Temperature	θ_i	2.5
Ignition size	r_0	1
Ignition location	x_0/L	0.01 or 0.99
Ignition wavenumber	k_i	2
Lewis number	$Le = D_{T_u}/D_u$	0.3
Prandtl number	$Pr = \mu_u/(\rho_u D_{T_u})$	0.7
Planar velocity ratio	$s_L = S_L/(S_L)_{asp}$	1.05
Zel'dovich Number	$\beta = E(T_b - T_u)/(R_g T_b^2)$	10
Transport power law	σ	0

TABLE 5.1 | Value of the dimensionless physical parameters used in the computations below.

for the spatial variations of pressure,

$$\frac{1}{12Pr} \nabla^2 p_0 = q\mu [\nabla \cdot (\mu \nabla \theta_0) + \Omega - b\theta_0] + \frac{1}{12Pr} \left[\nabla \mu \nabla p_0 \pm \frac{\partial \rho_0}{\partial x} G \mp \rho_0 G \frac{\partial \mu}{\partial x} \right]. \quad (5.29)$$

The complete formulation presented here accounts for the thermal expansion of the burnt gases, buoyancy, temperature-dependent diffusion coefficients, thermodiffusive effects, conductive heat losses at the walls and dynamic pressure variations in the premixed-flame combustion problem in open chambers. Therefore, it allows the analysis through numerical simulations of separated effects, such as the Rayleigh-Taylor, Darrieus-Landau, Saffman-Taylor and cellular instabilities, on flame dynamics, local quenching, flame wrinkling and change of the propagation speed.

Boundary and initial conditions

The problem to be solved, defined by the system (5.20), (5.23) and (5.27)-(5.29) needs specific boundary conditions in the 2D plane. We consider, at $y = 0$, $y = W$ and $x = L$

adiabatic and non-permeable walls

$$\frac{\partial p_0}{\partial n} = 0, \quad \frac{\partial Y_0}{\partial n} = 0, \quad \frac{\partial \theta_0}{\partial n} = 0, \quad (5.30)$$

with n representing the normal direction to each of the boundaries. The boundary at $x = 0$ is left open to the ambient $p_0 = 0$, allowing a net flux of mass, species and temperature out of the chamber, and the subscript 0 is dropped for simplicity from now on.

Ignition strongly influences the evolution of the propagation by defining the state of the mixture just after the energy deposition. The initial condition at $t = 0$ is an unburned mixture, $Y = 1$, at rest, $p = 0$, and a temperature field that decays exponentially with the distance from the ignition line placed at x_0 . The latter is perturbed as a sinusoid of small amplitude $A = 0.01$ in the y direction,

$$\theta = \theta_i \left[1 + A \sin \left(2\pi k_i \frac{y}{W} \right) \right] \exp \left\{ -\frac{|x - x_0|}{r_0} \right\}, \quad (5.31)$$

with $\theta_i = 2.5$ and $r_0 = 1$ the dimensionless temperature and size of the ignition regions respectively. The parameter k_i is introduced to add a perturbation wavenumber in the wrinkling and propagation of the flame. Furthermore, the initial condition (5.31) allows the calculation of two different configurations, as sketched in Fig. 5.1. When $x_0 = 0.01L$, the ignition end remains open and the flame propagates toward the closed end of the Hele–Shaw chamber, progressively building up pressure that opposes to the thermally-induced flow (open-closed configuration, OC). On the other hand, choosing $x_0 = 0.99L$, ignition occurs at the closed end and the flame propagates towards the open end, enhancing the flame propagation velocity as a consequence of the expansion of burned gases acting against the back wall (closed-open configuration, CO). Keeping in mind the objective of isolating certain physical processes, such as the ones caused by heat losses, the numerical simulations are first presented here with $\sigma = 0$ for the temperature power law of the diffusion coefficients. The value of the numerical parameters used in the computations below are summarized in Table 5.1 and will be kept constant hereafter if not specified otherwise.

Numerical method

The characterization of the flame and flow evolution in relation to the parameters of the problem is performed through CFD simulations. Finite elements are used with an in-house

Freefem⁺⁺ code to compute numerically the propagation of premixed flames for different conductive heat-losses. The system of equations is solved in the spatial domain Σ , discretized using a conforming triangulation T_h^n , with the subscript h indicating the mesh discretization and n the time instant. The spatial triangulation T_h^n may change from one time step to another, adapting the distribution of grid elements to the evolving features of the numerical solution as shown in Fig. 5.9 (a). The element refinement follows a combined criteria that is based on the steepness of the gradient of the temperature θ , reaction rate Ω and pressure p .

The equations are computed in their weak formulation, reducing the calculation to finding the functions $\theta_0(\vec{x}, t)$, $Y_0(\vec{x}, t)$ and $p_0(\vec{x}, t)$, with \vec{x} in a functional space $P_{m,h}$. Here, $P_{m,h}$ constitutes the finite-element space of polynomials of degree m on each cell of the domain triangulation T_h^n . The finite element solution is then expressed as a linear combination of basic functions of the functional space $P_{m,h}$, with piece-wise quadratic functions $m = 2$ for θ_0 , Y_0 , and linear piece-wise polynomials $m = 1$ for pressure p_0 in order to satisfy the inf-sup (or Babuska-Brezzi) condition [42].

A second-order backward difference formula (BDF scheme) is applied for time discretization. At each time step, the values of the dependent variables (namely θ_0 , Y_0 , and p_0) must be determined. To compute these values, the strongly coupled, highly-nonlinear equations are solved by means of a fully-implicit Newton iterative method. At time t^n , the iteration starts with $k = 1$ using U_x^{n-1} and U_y^{n-1} to solve the system (5.20), (5.27), (5.28) for $\rho_0^{k,n}$, $\theta_0^{k,n}$ and $Y_0^{k,n}$. New values of the pressure variable are obtained $p_0^{k,n}$ by integrating (5.29), to then obtain the new velocity components $U_x^{k,n}$ and $U_y^{k,n}$ from (5.23). The procedure continues iteratively until the error

$$\varepsilon = \sum_{j=1}^3 \frac{\|c_j^{k+1,n} - c_j^{k,n}\|_\infty}{\|c_j^{k+1,n}\|_\infty}, c = \rho, \theta, p$$

is smaller than a prescribed tolerance $\varepsilon = 10^{-4}$.

Maximum size of the mesh elements

The high-resolution of the triangulated mesh used in the computations is a key parameter in determining the accuracy of the results. As indicated above, it is adapted at every time step to cluster elements in the reaction region where the maximum gradients of temperature, reaction

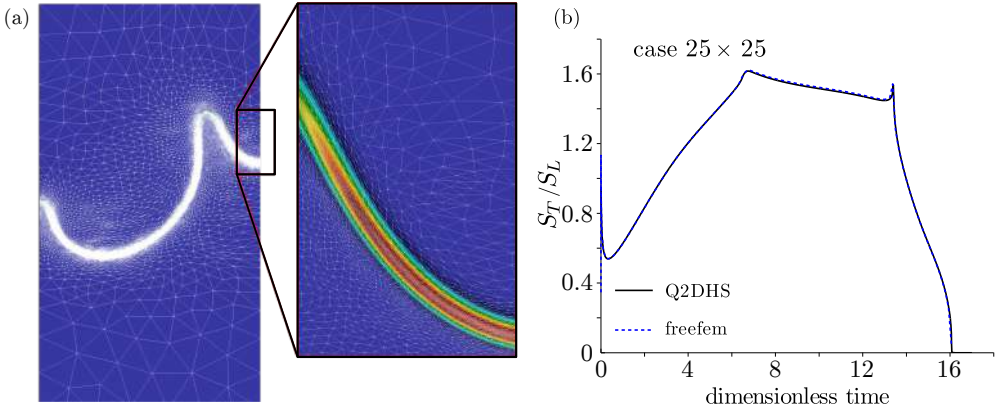


FIGURE 5.9 | (a) Mesh triangulation for a propagating flame from an open end (top) towards a close end (bottom) at an intermediate time step and zoom-in detail of the region marked with a rectangle. The color map depicts the refinement intensity based on the reaction rate. (b) Comparison of the propagation rate between the in-house finite difference code (Q2DHS) used in [22] and the FEM method used herein (b).

rate and pressure are found. Figure 5.9 (a) shows a distribution of the triangular elements at an intermediate instant of the premixed-flame simulation, with an inset that represents in detail the isocontours of reaction rate and the associated locally-adapted mesh. In a typical calculation of a domain $L' = 100\delta_T$, $W' = 30\delta_T$, around $O(10^5)$ triangular elements and grid points are used, with a minimum element size $h = 0.01$ around the reaction region. Spurious mesh-induced flame oscillations in the edges of the flame were observed when the grid is sufficiently coarse far from the reaction region. In this case, the pressure field is not properly solved and numerically-induced oscillations are transferred to both the velocity and the mass fraction field. To avoid them, we introduced an additional pressure-based mesh refinement criteria that ensures the correct calculations of the velocity field that limits the maximum size h_{max} of the grid elements near the open exit of the Hele-Shaw chamber.

Numerical test

Bearing in mind the necessity of proving the independence of the numerical method, we have compared the solution obtained using the finite-element code described above with an in-house, time-dependent, second-order finite-difference code (Q2DHS) [22]. This code runs at every time step the aggregation-based algebraic multigrid method [43] to solve the Poisson equation

(5.29). The test case considered here is a squared Hele-Shaw chamber with $L = W = 25$ and an ignition kernel at $(x_0, y_0) = (0, 12.5)$ given by

$$\theta = \theta_i \exp\left(-\left[(x - x_0)^2 + (y - y_0)^2\right]^{1/2} / r_0\right) \quad (5.32)$$

with the ignition end open to the atmosphere and the flame propagating towards the closed end. To compare both codes, we plot in Fig. 5.9 (b) the propagation rate as defined in (5.3). The results are indistinguishable, with a maximum deviation error less than 0.6%. Unlike the Q2DHS code, the finite-element code used in our computations introduces the additional complexity of dynamically clustering elements near the reaction front. This complication is offset with an optimization of the computational resources that speeds up the calculations and increases the accuracy of the simulations near the corrugated flame, aspect that turns out to be of utmost importance in the description of the traveling flame cells reported above.

CHAPTER 6

Experimental observations of ultra-lean H₂-air flames in narrow channels

Our numerical calculations (chapter 5; [1]) predicted the existence of unexplored lean hydrogen-air flame propagation regimes for quasi-2D geometries, $h \rightarrow 0$, when sufficiently-high heat losses are present in the formulation. Encouraged by these results, we decided to look for them empirically –being that the objective of this chapter–, burning highly-diffusive flames at ultra lean conditions and sufficiently thin gaps, down to $h = 1$ mm, with the aim of promoting the heat losses to the walls of the vessel.

The chapter is structured in the following way. First, we list the few changes done to the experimental setup and procedure used for hydrogen flames, which are required to operate at the mentioned conditions. Moreover, the new propagation regimes are introduced and explained in the next section, where interesting features are discussed in detail. Furthermore, mass diffusivity and the acceleration of gravity were also found to play an important role here, being their effect analyzed in section 6.3 and 6.4 respectively. Finally, some important remarks regarding the local structure of the tiny flames are discussed, focusing on the single or double structure that appears depending on different conditions.

6.1 Experimental setup and procedure

To burn such lean flames, there is no need to make major modifications to the aforementioned Hele-Shaw cell designed for the combustion of hydrogen (chapter 3, Fig. 3.1, [2]). The only

difference is that we are now able to build channels thinner than 4 mm, down to 1 mm. Additionally, we did not have to modify the previous experimental procedure, but a different post-processing of the data is required (Fig. 6.1). The visualization of the flames using Schlieren techniques becomes somehow problematic, due to the considerably small density jump between the burned and unburned gas across the reactive front. We applied an alternative way to determine how these flames propagate, following the path outlined by the condensed water streaks formed just behind them [3], which present a much higher density gradient than the flame itself and make it easier to track the flames (Figs. 6.2 and 6.3).

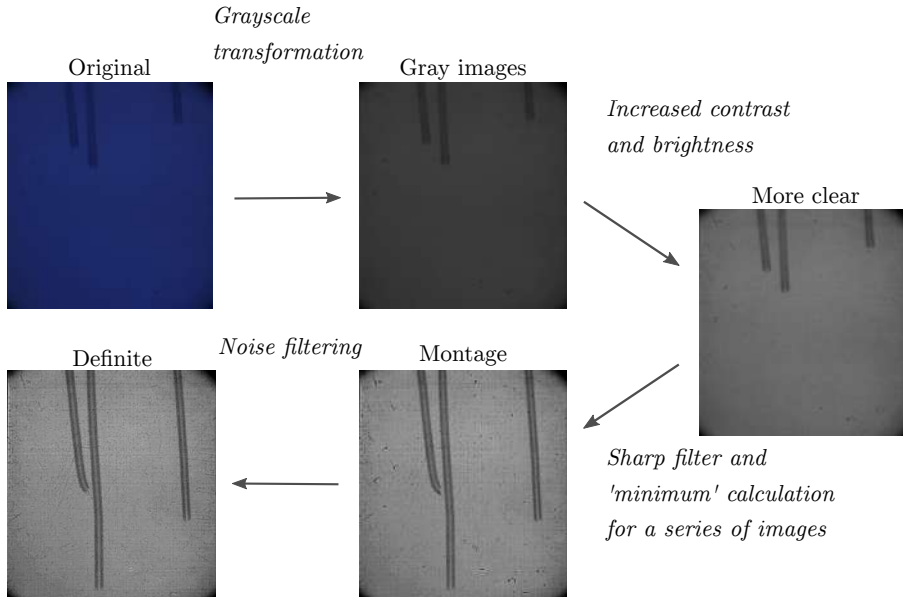


FIGURE 6.1 | Workflow followed for post-processing a series of images obtained from the videos of the experiments.

Table 6.1 summarizes important parameters for the studied lean hydrogen-air premixed flames. Note that the actual percentage-in-volume step used in the experiments is 0.25%, but the table only considers a 1% step to make it more concise. Also, the lean limit reached depends on the direction of propagation because buoyancy promotes burning of upward-propagating flames, being those shadowed mixtures only ignited for these conditions.

TABLE 6.1 | Properties of interest for the tested hydrogen-air mixtures calculated at ambient temperature and pressure. The shadowed mixtures were only ignited when propagating upwards.

%vol. H ₂	ϕ	T _b [K]	S _L [cm/s]	Le	δ_T [mm]
4	0.10	620	1.0	0.31	2.40
5	0.13	660	1.4	0.31	1.71
6	0.15	784	2.9	0.32	0.83
7	0.18	861	4.3	0.33	0.56
8	0.21	938	6.1	0.34	0.39
9	0.24	1013	8.6	0.34	0.28
10	0.26	1093	11	0.34	0.22
11	0.29	1169	15	0.34	0.16
12	0.32	1244	19	0.35	0.13
13	0.36	1319	23	0.35	0.10
14	0.39	1393	28	0.36	0.09
15	0.42	1466	35	0.36	0.07

6.2 Splitting and steady flame cells

Considering the characteristic velocity of the mixture in our experiments to be of the order of the laminar flame speed at lean conditions $S_L \approx 0.1$ m/s and using the kinematic viscosity of air at ambient conditions, we find a maximum Reynolds number $Re \approx 33$ in the range of gaps of interest $1 < h < 6$ mm, a value sufficiently small to anticipate a premixed hydrogen flame that remains in the laminar regime and, contrary to our numerical results, propagates as a continuous wrinkled front [4]. The high mass diffusivity of hydrogen outlines a reactive front characterized by the formation of small wrinkles related to the development of thermodiffusive instabilities (Fig. 6.2 (a) and 6.3 (a)).

In gaps narrower than $h < 6$ mm, the expected continuous flame front breaks into a set of small flame cells separated by cold, unburned gas, unveiling two unprecedented propagation modes that only emerge in flames with low enough hydrogen concentration. In the first one, the flame front breaks into several unstable flame cells (Fig. 6.2 (b) and 6.3 (b)) that split continuously and propagate leaving a path that conforms a fractal-like pattern which reminds of ferns and tree leaves. This propagation mode evokes the way starving fungi or bacteria colonies [5, 6] spread, with lack of nutrients being analogous to fuel scarcity. Also, diffusion-limited aggregation phenomena reveal similar fractal patterns [7]. In the second regime, the flame front breaks into a few isolated stable flame cells (Fig. 6.2 (c) and 6.3 (c)) that move steadily

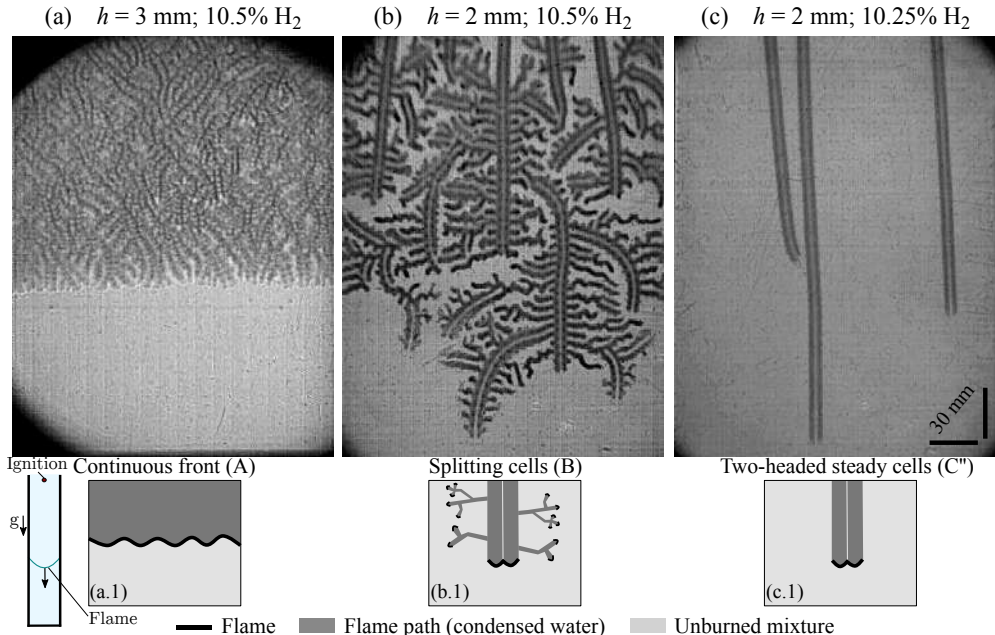


FIGURE 6.2 | Downward-propagating hydrogen flames and their different propagation modes. Image and scheme of (a)-(a.1) continuous flame front propagation, (b)-(b.1) splitting cells that propagate forming fractal patterns and (c)-(c.1) several two-headed isolated steady flame cells.

delineating an almost straight trajectory that brings to our minds the fingering patterns found during smoldering combustion of thin solid materials [8].

From the experimental results it is unclear both how the flame cells are formed and why hydrogen flames withstand more adverse conditions than heavier hydrocarbon fuels (chapter 2; [9]). Thanks to our previous numerical predictions, we could identify the intense heat losses at the walls and the high mass diffusivity of the fuel as, potentially, the two main mechanisms that control the emergence of the newly-discovered propagation modes.

To check our numerical hypothesis, the relative importance of heat losses is measured experimentally using the Peclet number $Pe = h/\delta_T$ [10], a non-dimensional parameter that compares the characteristic diffusive and residence times. Lower values of Pe indicate more relevant heat conduction and, therefore, the effect of heat losses can be stimulated by increasing the wall surface area-to-volume ratio reducing the gap size h (chapter 2; [9] and [11]) or thickening the flame by reducing the concentration of hydrogen in the mixture as indicated in

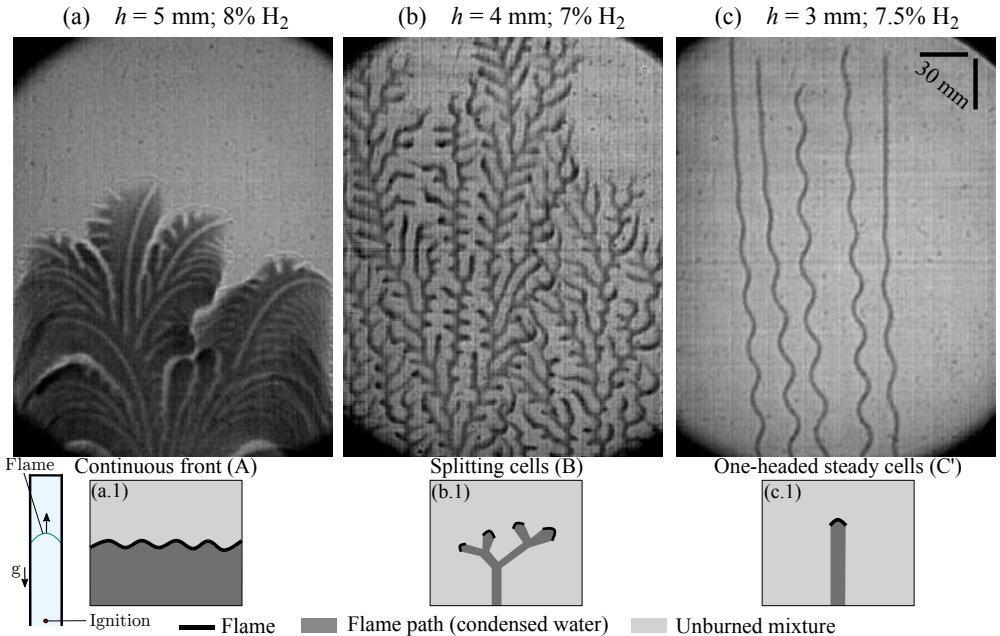


FIGURE 6.3 | Upward-propagating hydrogen flames and their different propagation modes. Image and scheme of (a)-(a.1) continuous flame front propagation, (b)-(b.1) fractal-like propagation mode and (c)-(c.1) several one-headed isolated steady flame cells.

Table 6.1. For sufficiently narrow chambers ($h < 6 \text{ mm}$) and lean mixtures ($\% \text{H}_2 < 16 - h$ dependent), conductive heat losses become decisive [9] and the flame front breaks into pieces. It is under these conditions when the two unprecedented propagation regimes appear. Starting with a constant gap size h , we increase the relative importance of heat losses by reducing the concentration of hydrogen. In mixtures leaner than a critical value, the flame evolves from a continuous front to a group of isolated flame cells that propagate as a fractal. Such transition arises soon after ignition and the few cells so formed do propagate until they reach the end of the chamber. During this time, the flame cells split and bifurcate cyclically, with newborn flame cells branching off, almost perpendicularly, from the main path to quench or to later repeat the splitting cycle (Fig. 6.2 (b) and 6.3 (b)). The paths followed by the flame cells are similar to the flame width $r_f = 5 \text{ mm}$ and form a unique fractal pattern of fractal dimension $d_f \approx 1.7$ (Fig. 6.6), that suggests a non-chaotic behaviour of the propagation, similar to the fractal dimension $d_f \approx 1.65$ observed in the propagation of starving bacteria and electrochemical depositions [6, 12].

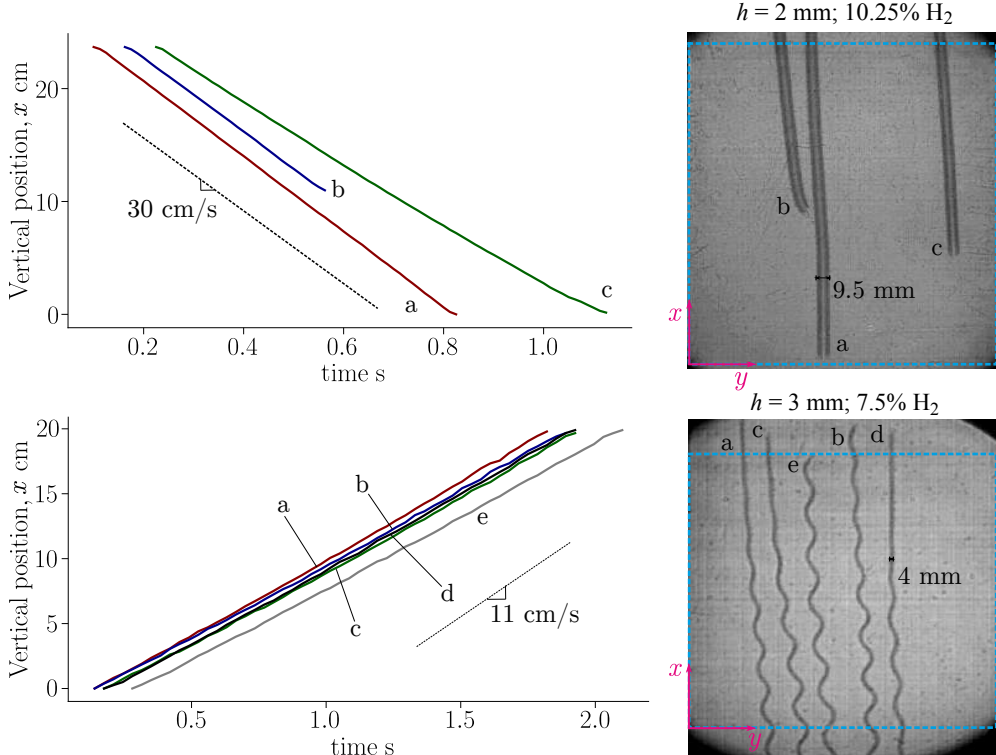


FIGURE 6.4 | Steady cells position with time calculated by tracking the traveling cell flames in the shown regions of interest (red-dashed squares). Moreover, the dashed black lines represent the average steady velocity of the cell flames. Also, the average width of the left tracks is given in the rightmost figures. The errors for the calculated values are ± 0.029 mm for the position and width and ± 15 ms for the time.

Further reduction in hydrogen concentration triggers a second transition that stops the flame cell splitting mechanism. After ignition, now only a few stable isolated cells travel steadily at an almost constant velocity of around $U_L = 30$ cm/s –case dependent–, keeping their size also constant until they reach the end wall of the chamber or extinguish as they collide with the water trail left by other flame cell, where no more fuel is available (Fig. 6.2 (c) and 6.3 (c)). Fig. 6.4 verifies that this isolated flame cells propagate at a constant velocity and width, which depend on several parameters, such as the acceleration of gravity, the mixture composition of the fresh gases, the gap size h , the burnt area (*i.e.*, width of the flames), etc. Conductive heat losses to the walls of the chamber offset heat production to keep the size of the flame cell constant. The unbalance between heat production and heat losses would explain the

splitting mechanism observed before in richer flames. An analogous behavior is observed in unconfined environments, when radiative heat losses were found to be key for the stabilization of three-dimensional hydrogen flames balls at microgravity [13–15].

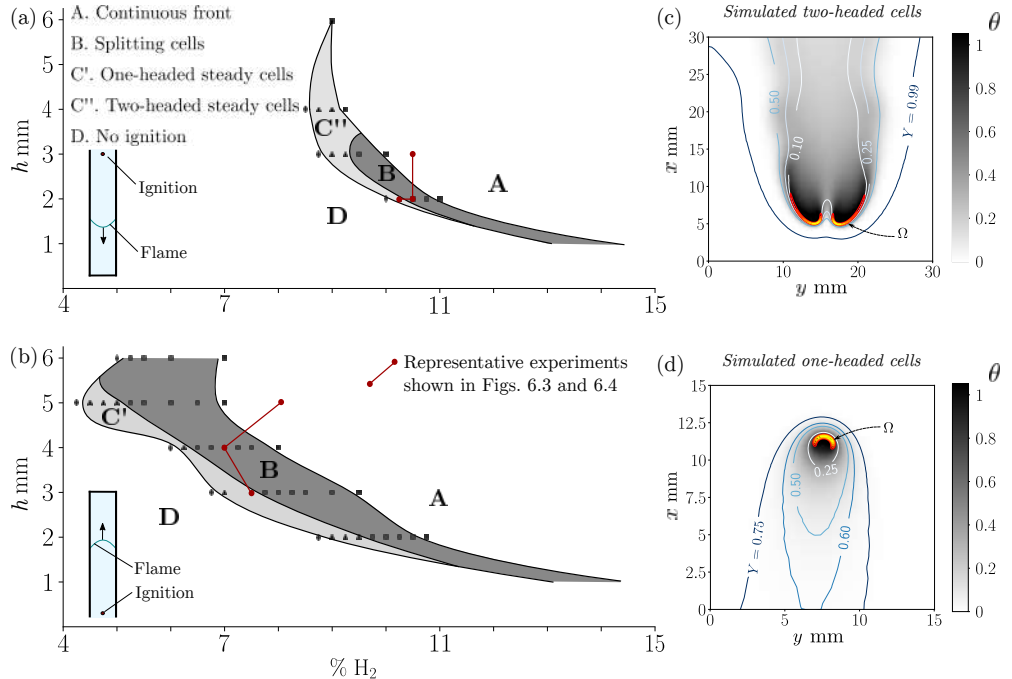


FIGURE 6.5 | Flame propagation modes in the $h\text{-}\% \text{H}_2$ parametric space for both (a) downward- and (b) upward-propagating flames. The solid lines separate the different propagation modes and the symbols represent the cases actually measured. Every experiment is repeated at least 3 times to reduce the uncertainty of the measurements. The mixture composition was obtained with an approximate error of $\pm 0.04 \% \text{H}_2$ and the gap thickness h has an average error of $\pm 0.114 \text{ mm}$. (c) and (d) detail the single and double-headed flame cells Ω obtained from our non-buoyant numerical computations in the limit of very narrow channels.

The relative importance of heat losses was also modified keeping a constant hydrogen concentration and changing the gap size. Qualitatively, the results are similar regarding the emergence of the two above-described regimes and are used to delineate a stability map in the $h\text{-}\% \text{H}_2$ parametric space (Fig. 6.5).

The criteria used to define the different regions traced in Fig. 6.5 is based on the fractal dimension of the condensed water path formed during the flame propagation, that evolves from $d_f \approx 2$ (continuous front Fig. 6.2 (a) and 6.3 (a)), $d_f \approx 1.7$ (splitting cells Fig. 6.2 (b) and

6.3 (b)) to $d_f \approx 1$ (steady traveling cells Fig. 6.2 (c) and 6.3 (c)). Also, the fractal dimension provides information about the degree of utilization of the available fuel, with $d_f = 2$ indicating total fuel consumption, $d_f \approx 1.7$ meaning that the flame bifurcates and burns around 40% of the total mixture and $d_f = 1$ showing that most of the fresh mixture remains unburned. To calculate the fractal dimension of the path followed by the flames in our experiments, we first transformed the gray images into binary. Then, their *skeletons* (Fig. 6.6) were extracted and analyzed applying the standard box counting method. We include in Fig. 6.6 the logarithmic variation of the number of boxes needed to fill the whites n as a function of the logarithm of the box size ϵ in linear scale. The fractal dimension d_f is then given by the slope of the linear fit of the experimental points (variance $\sigma^2 > 0.995$).

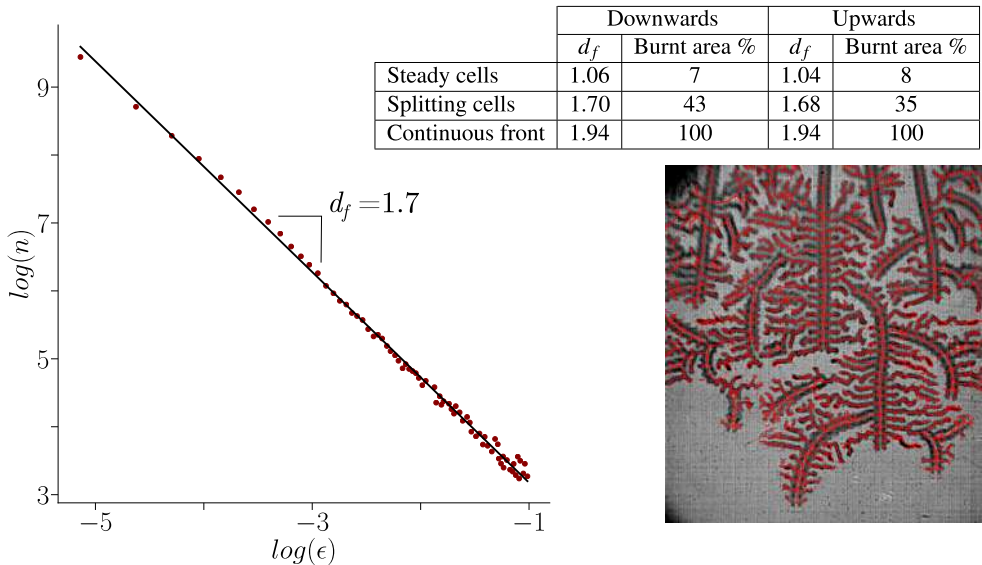


FIGURE 6.6 | Fractal dimension and burnt area analysis using the box-counting method for the different propagation methods found in the study. The bottom-right image represents the *skeleton* used for the calculations.

Moreover, we designed Fig. 6.7 from the numerical results obtained in the previous chapter to facilitate the comparison with our experimental observations. We show in dark colours the paths followed by the tiny flames, which are represented by reddish contours. Here, the effect of increasing heat losses (from left to right) verify the existence of the three reported propagation mechanisms: from a continuous front, to the *splitting cells* that form fractal patterns

to finally reach the isolated *steady cells*. Conductive heat losses to the enclosing walls trigger the transition between them.

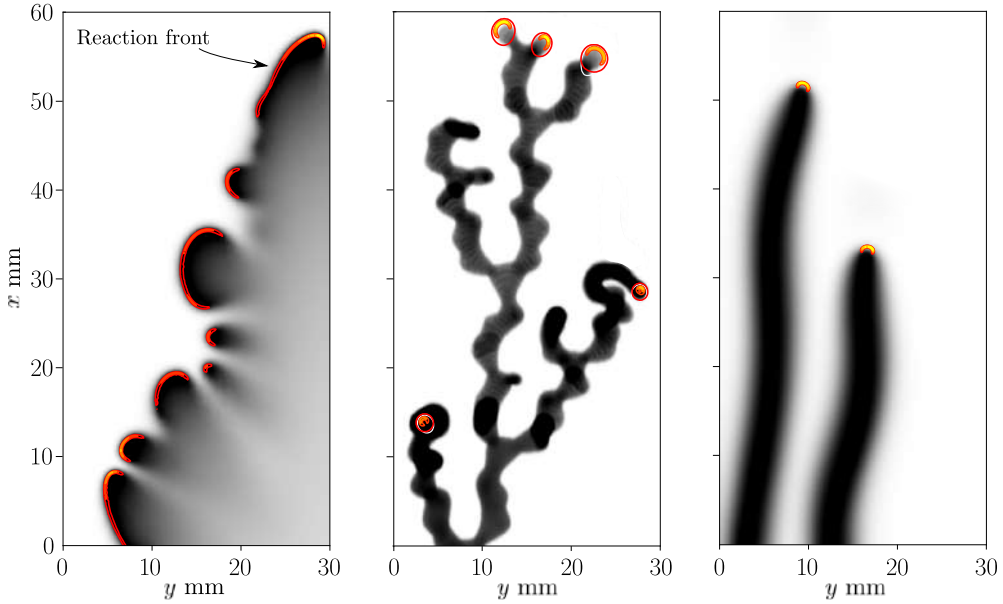


FIGURE 6.7 | Numerical results obtained for increasing heat losses to the plates (left to right). The dark regions show the path followed by the flame front, which is depicted with reddish contours at the latest time step of the simulation.

6.3 Effect of mass diffusivity

The effect of mass diffusivity was explored by testing experimentally (chapter 2; [9]) and numerically (chapter 5; [1]) methane and dymethilether (DME) flames, fuels with much lower mass diffusivity, with $Le \approx 1, 1.75$ for methane and DME flames respectively. For methane and DME ($Le \geq 1$), the flame does not withstand the heat losses that increase as the gap size h is reduced and extinguishes forming a continuous reactive front as shown for a DME flame propagating in a $h = 1$ mm channel (Fig. 2.14; [9]). This result then identifies mass diffusivity as the mechanism that counteracts heat losses and the high diffusivity of hydrogen becomes then flawlessly the survival mechanism that gives birth to the flame cells within which the temperature is high enough, always above the crossover temperature around 1000 K, to sustain combustion. The instantaneous high concentration gradient across the front triggers

the fast diffusion of hydrogen from the unburned region towards the surroundings of the flame, increasing the local availability of H₂. The additional energy released by the burning of this extra fuel is used to counteract conductive heat losses, extending hydrogen combustion towards ultra-lean mixtures below %H₂ < 5.

6.4 Effect of gravity

Considering safety-related real-life scenarios, gravity also plays an important role in stabilizing or destabilizing flames in vertical channels [16], as shown in chapters 2 and 3. To analyze to a greater extent how gravity intervenes in the development of the described propagation modes, we tested experimentally both upward- and downward-propagating flames to expand our stability map (Fig. 6.5). Similarly to methane and DME flames, in the downwards propagating case, extinction takes place with the H₂ flames forming a continuous reactive front for fuel concentrations below %H₂ < 9 in channels wider than 6 mm, approximately. Surprisingly, leaner mixtures can be found in narrower gaps once the reactive front of the H₂ flame is broken into small separated cells that show, mainly, a double-headed structure similar to that obtained numerically in our computations (Fig. 6.5 (c)). Simultaneously, the reduction in the gap size increases the relative importance of the gas viscosity, reducing the buoyant velocity induced by gravity and facilitating the propagation of the flame. The minimum fuel concentration %H₂ = 8.5 was found for $h = 4$ mm (Fig. 6.5 (a)).

In upward-propagating flames, buoyancy accelerates the flames and dilates the flammability limits to mixtures significantly leaner than in downward-propagating flames (Fig. 6.5). As in downward-propagating flames, extinction takes place for richer mixtures in channels wider than $h > 5$ mm. The minimum fuel concentration was found for $h = 5$ mm when a fuel concentration as lean as %H₂ ≈ 4.5 was capable of sustaining a solitary one-headed flame cell steadily traveling along the combustion chamber. In narrower channels, conductive heat losses shift the extinction limit towards richer H₂ mixtures (Fig. 6.5). The influence of gravity diminishes in very narrow channels, with both upward and downward propagating flames presenting an almost coincident extinction limit when $h = 1$ mm (Fig. 6.5 (b)).

6.5 One or two-headed cells

From the experiments, one can conclude that one- and two-headed flames are more prone to appear when propagating up- and downwards respectively. Following the same idea as in chapter 5, circle like one-headed flames would appear when the residence time of the propagating flame cells ($t_r = r_f/U_L$) and the diffusion time ($t_{diff} = D_T/(Le \cdot r_f)$ with $D_T = 2.5 \times 10^4$ and $Le = 0.3$) required for hydrogen to feed them were of the same order. When the flames travel too fast, the required time for hydrogen to feed them is too long and therefore the cells would not be able to close and the open double-headed structure arises. When the flames propagate upwards, this can be easily checked considering that buoyancy controls the overall motion, thus $U_L = \sqrt{(1 - T_u/T_b)gr_f}$. Next, comparing t_{diff}/t_r the required flame size r_f is given by $r_f = [D_T/(Le\sqrt{(1 - T_u/T_b)g})]^{2/3} \sim 4.7$ mm and thus $U_L \sim 17$ cm/s, which match with the experimentally observed values for circular flames (Fig. 6.4). Regarding the downward-propagating cases, it is not so straightforward to obtain the propagation velocity. However, if we make use of our experimental observations, the said controlling relation t_{diff}/t_r equals 3.6 and reinforces our previous idea.

However, we found both structures for gravity-free conditions in our simplified numerical model (chapter 5; [1]), which keeps the question about how gravity controls the shape of these traveling flames open. These differences may be based on the simplifications applied to the simulations, such as using a one-step Arrhenius model to represent a more complicated chemical chain reaction and neglecting both the viscosity and diffusivity jump across the reactive front. Although, the qualitative similarities between the calculation and the experimental findings are undeniable.

References

- [1] D. Martínez-Ruiz, F. Veiga-López, D. Fernández-Galisteo, V. N. Kurdyumov, M. Sánchez-Sanz, The role of conductive heat losses on the formation of isolated flame cells in hele-shaw chambers, *Combustion and Flame* 209 (187–199) (2019).
- [2] F. Veiga-López, M. Kuznetsov, D. Martínez-Ruiz, M. Sánchez-Sanz, Thermoacoustic analysis of lean premixed hydrogen flames in narrow vertical channels, Preprint submitted to *Fuel* (2020).
- [3] B. Bregeon, A. S. Gordon, F. A. Williams, Near-limit downward propagation of hydrogen and methane flames in oxygen nitrogen mixtures, *Combustion and Flame* 33 (33–45) (1978).
- [4] J. Yanez, M. Kuznetsov, J. Grune, Flame instability of lean hydrogen-air mixtures in a smooth open-ended vertical channel, *Combustion and Flame* 162 (2830–2839) (2015).
- [5] R. Halvorsrud, G. Wagner, Growth patterns of the slime mold *physarum* on a nonuniform substrate, *Physical Review E* 57 (941) (1998).
- [6] E. Ben-Jacob, O. Schochet, A. Tenenbaum, I. Cohen, A. Czirok, T. Vicsek, Generic modelling of cooperative growth patterns in bacterial colonies, *Nature* 368 (46) (1994).
- [7] T. Witten Jr, L. M. Sander, Diffusion-limited aggregation, a kinetic critical phenomenon, *Physical review letters* 47 (1400) (1981).
- [8] O. Zik, Z. Olami, E. Moses, Fingering instability in combustion, *Physical review letters* 81 (3868) (1998).
- [9] F. Veiga-López, D. Martínez-Ruiz, E. Fernández-Tarrazo, M. Sánchez-Sanz, Experimental analysis of oscillatory premixed flames in a hele-shaw cell propagating towards a closed end, *Combustion and Flame* 201 (1–11) (2019).
- [10] M. Kuznetsov, J. Grune, Experiments on combustion regimes for hydrogen/air mixtures in a thin layer geometry, *International Journal of Hydrogen Energy* 44 (8727–8742) (2019).
- [11] M. Sánchez-Sanz, Premixed flame extinction in narrow channels with and without heat recirculation, *Combustion and Flame* 159 (3158 - 3167) (2012).

- [12] V. Fleury, J. Kaufman, D. Hibbert, Mechanism of a morphology transition in ramified electrochemical growth, *Nature* 367 (435) (1994).
- [13] Y. B. Zeldovich, Theory of combustion and gas detonation (1944).
- [14] P. Ronney, K. Whaling, A. Abbud-Madrid, J. Gatto, V. Pisowicz, Stationary premixed flames in spherical and cylindrical geometries, *AIAA journal* 32 (569–577) (1994).
- [15] P. D. Ronney, M.-S. Wu, H. G. Pearlman, K. J. Weiland, Experimental study of flame balls in space: Preliminary results from sts-83, *AIAA journal* 36 (1361–1368) (1998).
- [16] P. Clavin, G. Searby, Combustion waves and fronts in flows: flames, shocks, detonations, ablation fronts and explosion of stars (2016).

Conclusions and future work

Conclusions

The propagation of low-Lewis premixed flames in non-adiabatic Hele-Shaw combustion chambers was analyzed both numerically and experimentally in this thesis.

First, taking advantage of the limit $a = h/\delta_T \ll 1$, we simplified the problem down to a quasi-2D case in which the velocity field is controlled by viscous effects. The resulting system of equations is solved numerically.

We recalled the widely-known result that steady flame circles cannot exist in a quiescent atmosphere using the reactive-diffusive system written in eq. (5.1) because of the lack of mathematical solution for the mass fraction profiles. In the adiabatic case, our results recovered the dynamics of unstable cell growth and the development of diffusive-thermal instabilities found previously in [1]. However, when conductive heat losses are included, our transient numerical calculations show the existence of isolated circle or comet-like flame cells travelling along the combustion chamber in the limit of slow propagation velocity. The two-dimensional equivalent to a flame ball arises stabilized by means of conductive heat losses, in comparison to pure convective effects considered by Grcar [2].

The dynamics of the isolated flame cells is very different depending on the orientation of the combustion chamber. In horizontal vessels, stable one or two-headed comet-like flames are formed in both open-closed (OC) and closed-open (CO) configurations for moderately large heat losses to the enclosing walls. Both the size of the flame cell and its travelling

velocity remain constant. Larger values of the heat loss parameter make the flame to adopt a semicircular shape to maintain the temperature high enough to sustain the reaction before total quenching happens. When propagating in favor of gravity, the dynamics of the isolated flame cells changes. In the OC configuration, the flame adopts a semicircular shape that undergoes a random walk with several flame-splitting episodes that form alternative paths branching off from a main flame cell pathway that is determined by the buoyancy forces. On the contrary, in the CO configuration, the semicircular flame cells are stable and propagate along the chamber with constant shape and velocity. Larger values of the heat losses parameter are necessary to extinguish the flame compared to the non-buoyant case. However, for propagation against the influence of gravity, only comet-like stable flames were observed in our calculations. Values of the extinction heat losses parameter are much smaller than upwards propagating flames, and not large enough to enable the generation of the circular regime.

Second, a series of experiments were carried out to validate our calculations for highly-diffusive fuels. Ultra-lean hydrogen-air premixed flames were burned, both propagating up- and downwards, in very narrow ($h \leq 6$ mm) OC combustion chambers.

The three different propagation mechanisms predicted by the numerical calculations were found. The increasing influence of heat losses was checked by reducing either the combustion chamber thickness or the concentration of hydrogen, keeping the other constant. When the losses were not intense enough, the expected continuous front was found. Once the transfer of heat to the walls exceeds a critical value, the front destabilizes triggering a new, fractal-like propagation mode. Further increment of the relative heat losses makes the flame cells to move steady without splitting.

Furthermore, differential diffusion plays a fundamental role in the formation of both circle or comet-like flames. For mixtures with values of $Le \gtrsim 1$, small flame curvatures develop with important influence of heat losses on the flame temperature. Even for small values of heat losses, they offset heat production inducing a rapid temperature decrease that extinguishes the nearly planar flame. Additionally, this effect was also reported experimentally by burning methane and DME non-buoyant flames in very narrow channels. As stated, the flames were found to extinguish as a continuous front once the heat losses to the walls are high enough. It is only the combined effects of heat losses and differential diffusion what make possible the appearance and development of these singular flame structures.

The discovery of the propagation regimes described before opens new research lines and leaves unanswered questions –some examples are addressed in the following section– regarding near-limit hydrogen combustion in narrow geometries. As the use of hydrogen in the near future is expected to increase [3, 4], we anticipate a raising concern about the safety of hydrogen-powered devices [5] that will motivate the exploration of interactions between different phenomena that may unveil unknown flame behaviours relevant in the development of safety measures.

Future work

The main physical mechanisms responsible for the appearance of our findings happen to be clear after both the numerical and experimental study. Nevertheless, there is still a long way to control and fully understand the phenomena. For that, we propose here some ideas to keep working on the topic.

Theoretical and numerical studies

- Look for a mathematical explanation that would solve the problem introduced in eq. (5.1).
- Fully understand the appearance of the one- or double-headed flame structures found preferably for upward- and downward-propagating fronts in the experiments.
- Reduce the number of hypothesis used to simplify the problem. The first step would be to let viscosity to change with temperature, that is modifying the exponent σ not to be zero.

Experiments

- Improve the experimental setup to better capture the structure of the small low-temperature flame cells, as they are difficult to see using the *Schlieren* system. We propose again the use of OH filters on the camera. Furthermore, being able to measure the temperature distribution within the chambers would add extra and interesting information.

- Check the predictions modifying the boundary conditions, making the flames burn from a closed to an open end (CO).
- Burn non-buoyant hydrogen flames in a similar geometry to the one proposed here to characterize the effect of gravity completely.
- Keep reducing, if possible, the gap distance for $h < 1$ mm to complete the instability map.

References

- [1] D. Fernández-Galisteo, V. N. Kurdyumov, P. D. Ronney, Analysis of premixed flame propagation between two closely-spaced parallel plates, *Combustion and Flame* 190 (133–145) (2018).
- [2] J. F. Grcar, A new type of steady and stable, laminar, premixed flame in ultra-lean, hydrogen–air combustion, *Proceedings of the Combustion Institute* 32 (1011–1018) (2009).
- [3] I. Staffell, D. Scamman, A. V. Abad, P. Balcombe, P. E. Dodds, P. Ekins, N. Shah, K. R. Ward, The role of hydrogen and fuel cells in the global energy system, *Energy & Environmental Science* 12 (463–491) (2019).
- [4] A. L. Sánchez, F. A. Williams, Recent advances in understanding of flammability characteristics of hydrogen, *Progress in Energy and Combustion Science* 41 (1–55) (2014).
- [5] M. Kuznetsov, J. Grune, Experiments on combustion regimes for hydrogen/air mixtures in a thin layer geometry, *International Journal of Hydrogen Energy* 44 (8727–8742) (2019).

Acknowledgments

This work was supported by projects ENE2015-65852-C2-1-R (MINECO/FEDER, UE) and BYNV-ua37crdy (Fundación Iberdrola España), and internal KIT funding.

